

Automatic and Accurate Segmentation of Thoracic Aortic Aneurysms from X-ray CT Angiography

by

Filipa I M Ferreira

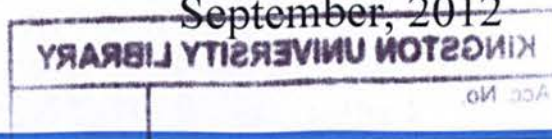
Submitted in partial fulfilment of the requirements of

Kingston University for the degree of

Doctor of Philosophy



September, 2012



Kingston University London

[Page intentionally left blank]

Supervision:

Prof Jamshid Dehmehski (Director of Studies)¹

Prof Salah Qanadli^{1,2}

Dr A Britten³

Dr A Belli³

¹ Quantitative Medical Imaging International Institute (QMI³)
Faculty of Science, Engineering and Computing
Kingston University
Penrhyn Road
Kingston upon Thames
KT1 2EE
United Kingdom

² Centre Hospitalier Universitaire Vaudois(CHUV)
Service de Radiodiagnostic et Radiologie Interventionnelle
Unité Cardio-Thoracique et Vasculaire
CH 1011 Lausanne
Switzerland

³ St George's University of London
Cranmer Terrace
London
SW17 0RE
United Kingdom

[Page intentionally left blank]

Declarations

I hereby declare that this dissertation describes my solely own research, which was carried out at Kingston University, except where otherwise indicated. Other sources are acknowledged by explicit references. Some of the research presented in this thesis has already been published or is under review for publication. For a complete list of publications, please refer to appendix 1.

This thesis has not been previously accepted in substance for any degree and is not being concurrently submitted to any other University for examination either in the United Kingdom or overseas.

Filipa Ferreira

[Page intentionally left blank]

Abstract

The scope of this dissertation is to procure and propose a novel fully automated computer aided detection and measurement (CAD/CAM) system of thoracic aortic aneurysms. More explicitly, the objective of the algorithm is to facilitate the segmentation of the thoracic aorta, as accurately as possible and detection of possible existing aneurysms in the Computer Tomography Angiography (CT) images. In biomedical imaging, the manual examination and analysis of aortic aneurysms is a particularly laborious and time-consuming undertaking. Humans are susceptible to committing errors and their analysis is usually subjective and qualitative due to the inter- and intra-observer variability issue. Objective and quantitative analysis facilitated by the application developed in this project leads to a more accurate diagnostic decision by the physician. In this context, the project is concerned with the automatic analysis of thoracic aneurysms from CTA images. The project initially examines the theoretical background of the anatomy of the aorta and aneurysms. The concepts of image segmentation and, in particular, segmentation of vessels methods are reviewed. An algorithm is then developed and implemented, such that it will conform to the requirements put forth in the stated objectives. For purposes of testing the proposed approach, a significant amount of 3D, clinical CTA datasets of thoracic aorta form the framework of the CAD/CAM system. It is followed by presentation and discussion of the results. The system has been validated on a clinical dataset of 30 CTA scans of which 28 CTA scans contained aneurysms. There were 30 CTA scans used as training dataset for parameter selection and another 30 CTA scans used as a test dataset, in total 60 for clinical evaluation. The radiologist visually inspected the CAD and CAM component results and confirmed it correctly detected and segmented the TAA on all datasets, proving to have 100% sensitivity. We were able to conclude that there is distinct potential for use of our fully automated CAD/CAM system in a real clinical setting. Although other CAD/CAM systems have been developed for other organ detection and even small sections of the thoracic aorta, to this date no fully automated CAD/CAM of the entire thoracic aorta has been developed hence its novelty. To facilitate the proposed CAD/CAM system is integrated in a Medical Images Processing, Seamless and Secure Sharing Platform (MIPS3) which is a friendly user interface that has been developed alongside with this project.

[Page intentionally left blank]

Acknowledgement

I would like to express my deep appreciation and gratitude to my supervisor, Prof Jamshid Dehmeshki for his patience, suggestion and encouragement during my academic and research work at Kingston University. I consider myself extremely fortunate to have worked under his supervision. Throughout this PhD, it was his vision, motivation and invaluable input that have brought me to this phase.

Also I would like to thank my co-supervisor Prof. Salah Qanadli for all his comments regarding the medical aspects of the research and clinical support.

I thank the South West London Academic Network (SWan) for the financial support of this work throughout the past three years.

It is needless to say that my gratitude goes towards all my family and friends who supported me in this adventure and were (and still are) an inexhaustible source of inspiration. Especially, a big thank you to my parents for their love, encouragement and support to ultimately pursue my future goals. Without their encouragement and love this thesis could not have materialized.

Lastly, a special thanks to Dr Maria Martini and Dr Xujiong Ye who kindly reviewed and assessed this thesis.

[Page intentionally left blank]

To my family

[Page intentionally left blank]

List of Publications

- **F. Ferreira, S. Qanadli, M. Dehkordi, A. Britten, A. Belli, A-M Jouannic, J. Dehmeshki .** New computer aided detection and measurement system for thoracic aortic aneurysms from CT angiography. SSR-SGR congress 2011.
- **F. Ferreira, J. Dehmeshki, H. Amin, M.E. Dehkordi, A. Belli and S. Qanadli.** An adaptive 3D region growing algorithm to automatically segment and identify thoracic aorta and its centreline using Computed Tomography Angiography Scans. SPIE International Symposium on Medical Imaging 2010.
- **F. Ferreira, J. Dehmeshki, H. Amin, M.E. Dehkordi, A. Belli and S. Qanadli.** An adaptive 3D region growing algorithm to automatically segment and identify the thoracic aorta using CT Angiography. 10th Annual Meeting of the Union of Vascular Societies of Switzerland 2009.

[Page intentionally left blank]

Contents

Declaration	V
Abstract	VII
Acknowledgements	IX
Publications	XIII
Contents	XV
List of Figures	XIX
List of Tables	XXVI
Glossary of Words	XXVIII
1. Introduction	1
1.1. Motivation.....	2
1.2. Anatomy of the Aorta	2
1.2.1. Thoracic Aortic Aneurisms (TAA)	4
1.3. Medical Imaging Technologies.....	6
1.3.1. PACS.....	6
1.3.2. DICOM.....	7
1.3.3. Computer Tomography.....	8
1.3.3.1. First Generation CT Imaging.....	10
1.3.3.2. Second Generation CT Imaging.....	11
1.3.3.3. Third Generation CT Imaging.....	13
1.3.3.4. Fourth Generation CT Imaging.....	14
1.3.3.5. Image reconstruction.....	15
1.3.3.6. Computed Tomography Angiography	18
1.3.3.7. CT vs MRI.....	19
1.4. Techniques of Aortic Aneurysm diagnosis and repair.....	20
1.5. Research Objectives.....	23
1.6. Thesis Organization.....	24
2. Computer Aided Detection(CAD)	25
2.1. CAD Literature Review.....	26
2.1.1. Mammography CAD.....	27
2.1.2. Brain CAD.....	29

2.1.3. Lung CAD.....	32
2.1.4. Colon CAD.....	34
2.2. TA CAD Literature Review.....	35
2.2.1. TA CAD in MRI.....	35
2.2.2. TA CAD in CT.....	37
2.3. CAD Image process components Literature Review.....	41
2.3.1. Pre-processing.....	42
2.3.1.1. Diffusion Filtering.....	43
2.3.1.1.1. Linear diffusion.....	44
2.3.1.1.2. Isotropic non-linear diffusion.....	45
2.3.1.1.3. Anisotropic diffusion.....	46
2.3.2. Image Segmentation	47
2.3.2.1. Thresholding.....	48
2.3.2.1.1. Automatic Thresholding.....	50
2.3.2.2. Region-Growing.....	52
2.3.2.3. Level set.....	57
2.3.2.4. Finding ellipses.....	62
2.3.2.4.1. Ellipse fitting methods.....	64
2.3.3. Finding Centreline Paths.....	65
2.3.3.1. Hessian Matrix.....	66
2.3.3.2. Flux Driven.....	67
2.3.3.3. Distance Transform.....	72
2.4. Summary	73
3. Proposed CAD System	74
3.1. Pre-Processing.....	76
3.2. TA Lumen Segmentation.....	77
3.2.1. Automatic Seed Selection.....	77
3.2.1.1. Celiac Trunk.....	81
3.2.2. Region Growing algorithm.....	86
3.3. Identify lumen centreline using Distance Transform.....	86
3.3.1. Voxel Coding.....	88
3.3.2. Cluster network construction.....	90
3.3.3. Skeleton construction.....	90
3.3.4. Smoothing and Pruning.....	92
3.4. Generating plane orthogonal to lumen centreline.....	96

3.5. Automatic detection of aneurysm (CAD).....	97
3.6. Summary.....	98
4. Proposed CAM System	100
4.1. Detection and segmentation of the Thoracic Aorta (aortic aneurysms).....	101
4.1.1. Ellipse fitting method.....	102
4.2. Characterizing aneurysm.....	110
4.3. Summary.....	111
5. Experimental Results and Validation(CAD & CAM)	112
5.1. MIPS3.....	114
5.2. Evaluation of CAD and CAM performance.....	121
5.2.1. Data Acquisition.....	122
5.2.2. CAD Results.....	122
5.2.2.1. TA Lumen Segmentation.....	123
5.2.2.1.1. Automatic Seed Selection.....	123
5.2.2.1.1.1. Validation of Automatic Seed Selection	126
5.2.2.1.2. Region Growing Algorithm.....	127
5.2.2.1.3. Validation of Lumen Segmentation.....	132
5.2.2.2. Identify Lumen Centreline Using DT.....	133
5.2.2.3. Generating Plane Orthogonal to Centreline.....	133
5.2.2.4. Automatic Detection of Aneurysm (CAD).....	134
5.2.2.4.1. Validation of CAD system.....	134
5.2.3. CAM Results.....	135
5.2.3.1. Segmentation of TAA.....	135
5.2.3.1.1. Validation of CAM system.....	136
5.3. Summary.....	141
6. Conclusions	142
6.1. Conclusions	143
6.2. Future Research	145
6.3. Closing Remarks.....	147
References	148

[Page intentionally left blank]

List of Figures

Figure 1.1:	The entire aorta and its major branches aorta.....	3
Figure 1.2:	Example of the average a humans aorta diameter and length through its life.....	4
Figure 1.3:	Ascending Aortic Aneurysm.....	5
Figure 1.4:	Descending Thoracic Aneurysm.....	5
Figure 1.5:	PACS workflow.....	7
Figure 1.6:	Typical slices of a CT volume, that are taken at regular interval across the patient. Vessels appear white because they are filled with a contrast product.....	8
Figure 1.7:	X-Ray CT scan.....	8
Figure 1.8:	First generation CT scanner.....	11
Figure 1.9:	Second generation CT scanner	12
Figure 1.10:	Hounsfield units scale.....	12
Figure 1.11:	Third generation CT scanner.....	13
Figure 1.12:	Fourth generation CT scanner.....	14
Figure 1.13	(a) Object imaged with four projections (P1-P4). (b) Reconstructed image.....	16
Figure 1.14:	A 2x2 matrix gives a simple visual schematic of CT linear back projection.....	16
Figure 1.15:	(a) The original 2 x 2 matrix with numerical values. (b-e) show the backprojected linear attenuation intensities measured for each projection and (f) shows the reconstructed matrix equations. The reconstructed matrix is normalized by subtracting the smallest element value and then dividing by the greatest common factor (6) yielding (g) the original matrix.....	17

Figure 1.16:	Comparison of CT and MRI images. (a) CT scan and (b) MRI showing the increased sensitivity that MRI adds in visualizing brain lesions, such as those in MS(arrows).....	19
Figure 1.17:	CT scan of the chest.....	20
Figure 1.18:	Illustration of the region of interest.....	21
Figure 1.19:	Example of bifurcation aortic stent graft	22
Figure 1.20:	Illustration of a stent graph being positioned in the aorta for repair of aneurysm.....	22
Figure 2.1:	Flow chart of Songyang Yu <i>et al.</i> CAD system. (a) A mammogram from the database. (b) A cluster of microcalcifications in (a). (c) The ground truth image corresponding to the cluster of microcalcifications in (b).....	27
Figure 2.2:	(a) Original breast image after breast region segmentation and (b) CAD detected masses denoted with asterisks. In one case, the centroid of the focal activity layer is outside the physician's mass annotation (shown in red).....	29
Figure 2.3:	Kobashi <i>et al.</i> proposed CAD system.....	30
Figure 2.4:	Aneurysm detection result of a patient in Lauric <i>et al.</i> (a) Original 3D-rotational angiography. (b) Corresponding medial axis of the 3D-RA dataset. (c) Detection results. Positive results were coloured in red. Black arrows point to true positives.....	31
Figure 2.5:	J. Tong <i>et al.</i> proposed CAD system flowchart. A nodule in the right lung lobe (red line) is illustrated in (a) and detected in (b) with authors CAD system.....	33
Figure 2.6:	A cross section of a colon data (a) and its colon segmentation and skeletonization result (b) of J. Dehmeshki <i>et al.</i> proposed CAD system.....	34
Figure 2.7:	(a) Original image and the deformable model after (b) initialization, (c) SA optimization (1.83% error), (d) ICM optimization (21.98%), (e) greedy optimization (28.85%), and (f) gradient descent optimization (48.81%).....	36
Figure 2.8:	(a) The original axial slice, (b) the magnied axial slice with proper contrast	

	and intensity in order to increase the accuracy of the manual segmentation, (c) the manually outlined aorta (dotted line) and (d) the correction of inaccuracies in the outline by repositioning some nodes in the 3D mesh (white line).....	38
Figure 2.9:	Results of the automated segmentation by I. Isgum, <i>et al.</i> (2009).....	40
Figure 2.10:	Example of a Gaussian filter kernel.....	44
Figure 2.11:	Thresholding (a) original image (b) threshold image.....	49
Figure 2.12:	On the left a four-neighbour stencil in 2D. On the right a 26-neighbor stencil in 3D. In both illustrations the reference grid point is shown in red and its neighbours in blue.....	53
Figure 2.13:	(a) Original head MR image. (b) Segmentation result of five regions superimposed on the original image (c), (d) peripheral contrast and average contrast regions and boundaries segmented out from image (a).....	56
Figure 2.14:	Illustration of the transformation of front motion into the level set.....	58
Figure 2.15:	Ellipse geometry.....	63
Figure 2.16:	Blum's Glassfire Flow, moving forward and inward normal vectors.....	68
Figure 2.17:	Flux-based level-set.....	71
Figure 3.1:	Flowchart of the proposed CAD/CAM system.....	75
Figure 3.2:	(a) Schematic overview of the celiac trunk (b) generated 3D image of the celiac trunk.....	78
Figure 3.3:	Lung regions. (a) Coronal view showing aorta below the lung regions (white arrow), (b) axial view of a lung, (c) extracted lung following thresholding and a morphological operation.....	79
Figure 3.4:	Celiac Trunk (a) Sagittal view showing the Celiac Trunk (arrowed), (b) Projected sagittal view of a segmented aorta, (c) result of morphological operation performed on b.....	80
Figure 3.5:	Detection of first seed point for region growing method illustration.....	81
Figure 3.6:	Flow chart of image segmentation of aortic lumen.....	81
Figure 3.7:	First image on the left is the matrix of the input image. Picture on the right	

	represents the matrix of the seed point on the output image matrix of zeros.....	82
Figure 3.8:	Image shows second seed point labelled on the output image. The labelled neighbouring pixels to the region are labelled in yellow and blue.....	82
Figure 3.9:	Image shows third seed point labelled on the output image. The image shows the neighbourhood of the region in zero with coloured background...	83
Figure 3.10:	Graph of average contrast of CTA image 01087.....	83
Figure 3.11:	Labelled boundary of the aortic lumen.....	84
Figure 3.12:	Schematic of input image, labelled region in the image, and output image (segmented image). (CTA slice 1053).....	84
Figure 3.13:	Schematic of input image, labelled region in the image, and output image (segmented image). (CTA slice 1068).....	85
Figure 3.14:	(a) shows a synthetic image (b) BS code of synthetic images (c) SS code of a synthetic 2D image.....	87
Figure 3.15:	SS filed of synthetic image and its Cluster network.....	89
Figure 3.16:	(a) original image, (b) resulted skeleton from original algorithm, (c)resulted skeleton from modified method.....	91
Figure 3.17:	Schematic of vessel segment central axis and orthogonal plane through segment midpoint.	92
Figure 3.18:	Above image is the 3D rendering of the aorta. Lower left: slice with its elliptical cross section of the healthy vessel. Lower right: orthogonal slice through the vessel showing the nearly circular cross section of a healthy vessel.....	93
Figure 3.19:	Cube.....	94
Figure 3.20	(a) Orthogonal plane detected (b) stack of images converted.....	96
Figure 3.21	Schematic representing dilation of the aorta(area in red is original aorta and in green the dilated aorta area).....	97
Figure 3.22	Schematic representing potential aneurysms.....	97
Figure 3.23	Schematic representing the removal of isolated objects with same	

	Hounsfield units to the aorta.....	98
Figure 4.1:	Illustration of CAM system.....	101
Figure 4.2:	TAA detection using ellipse fitting.....	109
Figure 4.3:	TAA segmentation using ellipse fitting (red colour) and CAD segmentation result (green colour).....	109
Figure 4.4:	Ellipse diameter calculation.....	110
Figure 5.1:	Diagram of MIPS3 application.....	114
Figure 5.2:	MIPS3 platform.....	115
Figure 5.3:	Annotation window.....	116
Figure 5.4:	Annotation list.....	116
Figure 5.5:	List of annotations by different radiologists.....	117
Figure 5.6:	Two annotations selected.....	117
Figure 5.7:	Diagram illustrating intra and inter observer variability between three radiologists.....	118
Figure 5.8:	Annotations of three different segmentations, two manual one automatic by our system.....	119
Figure 5.9:	Lung segmentation.....	124
Figure 5.10:	End of lung slice detection.....	123
Figure 5.11:	Thresholding method followed by a shape analysis (degree of circularity)....	124
Figure 5.12:	Slice “box” for the detection of the thoracic aorta.....	124
Figure 5.13:	Detection of the celiac trunk.....	126
Figure 5.14:	Distance between end-of-lung and the Celiac Trunk for 30 CTA images using the parameters Tsize=6, Tcnt=6. The x-axis indicates the 40 CTA images and the y-axis denotes the distance between the obtained end-of-lung and the actual Celiac Trunk locations.....	127
Figure 5.15:	Region Growing Segmentation.....	128
Figure 5.16:	Elimination process with different parameters (a) Remove smallest object if	

	less than $\frac{1}{4}$ of largest object (b) Remove largest object if twice the size of small object (c) If three objects present in one slice remove middle object....	128
Figure 5.17:	Example of bleeding region in CTA image, reason two regions merge.....	129
Figure 5.18:	Output of detection and segmentation of thoracic aortic lumen	129
Figure 5.19:	(a) Sagittal view of lumen segmentation (b) Centreline extraction after pruning.....	132
Figure 5.20:	View of TAA including annotation of the Aorta and quantification features.....	133
Figure 5.21:	Original image (left) and right image shows the comparison between initial segmentation of CAM (green) and CAM aneurysm segmentation result using ellipse fitting (red).....	136
Figure 5.22:	Initial segmentation (green), ellipse fitting segmentation (red colour) and level set segmentation (blue colour).	137
Figure 5.23:	Volume correlation derived from manual segmentation and CAM($R=0.86$).....	141

[Page intentionally left blank]

List of Tables

Table 1:	Finding end-of-lung using different parameter combinations.....	126
Table 2:	Mean errors and standard deviation of the diameters $\bar{e}_{D_{min}}$, $\bar{e}_{D_{mean}}$ and $\bar{e}_{D_{max}}$, and for the centreline position \bar{e}_{x_0} for the two approaches investigated.....	138
Table 3:	Comparison of automated measures to manual tracing.....	140

[Page intentionally left blank]

Glossary of Words

2D	Two Dimensional
3D	Three Dimensional
AC	Active Contour
BS	Boundary Seeded Voxel Coding
CAD	Computer Aided Detection
CAM	Computer Aided Measurement
CTA	Computer Tomography Angiogram
DFS	Distance from starting point
DFB	Distance from boundary point
DICOM	Digital Imaging and Communications in Medicine
LM	Local Maximum
TA	Thoracic Aorta
TAA	Thoracic Aorta Aneurysm
MRI	Magnetic Resonance Imaging
CT	Computer Tomography
ACTA	Automatic Computerized Transverse Axial
MSCT	Multi-Slice Computer Tomography
MDCT	Multi-Detector Computer Tomography
MIAS	Mammography Image Analysis Society
GDM	Geometric Deformable Models

MRF	Markov Random Field
PACS	Picture Archiving and Communication Systems
PA	Pulmonary Artery
ICM	Iterated Conditions Modes
ROC	Receiver Operating Characteristic
ROI	Region of Interest
KNN	K-Nearest Neighbour
DDSM	Digital Database for Screening Mammography
SVM	Support Vector Machine
VOI	Volume of Interest
FAS	Fast Adaptive Segmentation
FHT	Fast Harley Transform
HT	Hough Transform
SS	Single Point Seeded voxel coding
MIPS ³	Medical Images Processing, Seamless and Secure Sharing Platform

[Page intentionally left blank]

Chapter 1

Introduction

1.1. Motivation

Our main motivation for this project has been that if an aneurysm is not diagnosed or treated within time its progressive growth may eventually cause a rupture of the aorta. The likelihood of a rupture occurring in the thoracic aortic aneurysm (TAA) depends on its size. So, there is the need for a segmentation of the aneurysm for a subsequent accurate measurement.

As a general practice, the aneurysm regions are manually segmented from the CT Angiography (CTA) images by expert radiologists before the measurement. This is an expensive, time consuming and prone to error method.

Hence, in this project we propose a completely automated computer aided detection (CAD) and measurement (CAM) system for detection of potential aneurysm in the entire thoracic aorta, which is robust and accurate and requires no human interaction, and ultimately alleviate greatly the workload burden on radiologist, as well as improving their accuracy. It will also prove to be invaluable when planning surgeries for introduction of stents for repairs of thoracic aorta as all necessary measurements are provided in our system, once again improving efficiency and valuable time in theatre.

1.2. Anatomy of the Aorta

The aorta is the largest artery in the body. It has an internal diameter around 2.5cm and a wall thickness of 2mm, in an adult. It decreases in size slightly as it runs to its terminus. It has an aortic valve which guards the base of the aorta and prevents backflow of blood during diastole [1, 9].

Different parts of the aorta are named according to its shape and location. The first part, the ascending aorta, runs posterior and to the right of the pulmonary trunk. It persists for only about 5cm before curving to the left as the aortic arch. The only branches of the ascending aorta are the right and left coronary arteries, which supply the myocardium. Its three major branches,

brachiocephalic trunk, the left common carotid artery and the left subclavian artery provide arterial supply of the head, neck , upper limbs and part of the thorax wall [1, 9] .

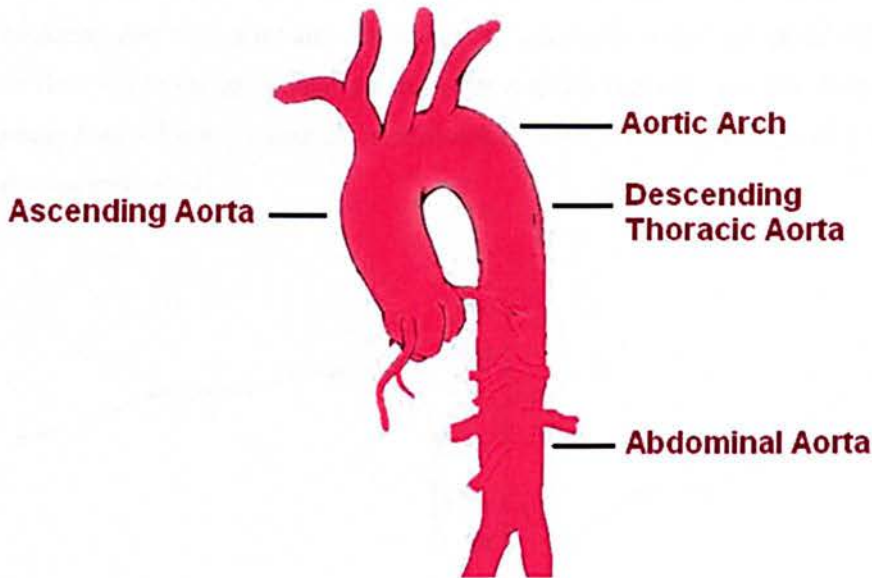


Figure 1.1: The entire aorta and its major branches Aorta [2].

The thoracic, or descending, is contained in the posterior mediastinal cavity aorta. It runs along the anterior spine from T5 to T12, at the aortic hiatus in the diaphragm where it becomes the abdominal aorta. This part of the aorta supplies the abdominal walls and viscera and ends at the L4 level, where it splits into the right and left common iliac arteries, which supply the pelvis and lower limbs [1, 9].

The thoracic aorta is composed of three layers: tunica intima, tunica media and tunica adventitia. The intima being the innermost layer and is in contact with flowing blood. This layer is thin and smooth at birth, but with ageing this layer thickens. The media is the muscular layer. The adventitia is a layer of loose connective tissue that contains blood vessels, the vasa vasorum and nerves. In the aorta the vasa vasorum penetrates into the outer third of the media. The higher elastic content of the media aids in the propulsion of blood after cardiac systole [1, 9].

1.2.1. Thoracic Aortic Aneurysms (TAA)

Thoracic aortic aneurysm (TAA) is a life-threatening condition that causes significant short and long-term mortality due to rupture and dissection. An aneurysm is defined as the dilation of the aorta greater than 1.5 times its normal diameter for a given segment. For the thoracic aorta, a diameter greater than 3.5 cm is generally considered dilated, whereas greater than 4.5 cm would be considered aneurismal [3].

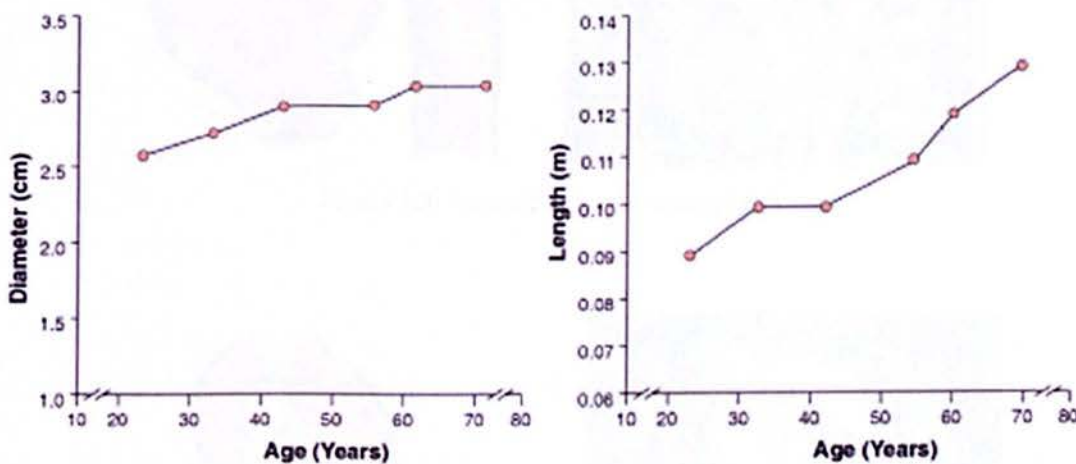


Figure 1.2: Example of the average a human's aorta diameter and length through its life [3].

Overall incidence of thoracic aortic aneurysms (TAA) is 5.9/100,000 people per year, with an average age of 65 and slightly higher prevalence in males than females. However, risk of rupture does not differ between genders [3].

Aneurysms may affect one or more segments of the thoracic aorta, including the ascending aorta, the arch, and the descending thoracic aorta. Thoracic aortic aneurysm most commonly results from degeneration of the media of the aortic wall as well as from local hemodynamic forces [3].

Weakening of the aortic wall is due to the increased shear stress, particularly in the ascending aorta. This segment of the aorta is most exposed to the pressure of each cardiac systole as well as the dynamic heart motion transmitted from each cardiac cycle. As local wall weakness causes

dilation of the aorta, wall tension increases. Small tears in the intimal (innermost) layer of the aorta can permit blood to penetrate the medial layer, leading to aortic dissection [3].

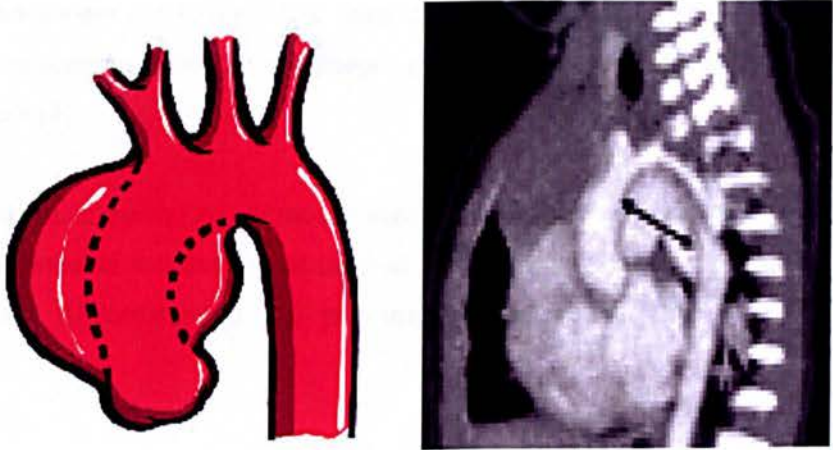


Figure 1.3: Ascending Aortic Aneurysm [5].

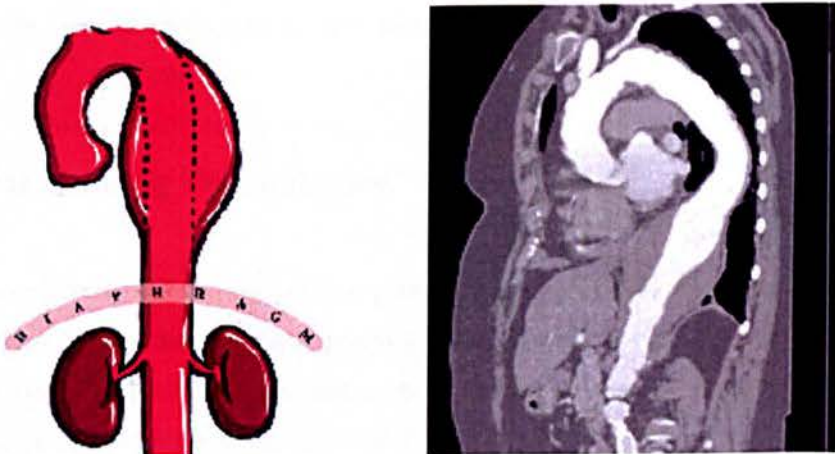


Figure 1.4: Descending Thoracic Aneurysm [5].

Most thoracic aneurysms are asymptomatic and are typically detected when imaging studies (chest x-rays, CT scans, MRI, etc) are being obtained. When aortic aneurysms reach larger sizes the symptoms are typically based on the location of the aneurysm [4].

Ascending aortic aneurysms frequently cause dilatation and leakage of the aortic valve. This can result in shortness of breath or even heart failure should the leakage be severe. Ascending aortic

aneurysms can also result in a dull pain underneath the breastbone or radiating to the upper back [4].

Aortic arch aneurysms can also produce upper chest and back pain. However, when large, these aneurysms can compress both the oesophagus and the airway resulting in difficulty swallowing and hoarseness [4].

Descending thoracic aneurysms are mostly asymptomatic, but can occasionally cause back pain. In contrast, abdominal and thoracic-abdominal aneurysms may cause a pulsating feeling in the upper abdomen. Abdominal and back pain may also be present if the aneurysm increases in size [4].

Whereas, most of the symptoms of stable thoracic aneurysms are vague and non-specific, rupture or dissection of these aneurysms produces dramatic symptoms. A ripping sensation within the chest and also severe pain in the back between the shoulder blades is the most typical complaint during thoracic aortic dissection or rupture [4].

1.3. Medical Imaging Technologies

In a medical environment, imaging technologies consist of three major components: imaging modalities such as X-ray computed tomography (CT), a secured network for the transmission of patient information, in DICOM format, and archives for the storage and retrieval of images and reports, PACS. In this section we will describe these three major components.

1.3.1. PACS

PACS is the acronym for picture archiving and communication systems, which are a network of computers serving the storage and visualisation of various digital medical imaging machines. The different computers in the PACS and the scanners communicate together through the DICOM protocol. In figure 1.5 we have a workflow diagram of the PACS systems.

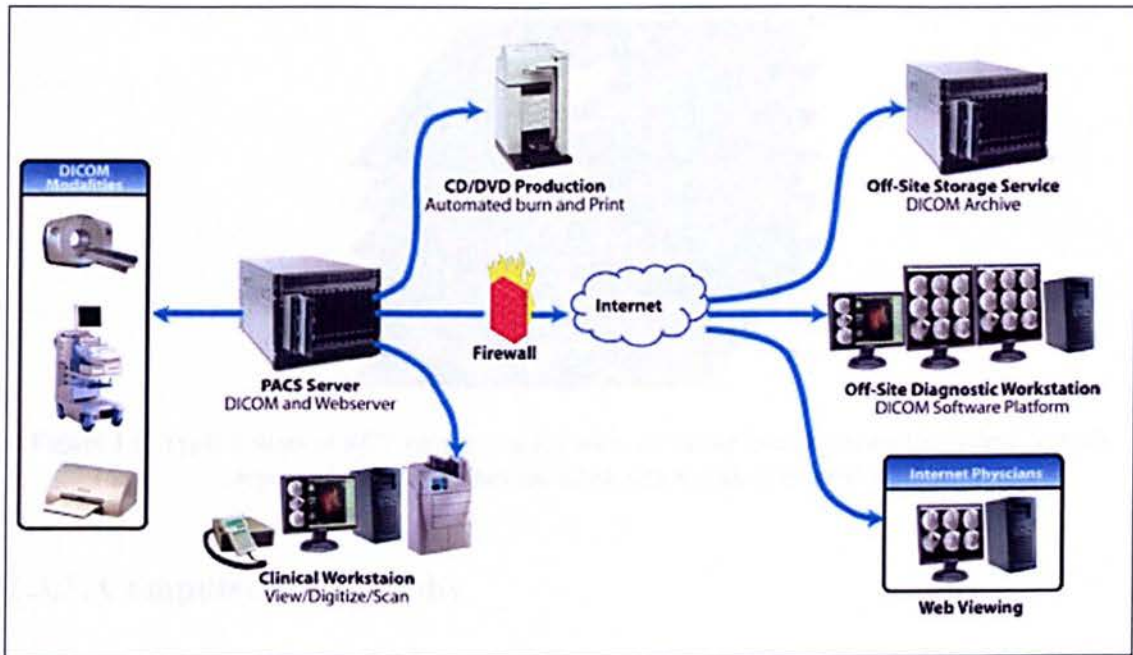


Figure 1.5: PACS workflow.

1.3.2. DICOM

DICOM stands for digital imaging and communications in medicine. It is a comprehensive set of standards for handling (printing, transmitting, storing) medical images. The acquisition of the images used in a hospital is done by exporting images from a PACS system to a CD-ROM in a DICOM file format.

These images are then imported into computer software's so that the radiologist is able to analyse them. Or as of more recent as can be seen in figure 1.5 DICOM files can be accessed online through PACS server, breaking down the physical and time barriers associated with traditional film-based image retrieval, distribution, and display [6].

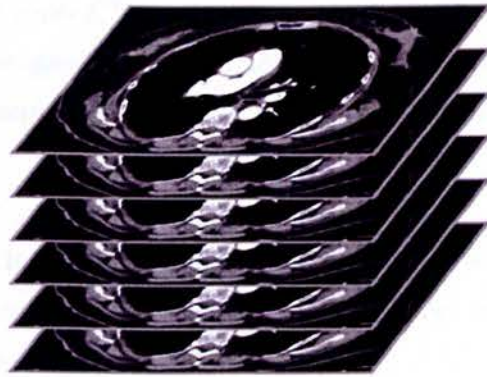


Figure 1.6: Typical slices of a CT volume that are taken at regular interval across the patient. Vessels appear white because they are filled with a contrast product [6].

1.3.3. Computer tomography

X-ray computer tomography (x-ray CT) is one of the fastest growing imaging modalities in health-care today. CT is fast, reliable, relatively inexpensive, and readily accessible. Furthermore, with recent technological advances, there is a potential for four-dimensional imaging, which includes traditional 3-D spatial imaging as well as dynamic imaging of organ function. As scan times are reduced to tens of milliseconds, a snap shot of the heart can be taken between beats, essentially eliminating all cardiac motion within the body during imaging [7].



Figure 1.7: X-Ray CT scan [8].

Prior to the development of x-ray CT, imaging of internal anatomical structure was limited to general radiography. While general radiography was a significant step above diagnostic technology prior to 1895, there were still several fundamental issues that were not solved until the advent of x-ray CT.

The three most significant challenges of general radiography were to find a way to increase x-ray absorption efficiency, reduce scatter photon contamination in the captured image and drastically reduce the superposition of anatomical structure.

X-ray absorption efficiency is determined by the percentage difference between detection and utilization of all the incident x-ray photons that reach the imaging detector. Typical x-ray film-screen efficiency was on the order of 25% prior to the introduction of x-ray CT. The sodium iodide (NaI) detectors that were used in early generations of x-ray CT were approximately 100% efficient at x-ray absorption, and current solid-state detectors have high absorption efficiency [9].

In general radiography, field sizes are chosen to cover small and large anatomical regions, according to the need of the x-ray examination. Collimation of the x-ray beam to the smallest region of interest helped reduce scatter radiation which reduces the contrast in the x-ray image.

However, the x-ray field had to be large to include all the required anatomical information, which caused significant contrast reduction in general radiography. Scatter radiation reduction was achieved in x-ray CT imaging by using a pencil x-ray beam for all the projection measurements. The small pencil x-ray beam limits the scatter component of the absorbed x-ray information.

Finally, general radiography superimposes three-dimensional anatomical information, into a two-dimensional image; this leads to uncertainty of anatomical placement of structure. X-ray CT imaging creates cross-sectional slices of anatomical information and a three-dimensional effect can be created as the clinician reviews these slices successively. Newer reconstruction algorithms can create 3D segments of extended anatomical structures. This allows a more complete assessment of any clinical abnormalities that a patient might have [9].

The development of x-ray CT imaging began in the 1960's. In 1963, Allan Cormack published findings from the first prototype CT scanner. Cormack determined the attenuation coefficients of different tissues within the body in an attempt to improve the planning accuracy of radiation therapy. In 1967 Sir Godfrey Hounsfield designed the first clinically usable x-ray CT scanner [10, 11].

Hounsfield determined that if x-ray transmissions from multiple directions through a body were collected, the internal structural information would be available in the reconstructed image. Hounsfield estimated that difference in attenuation coefficients of different tissues within the body could be determined to within an accuracy of 0.5%, thus making it possible to distinguish between different soft-tissues (as for example fat and muscle). In addition, Hounsfield realized that this type of data interpretation would only be possible by use of computer analysis. Both men earned the 1979 Nobel Prize in medicine for their pioneering work on computed tomography [9].

1.3.3.1. First Generation CT Imaging

First generation x-ray CT scanners used an x-ray tube that irradiated a pencil photon beam. The x-ray tube was rigidly attached to two side by-side NaI detectors that were placed on the opposite side of the imaging cavity. There were two detectors used to reduce the time of acquisition. The scan would be obtained from the x-ray projections measured as the tube and the detectors translated along the patient's head, then the apparatus would be rotated 1° . The acquisition process would be repeated for a total rotation of 180° . We can see a schematic of a first generation scanner in figure 1.8.

First generation CT scanners were only capable of imaging the head, as the scanners used a 'water-box' to encase the head for accurate reconstruction of the acquired data. The water-box ensured that each x-ray beam projection passed through equivalent distances of tissue and water. Therefore, the water-box allowed for dynamic range optimization of the detectors and helped limit the corrections required for the effects of x-ray beam hardening [9].

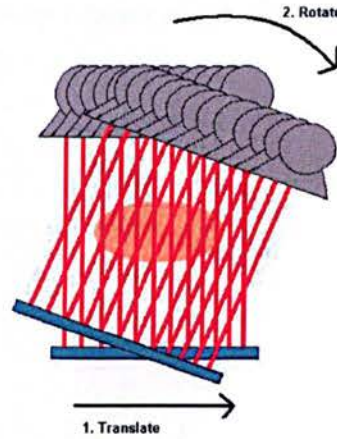


Figure 1.8: First generation CT scanner [12].

The dynamic range optimization allowed the detectors to be sensitive to a very limited range of energies and intensities. Beam hardening happens when the average energy in a photon beam shifts higher because of x-ray beam attenuation. All x-ray tubes produce polychromatic radiation and lower energy photons are preferentially attenuated at shallower depths within tissue. The mean energy of the photon beam shifts higher. As each CT projection traversed through the same distance of tissue and water, the average energy of the detected photon beam was similar for each projection [9].

In 1973, development on the Automatic Computerized Transverse Axial (ACTA) Scanner began and involved whole body image acquisition. It incorporated various characteristics that are still used on CT scanners including, the movement of the table through the CT gantry, gantry angulations, use of a laser section indicator to optimize patient positioning, and the elimination of the water-box. The detectors were adjusted to accommodate for the larger dynamic range of intensities. Beam hardening effects were empirically incorporated into convolution filter parameters and image reconstruction algorithms [9].

1.3.3.2. Second Generation CT Imaging

In the second generation of design of CT scanners, the two row detectors were replaced with an array of X detectors per row within the field of a fan beam. More detectors per row meant a

decrease in imaging time per slice by a factor of $1/X$. Below in figure 1.9 is a schematic of the second generation CT scanner [9].

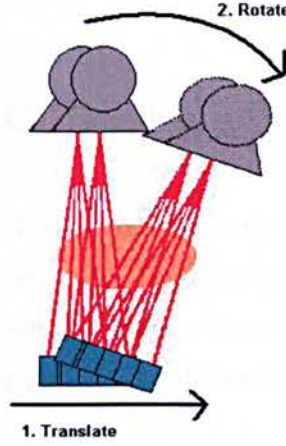


Figure 1.9: The second generation CT scanner [12].

Another development included the incorporation of the standard CT number scale. This number scale is also known as the Hounsfield number (H), and relates the relative attenuation coefficients of different tissues (μ) to that of the attenuation coefficient of water (μ_{water}).

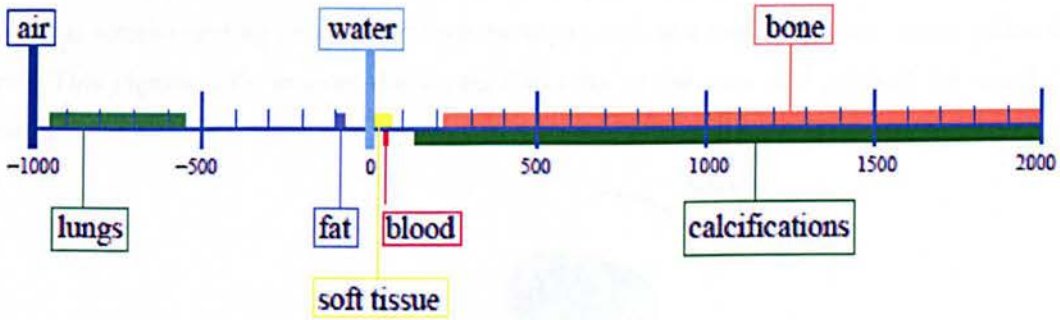


Figure 1.10: Hounsfield units scale [12].

CT numbers are calculated using Equation 1.1:

$$H = 1000 \left(\frac{\mu - \mu_{water}}{\mu_{water}} \right) \quad (1.1)$$

The speed of these scanners was limited to the inverse of the number of detectors in the scanner. For example, a head scan that previously took five minutes now took $5min/X$. However,

because the reduction of the time of acquisition was constrained, extensive use and development of this generation of CT scanner was limited [9].

1.3.3.3. Third Generation CT Imaging

Third generation CT scanners use an x-ray fan beam that covers the whole patient, and all the projections are acquired by a detector array. New scanners have multi-row detector arrays that allow more than one slice to be imaged at a time. These multi-row detector arrays have been expanded extensively, now allowing for 320 slice detector arrays [9].

The tube and the detector array are rigidly linked (as in previous generations) and a pulsed beam is used to reduce angular smearing of the photons. In turn, the pulsed photon beam helps reduce some of the patient dose and extend the life of the x-ray tube [9].

The CT scanner consists of a circular gantry, where the x-ray tube and multi-row detector array are on a slip-ring power contact, which sits inside the gantry. The slip-ring contact allows for a continuous rotation during imaging without having to stop and unwind power cables within the gantry. This significantly reduces the acquisition time of the scan and allowed for spiral CT scanning.

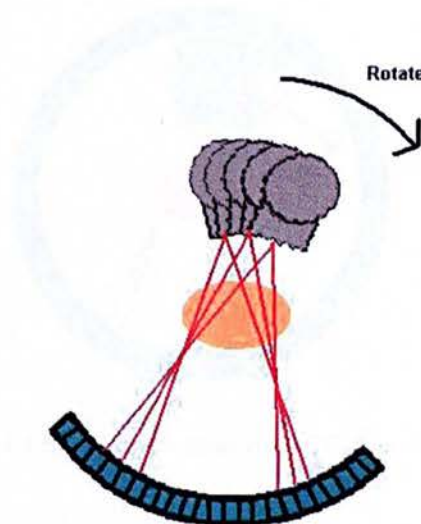


Figure 1.11: Third generation CT scanner [12].

As previously mentioned, the x-ray tube emits a fan beam that passes through the entire patient in one pulsed exposure, eliminating the translation of the tube and detectors along the width of the patient. Solid-state detectors are currently used and they have an x-ray absorption efficiency of approximately 80%.

Solid-state detector arrays also require the separation of the detector elements within the array by small tungsten or lead plates called septa. The septa form an inherent scatter rejection grid. Figure 1.11 is a schematic of the third generation CT scanner [13].

1.3.3.4. Fourth Generation CT Imaging

The fourth generation of x-ray CT scanner consisted of a ring of detectors (of over one thousand detectors) that covers the whole scanner, and the x-ray tube is rotated around the patient. A schematic representation can be seen in figure 1.12.

In the fourth generation of CT scanners, the imaging artifacts were less evident as the detector inaccuracies were spread across the image uniformly.

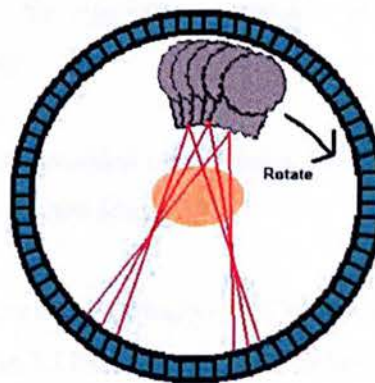


Figure 1.12: The fourth generation CT scanner [12].

Due to the sheer number of detectors required the main disadvantages of this scanner was the installation and its maintenance cost. Furthermore, due to the finite number of detectors and their rigid placement within the gantry, angular projection samples were limited.

There was also a need for a larger ring diameter, due to the tube often being inside the detector ring, which caused excessive heat loading on the x-ray tube. Unfortunately, this would cause a significantly shorter x-ray tube life. Ultimately, due to the initial cost and the cost of maintenance, most of scanners of this design have been phased out in favour of third generation CT scanners [9].

1.3.3.5. Image reconstruction

X-ray CT reconstructs a 2D image from measurements of x-ray attenuation taken from different angles within a plane. For each measurement the projection intensity (I) is the line integral of the attenuation coefficients (μ) along the path (x). I can be approximated by Equation 1.2 where I_0 is the incident photon intensity measured at the source.

$$I = I_0 e^{-\sum_i \mu_i x_i} \quad (1.2)$$

The main task of x-ray CT image reconstruction is to use the information stored in I and estimate the attenuation distribution within the object. This is not a trivial task, and as the methods of obtaining the x-ray flux measurements became more sophisticated (multi-row detectors, spiral CT scanning), the algorithms required to reconstruct the images in a timely matter must develop accordingly.

All modern x-ray CT image reconstruction algorithms rely on the principles and ideas of filtered back projection to create reconstructed images [9].

The finite numbers of projections taken during x-ray CT imaging are used to reconstruct the two dimensional image slices. Figure 1.13(a), illustrates a simple example of an object that has been imaged with four projections (P1-P4). Each projection is a simple line integral of the intensity measurements. Each measured intensity is assumed to be uniform through the whole object being imaged and the intensity measurements are linearly ‘smeared’ in the process of back projection (BP1-BP4). In figure 1.13(b), all back projection are added together to create the reconstructed image [9].

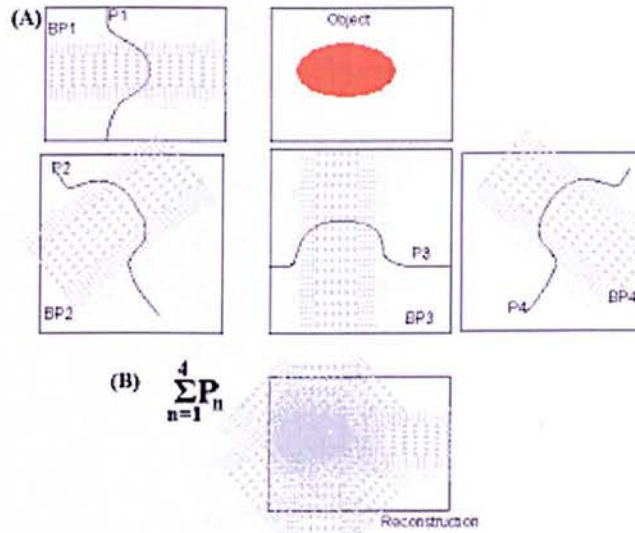


Figure 1.13: (a) Object imaged with four projections (P1-P4). (b) Reconstructed image [14].

Algorithmic filtration convolves the back projected data with data filters to add edge enhancement, smooth out noise and remove common artifacts from the reconstructed image.

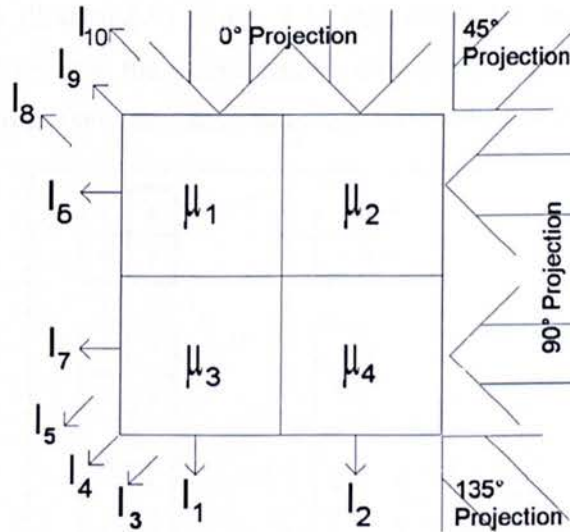


Figure 1.14: A 2x2 matrix gives a simple visual schematic of CT linear back projection [13].

Back-projection can also be illustrated numerically using a 2x2 matrix, as seen in figure 1.14. If four projections of data from angles 0°, 45°, 90° and 135° are taken, ten intensity measurements will be obtained. I_1 and I_2 correspond to measured values from the 0° projection; I_3 , I_4 and I_5 correspond to measured values from the 45° projection, etc. The intensity (I_n) for each of the 10 projections are given in Equation 1.3.

$$\begin{aligned}
I_1 &= I_0 e^{-(\mu_1 + \mu_3)x} \\
I_2 &= I_0 e^{-(\mu_2 + \mu_4)x} \\
I_3 &= I_0 e^{-\mu_1 x} \\
I_4 &= I_0 e^{-(\mu_2 + \mu_3)x} \\
I_5 &= I_0 e^{-\mu_4 x} \\
I_6 &= I_0 e^{-(\mu_1 + \mu_2)x} \\
I_7 &= I_0 e^{-(\mu_3 + \mu_4)x} \\
I_8 &= I_0 e^{-\mu_3 x} \\
I_9 &= I_0 e^{-(\mu_1 + \mu_4)x} \\
I_{10} &= I_0 e^{-\mu_2 x}
\end{aligned} \tag{1.3}$$

When each of the linear attenuation coefficients $[\mu_1, \mu_2, \mu_3, \mu_4]$ are replaced with numeric values (for example: $[0, 2, 1, 3]$), the mathematics of back projection reconstruction is illustrated in figure 1.15.

The first projection is illustrated in Figure 1.15 (b), where the first column elements are assigned the value I_1 . Similarly, the second column elements are assigned the value of I_2 . For each of the next three projections, the intensities are added as illustrated in Figure 1.15(c-e).

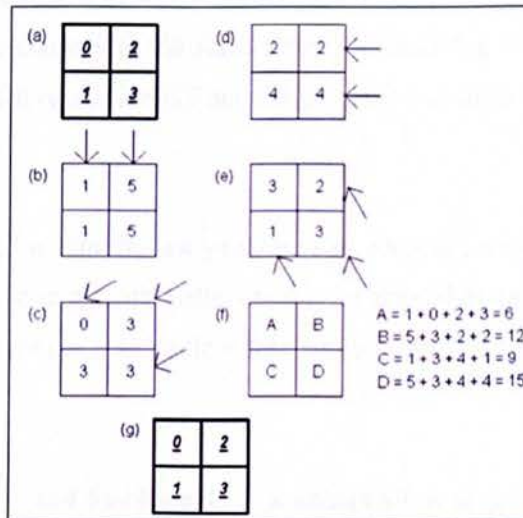


Figure 1.15: (a) Original 2 x 2 matrix with numerical values. (b-e) show the back-projected linear attenuation intensities measured for each projection and (f) shows the reconstructed matrix equations. The reconstructed matrix is normalized by subtracting the smallest element value and then dividing by the greatest common factor (6) yielding (g) the original matrix.

The first step of the imaging reconstruction is to determine the intensity values from Equation 1.3. One method is to assume that the intensity is represented by the linear attenuation coefficients, with all other factors (I_0, x) held constant. For this example, the intensity values can be represented by the sum of the corresponding linear coefficients of [1, 5, 1, 3, 3, 2, 4, 1, 3, 2] respectively [9].

For each of the next three projections, once all the intensity measurements are included, a constant value (i.e. the smallest summation of the total intensity for a matrix element) and in this example, (6) is subtracted from each matrix element. The values are reduced by the greatest common factor (3), and the original attenuation values are obtained. The values are reduced by the greatest common factor (3), and the original attenuation values are obtained, as shown in Figure 1.14(f). [9].

1.3.3.6. Computed Tomography Angiography

Computed Tomography Angiography (CTA) has evolved from the traditional X-rays computed tomography. With the development of fast CT scanners, the scan times have decreased substantially, which has allowed to scan a particular anatomic region of the body while contrast medium is injected intravenously at the same time. The resulting bright vascular opacification combined with high-spatial resolution CT acquisition gave rise to so called CT-Angiography, or CTA.

Modern CTA has evolved within the last years into an accurate, robust, and cost effective non-invasive imaging technique in patients with coronary or arterial diseases, thanks to the advent of helical multi-slice CT scanners which allow fast and precise 3D medical imaging of a human body.

Current state-of-the-art 16- and 64-channel CT scanners allow acquisition of a set of transverse images representing the whole area of interest in less than 30 seconds. With a simultaneous use of contrast medium, the produced images are well-suited for angiographic purposes and due to the better contrast resolution of CT when compared to conventional angiography, contrast

medium needs not be injected directly into the arterial system, but only into an arm vein, intravenously. CTA is thus much less invasive and less harmful for the patient.

A CTA dataset of the thoracic aorta consists of approximately 300–500 images 512×512 pixels each with 4096 levels of grey and resolution below 1mm^3 is produced. Within such dataset, vessels manifest densities that are different to those of the surrounding tissue, due to the contrast-medium enhancement of blood. As the number of transverse slices is very high, the radiologic interpretation of CTA dataset is laborious and lengthy and dedicated post-processing tools that generate a small set of easily interpretable images are typically used.

1.3.3.7. CT vs MRI

CT provides images which have a high spatial resolution and a comparable short acquisition time. There is also a good contrast between bone and soft-tissues. However, the contrast between different types of soft-tissues can be poor and this is overcome by using contrast agents.

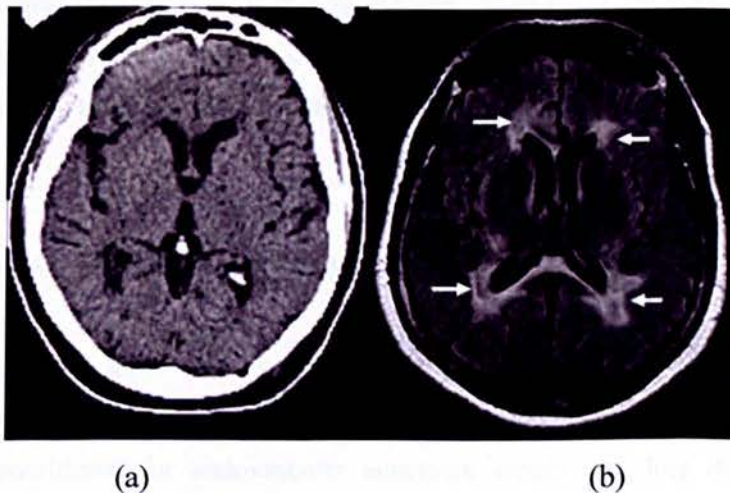


Figure 1.16: Comparison of CT and MRI images. (a) CT scan and (b) MRI showing the increased sensitivity that MRI adds in visualizing brain lesions, such as those in MS (arrows) [15].

CT is preferred to MRI for patients with cardiac pacemakers. Due to its short acquisition times, it is also suitable for patients who may feel claustrophobic inside MRI scanners. However, major disadvantage of CT is the relatively high exposure dose of X-ray radiation.

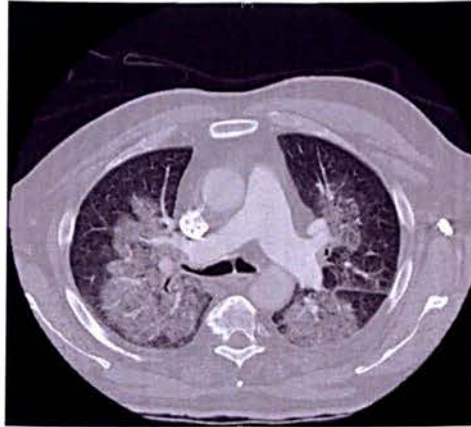


Figure 1.17: CT scan of the chest.

In cardiac imaging, CT is commonly used for imaging the arteries. Ultrafast CT is used for measuring the amount of calcium deposits in arteries. It is also possible to acquire multi-slice images using multi-slice CT (MSCT) and multi-detector helical CT (MDCT) scanners. These are now commonly used for assessing cardiac structure and morphology [15].

CT is fast, reliable, relatively inexpensive, and readily accessible. Furthermore, with recent technological advances, there is a potential for four-dimensional imaging, which includes traditional 3-D spatial imaging as well as dynamic imaging of organ function. As scan times are reduced to tens of milliseconds, a snap shot of the heart can be taken between beats, essentially eliminating all cardiac motion within the body during imaging [16].

1.4 . Techniques of Aortic Aneurysm diagnosis and repair

Accurate assessment of aortic anatomy is essential to the success of endovascular aneurysm repair. A number of imaging modalities have been used in the preoperative assessment of patients being considered for endovascular aneurysm repair including duplex ultrasound, magnetic resonance angiography and spiral CTA. CTA provides a non-invasive means to evaluate the arterial system throughout the body and has become an increasingly important diagnostic tool.

Although aortography is considered the gold standard for aortic imaging, the volumetric acquisition of spiral CT offers several advantages, particularly for evaluation of overlapping structures in the chest [17].

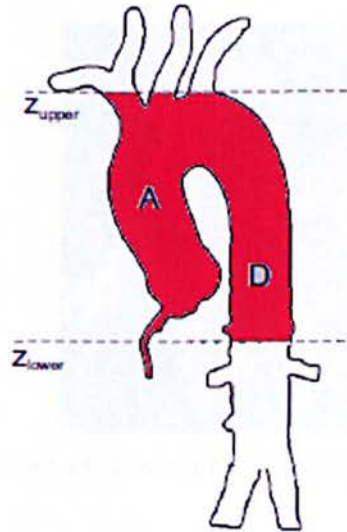


Figure 1.18: Illustration of the region of interest [17].

Studies as early as 1995 demonstrate that the sensitivity of CTA exceeds that of conventional angiography for the detection of traumatic aortic injury. Since then, the indications for CTA of the thoracic aorta have expanded to include imaging of thoracic aortic aneurysm, thoracic aortic dissection, and intramural haematoma [17, 18].

The use of CTA for evaluation of thoracic aortic aneurysm can be to accurately identify the size and extent of the aneurysm as well as the involvement of aortic branch vessels. 3D reformations can be used for the accurate determination of path lengths and to facilitate measurements of neck and landing zone dimensions for the purposes of device sizing. These techniques are helpful as an aid to surgical or endovascular repair planning and can be used in follow-up to determine the successfulness of an intervention [17].

Treatment for an aneurysm depends on its size and location and your general health. If the aneurysm is small and you have no symptoms, it might be suggested a "watch-and-wait" approach with regularly scheduled images of the aneurysm to check the size. However, if your aneurysm is large enough, or if the aneurysm is growing more than 1 centimetre per year, surgery may be necessary [17].

Several prostheses and delivery systems have been developed for endovascular aortic aneurysm repair over the last decade. For example, a stent graft, which is a tubular device, which is composed of special fabric supported by a rigid structure, usually metal [18].



Figure 1.19: Example of bifurcation aortic stent graft [19].

Despite some early failures with first generation stent-grafts in the early to mid 1990s, currently available stent-grafts can be expected to achieve successful primary aneurysm exclusion in at least 90% of patients [18].

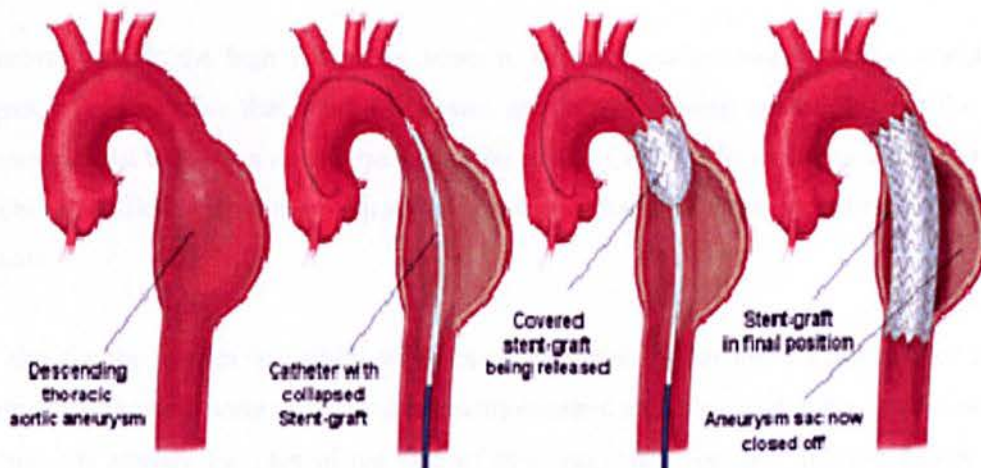


Figure 1.20: Illustration of a stent graft being positioned in the aorta for repair of aneurysm [18].

Overall, the development of stent-grafts for repair of distal descending thoracic aneurysms may be viewed as a success story with encouraging pre-operative and mid-term results. Yet, satisfactory endovascular solutions to arch and proximal thoracic aneurysms have so far remained elusive [18].

1.5. Research Objectives

As a general practice, the aneurysm regions are manually segmented from the CTA images by expert radiologists before the measurement. This task is difficult, inefficient and time consuming, even for trained professionals. Additionally, the result depends on the user and has limited reproducibility. Therefore, there is a real need for the development of a fully automated CAD system.

Developing such system can prove to be extremely challenging due to the anatomical shape the vessel such as the thoracic aorta and its aneurysms as due to a vessel curved shape anatomy, it is difficult to measure the true diameter of the aorta. Another challenge is differentiation the different organs (tissues, bone, etc) as they often have similarities in pixel intensities.

Our main goal is to design an algorithm which is robust and computer efficient, so it is viable to be used in the radiologist work environment to ultimately alleviate greatly their workload burden on by reducing image reading time.

Moreover, due to the high volume of scans to be read, reader fatigue and the complexity of images, it is inevitable that some aneurysms are currently being missed without the use of a computer assist tool. As a result, the utilization of this CAD/CAM tool would serve to improve not only the efficiency but the accuracy of aneurysms detection when screening is performed on patients.

We aim for the system to helpful when planning surgeries for the introduction of stents for repair of the thoracic aorta as all measurements required are calculated in the system, so that the surgeon has already the idea of the size of stent necessary for each specific patient prior to entering the surgical theatre.

1.6. Thesis Organization

The remainder of this thesis is organized as follows:

Chapter 2 contains a literature review of computer aided detection systems developed until this date followed by reviewing image processing theoretical ideas involved in the implementation of this project, such as pre-processing, segmentation and classification.

Chapter 3 provides the proposed methodologies used to implement proposed CAD system, such as automatic seed selection, lumen segmentation, centreline detection and orthogonal plane to centreline. If potential aneurysms are identified in this chapter the program continues to CAM system for quantification of the thoracic aorta.

Therefore chapter 4 introduces the methodologies used to implement CAM component of our developed system, where an ellipse fitting method is innovatively used in such application for characterization of the aneurysm features.

Chapter 5 discusses the experimental the results obtained and validation of our CAD and CAM components.

Finally in Chapter 6 concludes the thesis and we suggest further research possibilities where this system can be adapted to other application or even include further feature extraction of connected vessels to the thoracic aorta.

Chapter 2

Computer Aided Detection (CAD)

Several CAD systems have been developed in different medical applications but currently no fully automated CAD system for detection of thoracic aneurysms is available on the market. The only systems available focus on detection of classifications or focus only in a small section of the aorta, never detecting the entire vessel.

In this chapter we start by reviewing some CAD systems that have already been developed so far for different medical imaging analysis such as in mammography, brain, colon, etc. We then review CAD systems that are more closely related to our own system for detection of aneurysms.

After reviewing the CAD systems available to date, we review methodologies used for thoracic aortic detection. These references were used to gain an understanding of the ideas and concepts required to implement a system that will meet the requirements we have set out in our objectives.

2.1. CAD Literature Review

Computers are playing an increasingly large role in radiology. In conventional radiography, x-ray images were recorded on screen-film systems, while today's radiologists view digital radiographs on display monitors. Computers have been vital in the development of medical imaging technology - without computerized reconstruction, CT and MRI imaging would not be possible.

CAD is an active area of research, which focuses on the identification of pathologies and their development such as lesions in the breast and lungs via x-ray projection images. As the name of the application indicates, the system only aids radiologists by providing a "second opinion" and can only be used in the first stage of examination. The identification process always requires some form of segmentation.

2.1.1. Mammography CAD

Songyang Yu *et al.* developed a CAD for the automatic detection of clustered microcalcifications in digitized mammogram films. The proposed system consisted of two main steps. The first step consisted of the potential micro calcification pixels in the mammograms being segmented out by using mixed features based on wavelet features and gray level statistical features, and labelled into potential individual microcalcification objects by their spatial connectivity. The second step consisted of the individual micro calcifications being detected by using a set of 31 features extracted from the potential individual microcalcification objects [20].

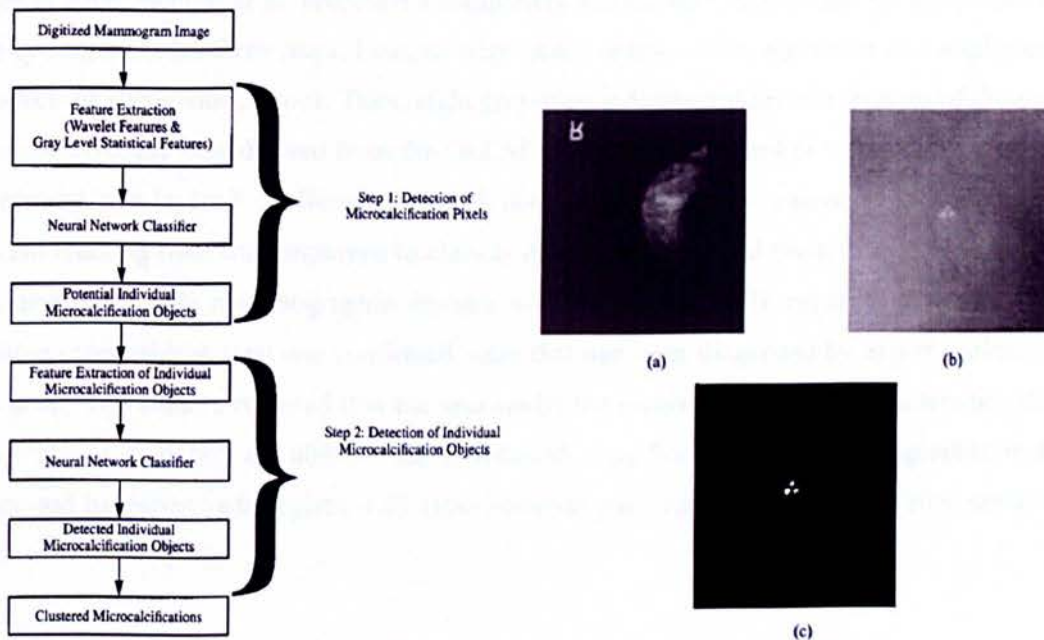


Figure 2.1: Flow chart of Songyang Yu *et al.* CAD system. (a) A mammogram from the database. (b) A cluster of microcalcifications in (a). (c) The ground truth image corresponding to the cluster of microcalcifications in (b) [20].

The author analyzed these features using general regression neural networks via sequential forward and sequential backward selection methods. The classifiers used in these two steps were both multilayer feed forward neural networks. In this study the system gave quite satisfactory detection performance. In particular, a 90% mean true positive detection rate is achieved at the cost of 0.5 false positive per image where mixed features were used in the first

step and 15 features selected by the sequential backward selection method are used in the second step [20].

S. Liu *et al.* (2001) proposed a multiresolution scheme to detect spiculated lesions. The image was decomposed into a multiresolution representation and four features were extracted for every pixel at each resolution. In their experiments, the authors selected 19 mammograms containing spiculated lesions from the Mammographic Image Analysis Society (MIAS) database. The authors reported 84.2% true positive detection at less than 1 false positive per image, and 100% true positive detection at 2.2 false positives per image. [21]

Later in 2006, Bellotti *et al.* proposed a completely automated CAD system for mass detection. The system included three steps. First, an edge-based segmentation algorithm was implemented to select the suspicious regions. Then, eight gray-tone independent texture features of the region of interest (ROIs) were derived from the GLCM at four angles $\theta=k\pi/4$ ($k = 0, 1, 2, 3$). Finally, a supervised two-layered feedforward neural network, which was trained with the gradient-descent learning rule, was employed to classify masses from normal tissues. In their experiment a database of 3369 mammographic images, which included 2307 negative cases and 1062 positive cases with at least one confirmed mass that had been diagnosed by expert radiologists, was used. The authors reported that the area under the receiver operating characteristic (ROC) curve was $A_z = 0.783 \pm 0.008$ for the ROI-based classification. For mammographic images diagnosed by expert radiologists, 4.23 false positives per image were found at 80% sensitivity of mass detection [22].

In 2007 Eltonsy *et al.* proposed a multiple-concentric-layers-based algorithm to detect masses in mammograms. The algorithm consisted of three steps. First, the breast regions of screening mammograms were pre-processed by segmentation and granulation techniques. Then, the suspicious focal areas were detected using knowledge-based reasoning. Finally, two different criteria were applied to eliminate the false positives. In their experiment, 270 CC views of mammographic cases with biopsy-proven malignant masses from the Digital Database for Screening Mammography (DDSM) database were selected. Half of the cases were used for training and the other half were used for testing.

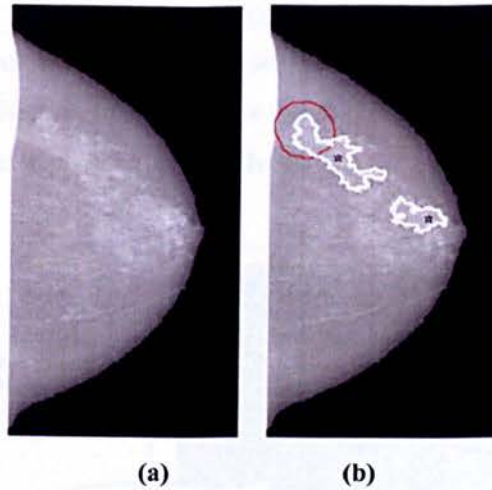


Figure 2.2: (a) Original breast image after breast region segmentation and (b) CAD detected masses denoted with asterisks. In one case, the centroid of the focal activity layer is outside the physician's mass annotation (shown in red) [23].

The authors reported that the test detection rates were 92%, 88%, and 81% sensitivity at 5.4, 2.4, and 0.2 false positive marks per image, respectively [23].

Later in 2007 an automated mass detection method was presented by Timp *et al.* to detect temporal changes in mammographic masses between two consecutive screening rounds. Two kinds of temporal features, difference features and similarity features were designed to realize the interval change analysis. A support vector machine (SVM) was employed as a classifier to detect the temporal changes in mammographic masses. The classification performance was evaluated with and without the use of temporal features. In their experiment, the database consisted of 465 temporal mammogram pairs containing 238 benign and 227 malignant cases. The authors reported the area under the ROC curve was $Az = 0.74$ without temporal features and 0.77 with the use of temporal features [24].

2.1.2. Brain CAD

There are several CAD systems that have been developed so far, such as the Kobashi *et al.* (2006) method to extract the cerebral artery from the MRA images and apply a thinning procedure to derive the skeleton of the artery. The skeleton is then dilated to generate an approximate reconstruction of the normal vessel. This reconstruction is then subtracted from the

segmented artery in order to identify potential candidates of aneurysm. False positive reduction is based on evaluating some feature values with respect to the shape and intensity of the aneurysms candidates. However, this method is based on the exact extraction of cerebral artery and estimation of normal artery which is a challenging task in the CTA dataset [25].

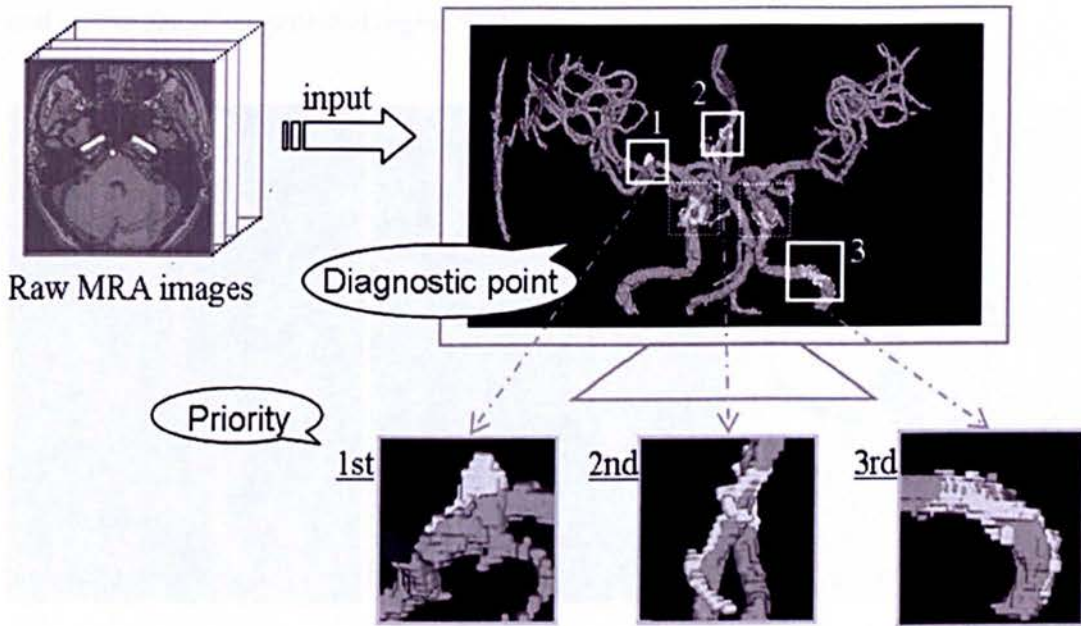


Figure 2.3: Kobashi *et al.* proposed CAD system [25].

Y. Uchiyama *et al.* in 2007 developed a CAD scheme to assist radiologists in identifying lacunar infarcts on MR images using modular classifier technique. The detection of asymptomatic lacunar infarcts on magnetic resonance (MR) images are important tasks for radiologists to ensure the prevention of severe cerebral infarction. However, their accurate identification is often a difficult task. The authors first segmented the cerebral region in the T1-weighted image by using a region growing technique. For identifying the initial lacunar infarcts candidates, white top-hat transform and multiple-phase binarization were then applied to the T2-weighted image. A rule-based scheme and a neural network with 12 features were employed as the first step for eliminating FPs. The modular classifier was then used for eliminating three typical sources of FPs. As a result, the sensitivity of the detection of lacunar infarcts was 96.8% with 0.30 FP per image [26].

In 2010 Lauric *et al.* proposed a detection method which takes as input a segmented 3D vasculature using 3DRA and CTA. Then the centreline of the vascular tree is constructed and short branches in the centreline are considered as potential locations of the aneurysm. A measure called the writhe number is computed for the local neighbourhood and regions with nonzero writhe numbers are reported as potential aneurysms. False positive reduction is applied based on the size of the potential region [27].

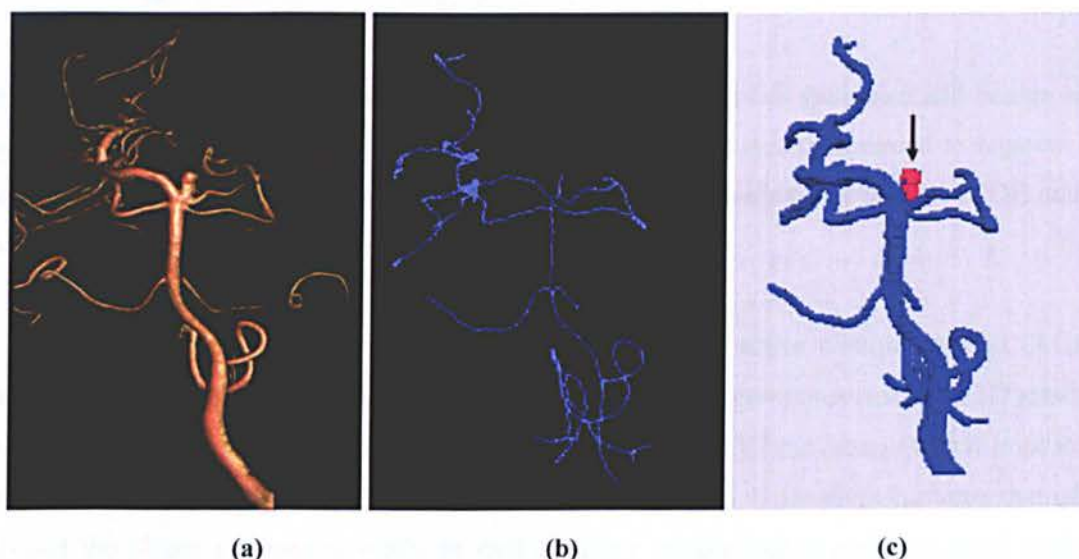


Figure 2.4: Aneurysm detection result of a patient in Lauric *et al.* (a) Original 3D-rotational angiography. (b) Corresponding medial axis of the 3D-RA dataset. (c) Detection results. Positive results were coloured in red. Black arrows point to true positives [27].

In the same year Robert D. Ambrosini *et al.* developed an automated approach applied specifically for the detection of metastases on brain MR scans. The basis of the algorithm is a 3-D template matching between MR image features and 3-D spherical tumour appearance models constructed to represent typical geometrical patterns of brain metastases. The algorithm results were encouraging as they represent a high detection rate and a manageable number of false positives without any restrictions having been placed on target nodules with regard to size, heterogeneity or whether a metastasis' morphology has been altered by treatment with radiation prior to the patient's scanning.

To make sure of only detecting nodules the author used a diameter constraint on the algorithm (diameter greater than or equal to 5 mm). In his research the major limitation for the algorithm was the possibility that the brain metastases to be detected may differ considerably from the

hypothesized spherical morphology and intensity profile represented by our 3-D tumour appearance models. His work concluded that the system developed can reduce the number of spatial positions that need to be examined from potentially thousands to less than one per slice in most datasets[28].

2.1.3. Lung CAD

In 2006 Ted W. Way *et al.* developed a CAD system that classifies malignant and benign lung nodules found on CT scans. It claimed to be a fully automated system designed to segment the nodule from its surrounding structured background in a local volume of interest (VOI) and to extract image features for classification.

The nodule segmentation algorithm consisted of using a 3D active contour method (AC), a model based on a 2D AC with the addition of three new energy components such as 3D gradient (which guides the active contour to seek the object surface), 3D curvature (which imposes a smoothness constraint in the z-direction) and mask energy (which penalizes contours that grow beyond the pleura or thoracic wall), as well as using morphological and gray-level features were. It was concluded that the lung nodule volumes segmented by the 3D AC model for best classification were generally larger than those outlined by the LIDC radiologists using visual judgment of nodule boundaries [29].

J. Tong *et al.* in 2007 presented an automatic CAD scheme that identifies the true positive nodule candidates in lung field when they are in the biologically early stage of their evolution. The scheme is based on HRCT (high resolution CT) images which have the fine isotropic resolution and have the advantage that the absolute CT value can be directly used for recognition of nodules and rejection of false positive candidates [30].

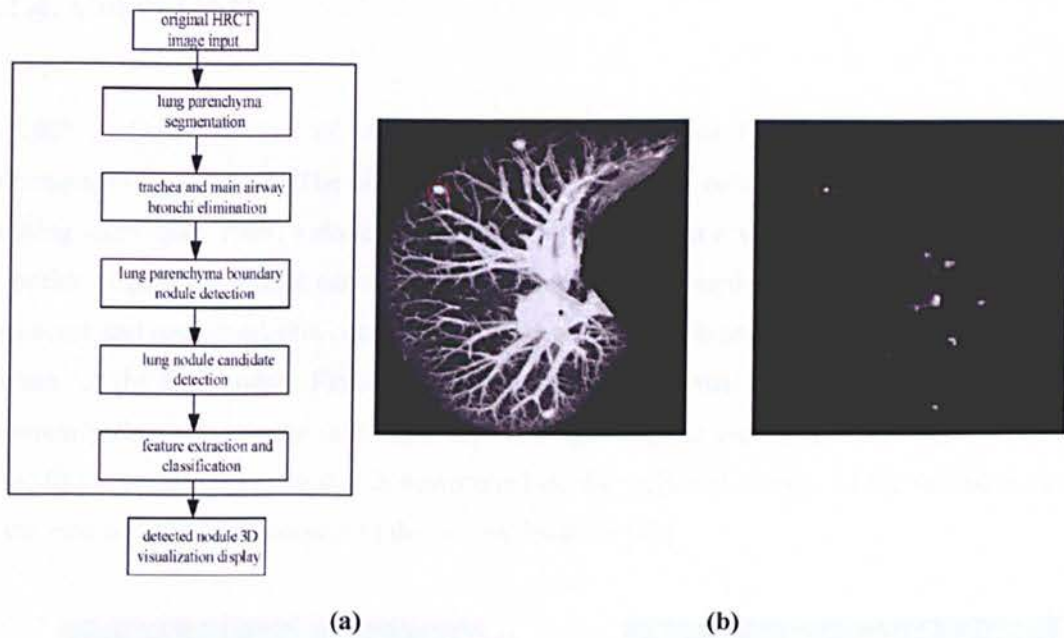


Figure 2.5: J. Tong *et al.* proposed CAD system flowchart. A nodule in the right lung lobe (red line) is illustrated in (a) and detected in (b) with authors CAD system [30].

The proposed method work was divided into steps: the segmentation of lung parenchyma, the detection of suspicious nodule candidates, the feature extraction and classification. The authors used adaptive threshold segmentation, math morphologic, Gaussian filter and Hessian matrix algorithms. All the algorithms used in the process were fully automated without the need for any user interaction. In the whole process adaptive threshold segmentation, math morphologic, Gaussian filter, Hessian matrix algorithms are used [30].

X. Ye *et al.* in 2009 proposed a computerized lung nodule detection approach and evaluated the performance of the scheme on two CT data sets. A pre-processing stage was imported to get lung fields and smooth the 3D CT sequences. The method developed by the authors is multi-step, including lung field's segmentation, initial nodule candidate's enhancement, enhanced voxel feature extraction, voxels classification with SVM and nodule decision rule. By using a 3D selective enhancement filter, the initial nodule voxels were obtained. Then by combination of SVM classifier and a decision rule, the authors achieved 0.9375 sensitivity with 4.6 FPs per case. Nevertheless, it should also be noted that the centre of enhanced nodule region are the most sensitive region when detecting lung nodules. The authors concluded that the performance of a lung CAD system can be improved by analyzing the 3D voxel characteristic [31].

2.1.4. Colon CAD

In 2007 J. Dehmeshki *et al.* developed a fully automated CAD system for use in CT-colonography application. The algorithm first segments the colon using a fuzzy based region growing technique. Then, a skeletonization method based on a voxel coding scheme to define an optimum path for virtual camera is applied on the segmented colon. The optimum path is a connected and one-voxel-thin centreline of a 3D object, which provides the location of a virtual camera for the fly-through. Finally, a smooth and stable virtual camera view direction on the optimum path is recursively calculated based on updating the view direction of the current site by adding a deviation vector that is determined by the weighted average of the deviation vector of the next n voxels with respect to the current location [32].

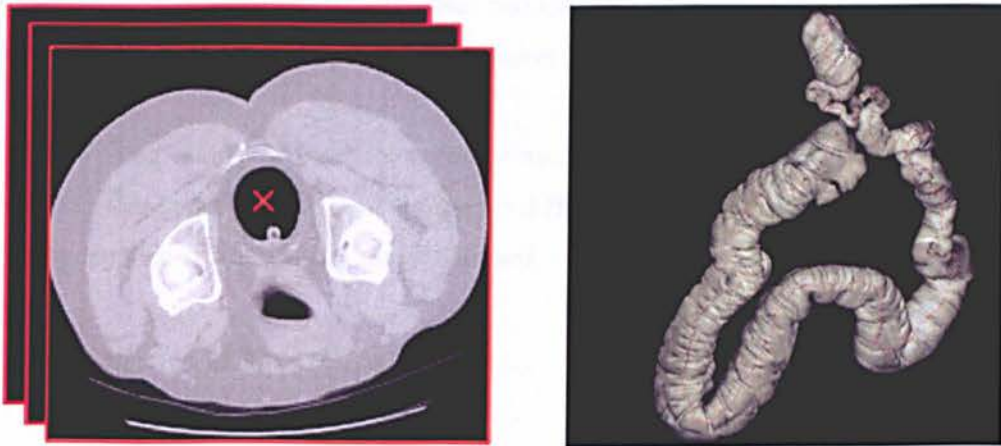


Figure 2.6: A cross section of a colon data (a) and its colon segmentation and skeletonization result (b) of J. Dehmeshki *et al.* proposed CAD system [32].

V. Ravesteijn *et al.* in 2010 proposed a CAD system for computed tomography colonography that orders the polyps according to clinical relevance. The CAD system consisted of two steps: candidate detection and supervised classification. The characteristics of the detection step lead to specific choices for the classification system. The candidates were ordered by a linear logistic classifier (logistic regression) based on only three features: the protrusion of the colon wall, the mean internal intensity, and a feature to discard detections on the rectal enema tube. This classifier can cope with a small number of polyps available for training, a large imbalance between polyps and non-polyp candidates, a truncated feature space, unbalanced and unknown

misclassification costs and an exponential distribution with respect to candidate size in feature space. The authors CAD system was evaluated with data sets from four different medical centres. Due to this they were able to conclude that the CAD system generalizes to data from different medical centres and with different patient preparations, which is a vital characteristic for applications in large-scale screening of colorectal polyps [33].

2.2. Thoracic Aorta CAD Literature review

In the previous section we have made an exhaustive review of CAD systems available to date in the many other applications other than for the thoracic aorta detection. From our literature review, no fully automated CAD/CAM system has been developed of the thoracic aorta to this date, but we will review systems which detect certain areas of the aorta and systems that are developed for detection of classification in this section.

In the case of using a CAD system for a cardiovascular disease patient, both MR and CTA images can be used. In section 2.2.1 we discuss the different CAD systems for the thoracic aorta are both when applied in MR and CT image data sets.

2.2.1. TA CAD in MRI

Rueckert *et al.* in 1997 used deformable models in tracking of the aorta in cardiovascular MR images. The system tracks the shape of the aorta in a cardiac cycle to study compliance, which is a measure of elasticity of an artery and defined as the ratio of volume change per pressure change between contraction and expansion of the aorta. The location and diameter of the aorta is roughly estimated by using a multiscale medial response function accompanied with a priori knowledge about the circular shape of the aorta as an initial segmentation step. Then, the estimate obtained is refined using an energy minimizing Geometrically Deformable Model (GDM). Their work introduces two new aspects the classical GDM. First, a Markov-Random Field (MRF) framework is introduced. The system uses Simulated Annealing (SA) and Iterated Conditions Modes (ICM) to minimize the energy of the snakes in the MRF framework. Second,

GDM is represented by a spline-based representation which is C2 continuous and has the advantage of computing the curvature from analytical models easily [34].

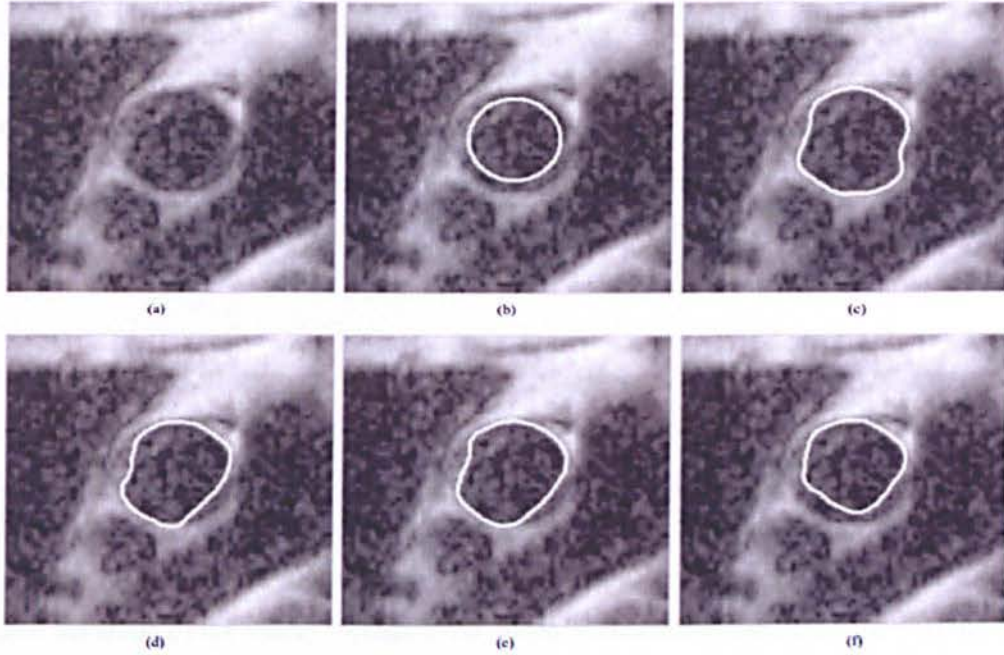


Figure 2.7: (a) Original image and the deformable model after (b) initialization, (c) SA optimization (1.83% error), (d) ICM optimization (21.98%), (e) greedy optimization (28.85%), and (f) gradient descent optimization (48.81%) [34].

L. Flórez Valencia *et al.* in 2007 developed an algorithm for lumen segmentation of arteries in MRA to facilitate the pre-operative choice of the stent's length and diameter. There were two models used to accomplish this task: a deformable cylindrical simplex (DCS) model of the arterial intraluminal wall and a right generalized cylinder (RGC) model representing the stent's geometrical properties. The angiographic 3D image is first segmented using the DCS model to create a patient-specific vascular model.

The RGC model of a folded stent is then slid along the vessel centreline until an interactively chosen delivery location, and the model's geometry is modified to simulate the unfolding of the stent. Lastly, the DCS model is re-meshed to fit the shape of the unfolded-stent model and thus to simulate the shape of the arterial lumen boundaries after stenting. Moreover, the cylinder deformation model is simple and requires a short computation time, which is compatible with actual clinical procedures [35].

2.2.2. TA CAD in CT

Bombardier *et al.* in 1997 used two fuzzy segmentation operators for the automatic identification of artery boundaries from angiogram images in their knowledge-based approach. Different segmentation operators cooperate to extract different anatomical structures (the aorta and renal arteries). The segmentation process has two main steps: (1) identification of the region of interest (ROI), which is the renal artery in this case; and (2) Detection of the boundaries of the identified structures automatically. They use fuzzy set theory to represent the knowledge [36].

In the same year Kitasaka *et al.* presented a model based segmentation of the aorta and pulmonary artery (PA) in the mediastinum of the chest from un-contrasted chest X-ray CT images. These areas are difficult to extract in CT due to them having low intensity contrast in the mediastinum. The authors' proposed method employed a model fitting technique to use shape features of blood vessels for extraction. First, edge voxels were detected based on the standard deviation of CT values. A likelihood image, which shows the degree of "likelihood" on medial axes of vessels, was calculated by applying the Euclidean distance transformation to non-edge voxels. Second, the medial axis of each vessel was obtained by fitting the model. This was done by referring the likelihood image. Finally, the aorta and PA areas were recovered from the medial axes by executing the reverse Euclidean distance transformation. The author applied the proposed method only to seven cases of uncontrasted chest X-ray CT images and evaluated the results by calculating the coincidence index computed from the extracted regions and the regions manually traced. Experimental results were promising as the extracted aorta and the PA areas coincided with manually input regions with the coincidence indexes values 90 % and 80-90 %, respectively, but the author does recognized that the proposed method should be applied in a larger number cases of CT for better evaluation[37].

Later in 2006 T. Kovacs *et al.* proposed the first step towards an automatic CAD system capable to display the different lumens in cases of acute aortic dissection. The author successfully detected the entire thoracic aorta lumen without any user interaction. The method uses HTs to detect the approximately circular shape of the aorta on the individual slices orthogonal to the vessel, and a 3D elastically deformable mass-spring model to more accurately adjust the

detected contour to the aortic lumen. It was a robust method against acquisition artifacts typically present in 3D CTA images of aortic dissections [38].

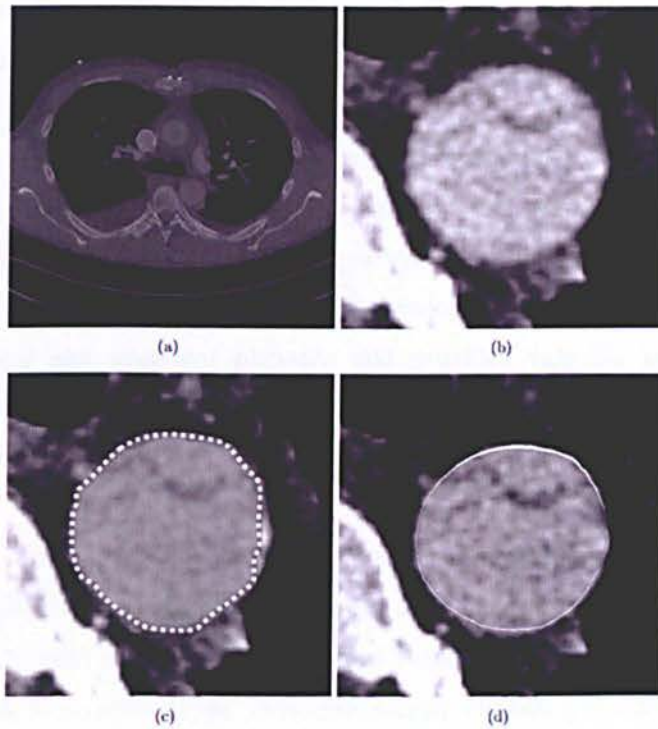


Figure 2.8: (a) The original axial slice, (b) the magnified axial slice with proper contrast and intensity in order to increase the accuracy of the manual segmentation, (c) the manually outlined aorta (dotted line) and (d) the correction of inaccuracies in the outline by repositioning some nodes in the 3D mesh (white line) [38].

Kurkure *et al.* In 2008 presented a method for localization and segmentation of ascending and descending aorta in non-contrast CT images using dynamic programming concepts to detect and quantify aortic calcium. The localization and segmentation of the aorta are formulated as optimal path detection problems, which are solved using dynamic programming principles. The method for segmentation of the ascending and descending aorta based on the Hough transform.

It was a dynamic programming-based method for the automated localization and segmentation of the thoracic aorta. Using the Hough space as a medialness feature space and applying dynamic programming for tracking provides an automatic and robust method to detect the centreline of symmetric and tubular structures like the aorta. It is shown that this step introduces a significant improvement in the localization of the aorta compared to the general approach of selecting the point of global maxima in the Hough space. The dynamic programming-based

aorta segmentation results compared well with manually traced aorta boundaries. However, the authors concluded that the segmentation of ascending aorta could be further improved by incorporating 3D surface continuity constraints and allowing more flexibility to deviate from circular shape assumption [39].

In 2009 Feuerstein *et al.* presented a method for the segmentation of the aortic arch and its main arterial branches in the thoracic CT scans. The method was based on Hough and Euclidean distance transforms and probability weighting, working on both contrast enhanced and non-contrast CT. The authors suggest the method developed can be useful in supporting the physician's diagnosis and treatment planning and provides valuable landmarks for further segmentation of the aortic branches, intra- and interpatient registration of the mediastinum, or chest atlas generation [40].

I. Isgum *et al.* In 2010 developed a computer-aided diagnosis system for fully automatic detection and quantification of calcifications in the aorta in computed tomography (CT) scans of the thorax, and subsequent risk assessment for cardiovascular disease. This technique was only successfully applied in sections of the aorta, specifically excluding the thoracic arch. A multi-atlas based segmentation method was performed to automatically delineate the aorta in scan [41].

This method had previously been developed by I. Isgum, *et al.* (2009), using an atlas-based segmentation approach based on the combination of multiple registrations. To identify candidate objects for calcifications, the segmented volume was thresholded at 130 HU. The candidate objects represented calcified lesions in the aorta and its vicinity, and noise.

To separate the calcifications in the aortic wall from the remaining candidate objects, each of them was described with 63 features. Subsequently, a two-stage classification with a selection of features and k-nearest neighbour (kNN) classifiers was performed. Based on the detected calcifications each subject was assigned one of six risk categories for coronary artery disease. The computer system detected 83.9% of calcifications at the expense of on average 1.9 false positive objects per scan. [42].

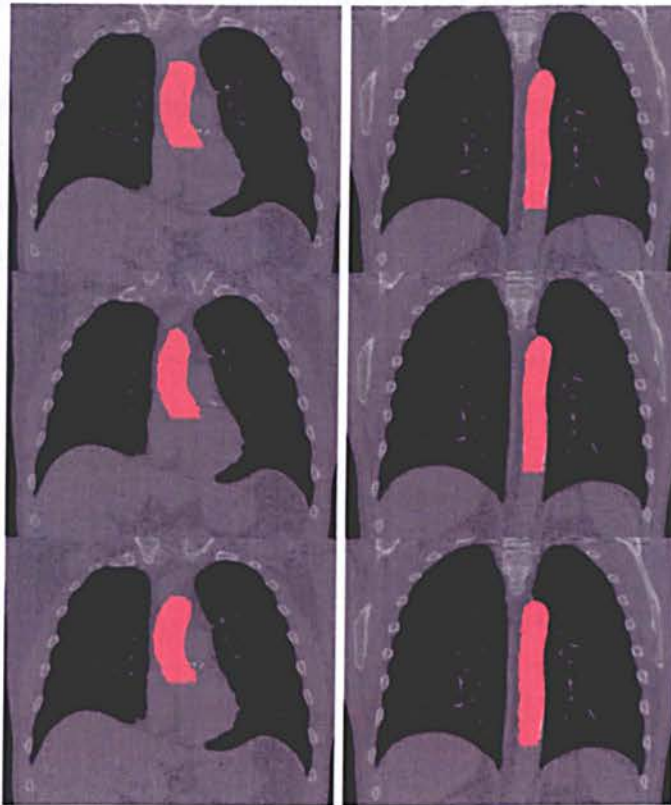


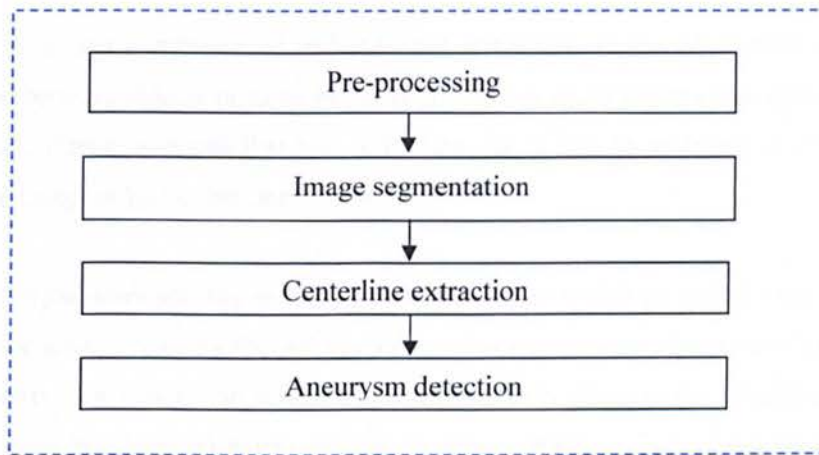
Figure 2.9: Results of the automated segmentation by I. Isgum, *et al.* (2009) [42].

Even though research has been done in MRI and CT, the best method for CAD system is CT as it clearly indicates the region of blood flow on the image due to contrast agent. Most of the detection methods are heavily dependent on the segmentation result of the artery, which is also a challenging task. Therefore there is a need to have a comprehensive CAD/CAM system to detect and segment an aneurysm in CTA images.

Until now considerable research has been conducted towards aorta detection and segmentation. However to the best of our knowledge there is no fully automated CAD system of thoracic aortic aneurysms in CT scans. Our research group has previously published a fully automated CAD system for detection of the abdominal aorta.

2.3. CAD Image Processing Components Literature Review

From reviewing the various available CAD systems in the previous section, we have come to notice that all CAD systems are application orientated and vary from one application to another, but always having some crucial steps of image processing methods as illustrated on the following diagram.



Vessel analysis in medical images is important both for diagnostic and intervention planning purposes. Vessel centreline extraction can be used to generate specific visualizations, such as endovascular views or multiplanar reformats.

Vessel segmentation can be used for quantification, for example quantification of an aneurysm, or to determine the dimension of stents to be used in interventions.

In many approaches for vessel analysis, images are first pre-processed to enhance vascular structures. Vessel enhancement improves vessel visualization (e.g. in volume rendering techniques or maximum intensity projections) and has the potential to facilitate the task of centreline extraction and segmentation.

Therefore, in the next sections we will review the different methods that can be used in each step to achieve the detection and quantification of the thoracic aorta in our case as described in the diagram above.

2.3.1. Pre-processing

The ideas of using variational methods in image processing can be traced back at least to Jain in 1977. However, the field did not attract much research interests until the concept of scale space was introduced in two independent works by J. Koednderink in 1984 and A. Witkin in 1983 [43, 44].

In this concept an image is represented and analyzed at multiple scales. Multiscale analysis is natural in vision because objects become larger if one moves close to the scene and smaller if one moves away. Hence, suppose that one is looking for a face in an image it can occupy either the whole image or just a tiny part of it [45].

This is different from other sensing such as tactile sensing in which an object's size obtained by a tactile sensor always remains the same since one has to touch the object in order to sense it or auditory sensing in which one specific temporal scale is given to the vibration of one's vocal cord. In these two seminal works multiscale representation of an image was obtained using Gaussian filtering at various scales, which was proven to be equivalent to deforming the image at various amount of time based on the classical heat equation, leading to an isotropic diffusion flow.

Later, in early 1990s, Perona and Malik proposed a nonlinear diffusion filter which later became one of the most influential works in the field. Unlike isotropic diffusion in which the information is diffused equally everywhere, nonlinear diffusion limits the diffusivity around some areas of interest like edges in order to preserve them. The work opened up a large number of studies on PDE-based image processing community, both theoretically and practically [46, 47, and 48].

Weickert proposed to further control the diffusivity not only at preferred locations but also at certain directions. The model is thus called anisotropic diffusion filter, which was shown to be very effective in enhancing coherent structures [49].

2.3.1.1. Diffusion Filtering

Diffusion filtering has become a powerful and well established tool in image processing. It is based on smoothing an image using the diffusion equation,

$$\frac{\partial I(x,t)}{\partial t} = \text{div}(D \cdot \nabla I) \quad (2.1)$$

Where $I(x,0) = I_0 : \mathbb{R}^2 \rightarrow \mathbb{R}$ is the input image, $x = (x,y)$ the spatial location, t an artificial time variable, ∇I the gradient of the image, and D the diffusion tensor, which is a positive definite symmetric matrix. Here, image intensity is considered as mass concentration and accordingly the intuition of diffusion is to balance concentration differences without creating or destroying mass. The process where a pixel gains less mass from its larger neighbours that it lost to its neighbours is called forward diffusion.

The reverse process is backward diffusion, where a pixel loses less mass to its smaller neighbour that it obtains from its larger neighbour. If D is replaced by a positive scalar valued diffusivity g , one has isotropic diffusion, where the information is diffused equally in all directions, as opposed to anisotropic in the general case, which is where diffusion in some directions is more emphasized than in others. The general isotropic diffusion equation is then,

$$\frac{\partial I(x,t)}{\partial t} = \text{div}(g \nabla I) \quad (2.2)$$

where g is any scalar valued function.

2.3.1.1.1. Linear diffusion

A simple case of isotropic diffusion is the case where the diffusivity g is constant over the whole image. In particular, when $g=1$, one obtains

$$\partial t = \Delta I = \text{div} (D . \nabla I) \quad (2.3)$$

where Δ denotes the Laplacian operator. The solution is given by

$$I(x,t) + (G_{\sqrt{2t}} * I)(x) \quad G_{\sigma}(x) = \frac{1}{2\pi\sigma^2} \exp\left(-\frac{x^2}{2\sigma^2}\right) \quad (2.4)$$

meaning that stopping the evolution process after a time $t \geq 0$ is equivalent to the convolution of the input image with a Gaussian kernel G_{σ} with the standard deviation $\sigma = \sqrt{2t}$ [50].

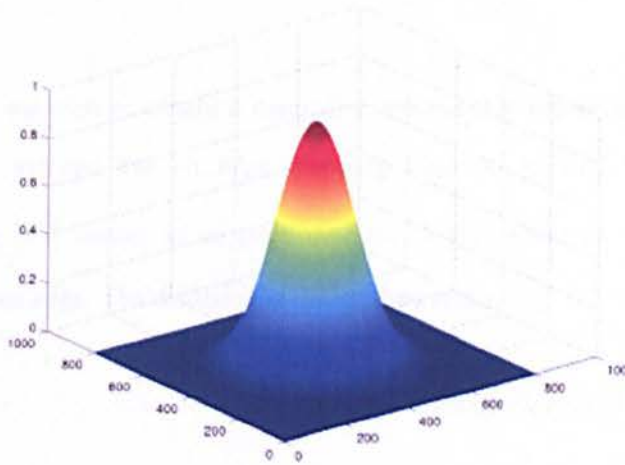


Figure 2.10: Example of a Gaussian filter kernel.

Larger values of t yield larger levels of smoothing, which defines a scale space for the image, which is a family of gradually smoother version of it. Note that any scale t_i can be obtained either for a sale $t_j(t_j < t_i)$ or from the original image. The scale space analysis provides a step to semantical description of an image from a pixel basis because it introduces a hierarchy of image features. This theory is more than twenty years old and detailed treatment of its various aspects can be found in previous research such as T. Lindbergh in 1994 and latter J Sporring *et al.* in 1997 [51, 52].

Gaussian filtering, as in equation 2.4, is regarded as a linear approach to reduce additive noise. An image gets progressively more and more simplified and noise removal is successful.

However, the method suffers from two major disadvantages. One is important features such as edges that are dislocated when moving from finer to coarser scales. To find the right location of structures at a coarse scale, one has to trace back to the original image, which is not an easy task to perform, especially when junctions and bifurcations are involved [54].

2.3.1.1.2. Isotropic non-linear diffusion

The best way to resolve both problems of linear diffusion is to introduce a location dependent diffusivity that limits or stops the diffusion in important areas, leading to a non-linear isotropic diffusion.

For example, if we wish to obtain a denoising process that preserves the edges contrast and location. Then, we can use an edge stopping function $g(|\nabla I|)$ satisfying $g(s) \rightarrow 0$ as $s \rightarrow +\infty$. Here, $|\nabla I|$ serves as an edge detector, higher value of it corresponds to higher likelihood to be an edge. The diffusion equation then reads,

$$\partial_t I = \text{div}(g(|\nabla I|)\nabla I) \quad (2.5)$$

Since the diffusivity g is a decreasing function which approached 0 in the vicinity of an edge, it reduced the smoothing amount around edges. The outcome of the filter depends considerably on choosing this function. The first formulation of this kind was introduced by Perona and Malik who proposed the two following diffusivity function,

$$g(|\nabla I|) = \frac{1}{1 + |\nabla I|^2 / \lambda^2} \quad (2.6)$$

$$g(|\nabla I|) = \exp\left(-\frac{|\nabla I|^2}{2\lambda^2}\right) \quad (2.7)$$

where $\lambda > 0$ is the contrast parameter. To study the behaviour of this parameter, we need to consider the 1D case for simplicity and denote $\phi(\partial_x I) = g(|\partial_x I|)\partial_x I$, leading to,

$$\partial_t I = \partial_x \phi(\partial_x I) = \phi'(\partial_x I) \Delta I \quad (2.8)$$

Two formulations of $\phi'(\partial_x I)$ corresponding to two diffusivity equations 2.6 and 2.7 can be derived as,

$$\phi'(\partial_x I) = \frac{\lambda^2(\lambda^2 - |\partial_x I|^2)}{(\lambda^2 + |\partial_x I|^2)^2} \quad (2.9)$$

$$\phi'(\partial_x I) = \left(1 - |\partial_x I|^2 / \lambda^2\right) \exp\left(-\frac{|\partial_x I|^2}{2\lambda^2}\right) \quad (2.10)$$

In both cases, $\phi'(\partial_x I) > 0$ (forward diffusion) if $|\partial_x I| < \lambda$ and vice versa, $\phi'(\partial_x I) < 0$ (backward diffusion) if $|\partial_x I| > \lambda$. Forward diffusion smoothes the contrast and backward diffusions enhance them. Therefore contrast parameter λ determines how large the gradient of an edge must be in order for the edge to be preserved.

It is not trivial to study the stability of the above model. Of course, a reasonable regularization provided by numerical schemes can stabilize the process. However, to reduce the dependence of stabilization on numerical implementations, one can apply spatial regularization directly on the continuous equation. Catte *et al.* proposed to replace the diffusivity $g(|\nabla I|)$ of the Perona Malik model by $g(|\nabla I_\sigma|)$ where, resulting in,

$$\partial_t I = \text{div} (g(|\nabla I_\sigma|) \nabla I) \quad (2.11)$$

In 1994 X. Li *et al.* research, the parameter σ and λ were made time dependent. The spatial regularization with additional scale parameter σ helps the Perona Malik model eliminate false edges caused by noise [54].

2.3.1.1.3. Anisotropic diffusion

All diffusion schemes discussed so far, either linear or not, rely on a scalar valued diffusivity and thus are isotropic, where the diffusion amount is the same in all direction. In some

applications where edges are noisy, it is desirable to reduce the diffusion across edges only while maintaining the smoothing along edges. These requirements can be satisfied by replacing the scalar valued diffusivity with a matrix valued diffusion tensor D which is constructed by defining its orthogonal eigenvectors and eigenvalues.

The main idea is to align the eigenvectors to the directions along which the contrast is smoothed and assigning the smoothing amount to the corresponding eigenvalues. If we for example construct the eigenvectors v_1, v_2 of D such that $v_1 \parallel \nabla I_\sigma$ and $v_2 \perp \nabla I_\sigma$ and choose the corresponding eigenvalues λ_1 and λ_2 as,

$$\lambda_1 = g(|\nabla I_\sigma|) \quad (2.12)$$

$$\lambda_2 = 1 \quad (2.13)$$

The diffusion tensor is then calculated as $D = Q \text{diag}(\lambda_i) Q^T$ where Q is a matrix comprised of the normalized v_1 and v_2 as its columns. The resulting filter will limit the diffusion in v_1 direction, across the edges, while allow constant smoothing in the v_2 direction, along the edges.

2.3.2. Image Segmentation

Image segmentation algorithms for the delineation of anatomical structures and other regions of interest are becoming increasingly important in the support and automation of a number of radiological tasks. Amongst the key applications of these algorithms in biomedical imaging, are the quantification of tissue volumes, the diagnosis and localization of pathology, the study of anatomical structures, the treatment planning, and computer-guided surgery [55].

By definition, image segmentation refers to the partitioning of an image into a set of non-overlapping regions whose union is the entire image. In the simplest case, there exists a single object region and a single background region [56].

A region cannot be declared a segment unless it is completely surrounded by edge pixels. For this reason, and from a computational point of view, it is often complex to characterise and

identify well-done segmentation. A set of rules in general segmentation procedures are thus used. Regions of image segmentation should be uniform and homogeneous with respect to some particular characteristic of the image (e.g. the grey level or texture) region interiors should be simple and without many holes, adjacent regions of segmentation should have significantly varying values with respect to the characteristic on which they are uniform, and the boundaries of each segment should be simple, not ragged, and spatially accurate [56].

The segmentation of an image produces a binary output region. Object pixels are set to 1 (white) and background pixels are set to 0 (black). Depending on the particulars of an application, the target region may alternatively be labelled as 0 and the background as 1. With the standard pixel-based methods available, only the grey value of a pixel is used as to decide whether or not a pixel belongs to a target object [56].

In our research it was difficult to determine which segmentation method would be more suitable to detecting the thoracic aorta and aneurysms, due to similarity of intensity value of the aorta and the tissue surrounding it. Therefore in this section we review the different segmentation methods.

2.3.2.1. Thresholding

Thresholding is one of the simplest techniques and was earlier the basis of manual or semi-automatic segmentations. In this approach, voxels with an intensity value below or above a defined threshold are regarded as part of the object whereas remaining voxels are interpreted as background. To convert a grey level image into a binary image, all pixels below a predetermined threshold are turned to zero and all pixels above that threshold are turned to one.

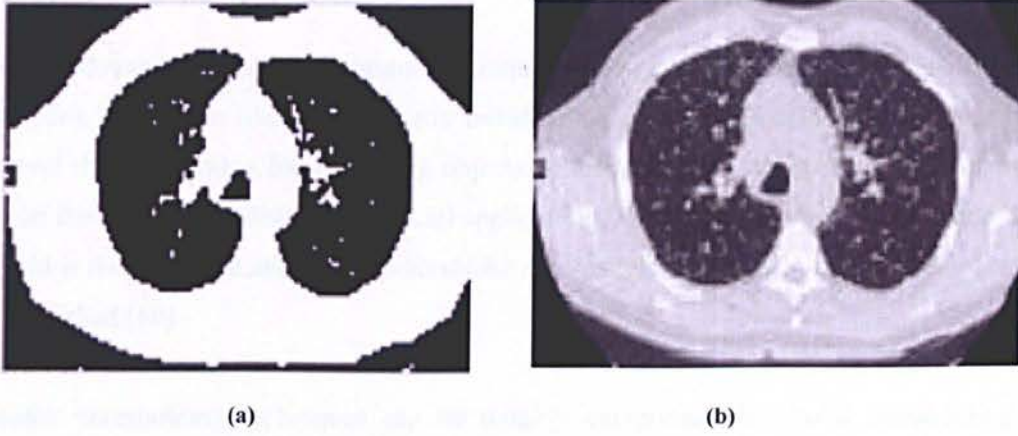


Figure 2.11: Thresholding (a) original image (b) threshold image.

It is still one of the most commonly used methods of image segmentation. Apart from its use as a standalone segmentation method, thresholding may yield a good initial estimate from which more advanced methods can proceed [56].

If $g(x, y)$ is a thresholded version of $f(x, y)$ at some global threshold T ,

$$g(x, y) = \begin{cases} 1 & \text{if } f(x, y) \geq T \\ 0 & \text{otherwise} \end{cases} \quad (2.14)$$

Ney *et al.* introduced an editing tool for 3D medical imaging based on simple thresholding [42]. Suri *et al.* defined a threshold value to extract the vessel structure from MRA dataset [57]. Shifiman *et al.* used multilevel thresholding calculated by a neural network in order to segment aortic aneurysm from CTA images.

One serious shortcoming of these approaches is the usage of global thresholding, which performs poorly if the vessel intensity varies significantly throughout the image [57].

Although Fiebich *et al.* refined the technique by combining the threshold value with local gradient information the concept still has limitations such as merging different tissues with similar intensity [57].

2.3.2.1.1. Automatic Thresholding

Automatic thresholding is an important technique in image segmentation and machine vision applications. The basic idea of automatic thresholding is to automatically select an optimal gray-level threshold value for separating objects of interest in an image from the background based on their gray-level distribution. In all applications of thresholding, correct selection of the threshold is the key issue and many methods for automatic selection of optimal thresholds have been published [60].

Automatic thresholding techniques can be roughly categorized into local thresholding and global thresholding.

Local Thresholding

Local thresholding methods can deal with non-uniform illumination but they are complicated and slow. For automated visual inspection applications, where non-uniform illumination is usually not an issue due to controlled lighting conditions, global thresholding is commonly used for its simplicity and speed [60].

Global Thresholding

Global thresholding selects a single threshold value from the histogram of the entire image. Local thresholding uses localized gray-level information to choose multiple threshold values; each is optimized for a small region in the image. Global thresholding is simpler and easier to implement but its result relies on good (uniform) illumination.

Among the global thresholding techniques, Otsu method (Otsu, 1979) is one of the better threshold selection methods for general real world images with respect to uniformity and shape measures. This method selects threshold values that maximize the between-class variances of the histogram. The Otsu method is optimal for thresholding large objects from the background; in other words, it is good for thresholding a histogram with bimodal or multimodal distribution. The Otsu method, however, fails if the histogram is unimodal or close to unimodal. Because

defect detection applications range from no defect to small and large defects, the gray-level distributions range from unimodal to bimodal [61].

As a result, to successfully detect defects in the automatic visual inspection applications with the Otsu method, we need to revise the method so that it will handle both unimodal and bimodal distributions equally well. The objectives of this study were to revise the Otsu method for selecting optimal threshold values for both unimodal and bimodal distributions, and to test the performance of the revised method on common defect detection applications.

In 1985 Kittler *et al.* introduced an automatic threshold selection algorithm for segmentation of object-background images dubbed Robust Automatic Threshold Selection (RATS). The RATS algorithm computes thresholds either locally or globally using a weighted average of the grey levels within arbitrary areas of an image. The weight assigned to each pixel is the response of a simple edge detector at that pixel [62].

RATS PRINCIPLE

If you consider an ideal step $S_A(x)$ at $x=0$ of amplitude A on a constant background B , this function can be split into an even and odd part,

$$S_A(x) = B + \frac{A}{2} + \frac{A}{2} \text{sgn}(x) \quad (2.15)$$

With $\text{sgn}(x)$ the sign of x . Let $S_A(x)$ be convolved with an even point-spread-function (PSF) $\text{psf}(x)$ with a unity integral over $(-\infty, \infty)$. The result $S_{A,\text{psf}}(x)$ can be written as an even and odd part,

$$S_{A,\text{psf}}(x) = B + \frac{A}{2} + \frac{A}{2} (\text{psf} * \text{sgn})(x) \quad (2.16)$$

In which $(\text{psf} * \text{sgn})(x)$ denotes the convolution of $\text{psf}(x)$ and $\text{sgn}(x)$. Let a weight function $w(x)$ be an even, integrable function, which is zero outside $[-a, a]$ for some finite a , and which has a nonzero integral over $[-a, a]$, it then follows that

$$T = \frac{\int_{-a}^a w(x) S_{A,psf}(x) dx}{\int_{-a}^a w(x) dx} = \frac{\frac{A}{2} \int_{-a}^a w(x) (psf * sgn)(x) dx + (B + \frac{A}{2}) \int_{-a}^a w(x) dx}{\int_{-a}^a w(x) dx} = B + \frac{A}{2} \quad (2.17)$$

since the first term of the numerator is the integral of an odd functions over an even interval, and therefore zero. In the case of a point-spread-function (PSF), where the maximum of the first derivative is halfway between object and background intensity, the statistics T is therefore, equal to the ideal threshold.

Despite the successful application of RATS in 2-D microscopic images by M. Wilson *et al.* in 1996, it had never been adapted to 3-D medical images. In 2003 the author published his new work where he develops two new moving-window versions of the algorithm, using either flat or Gaussian weighted windows for local thresholding with Robust Automatic Threshold Selection and applied them to segmentation of blood vessels in 3-D angiograms.

The author concluded that fast segmentation of blood vessels against a varying background and noise is possible at modest computational cost [63].

Thresholding CT images is a simple way to separate in our case the thoracic aorta from other soft tissues. Some of the drawbacks of this technique however, are the merging together of nearby bones and the creation of holes in the data where the bone is thin or very spongy.

In section 2.3.2.2 we review another segmentation technique for detection of TA, region growing algorithm that will provide us with an improvement in the segmentation of TA from CT scans.

2.3.2.2. Region Growing

Some segmentation methods such as Thresholding achieve their goal by looking for the boundaries between regions based on discontinuities in gray levels or colour properties. Region-based segmentation is a technique for determining the region directly.

In the case of region-growing segmentation, a homogeneity criterion forms the basis of examining neighbouring pixels and adding them to a particular region. This process is iterated for each pixel in the image. When there are adjacent regions a region merging algorithm is operated, in which similar regions are merged and weak edges are dissolved while strong edges are allowed to remain intact [64].

The first step in region growing is to select a set of seed points. Seed point selection is based on some user criterion (for example, pixels in a certain gray-level range, pixels evenly spaced on a grid, etc.). The initial region begins as the exact location of these seeds. The algorithm starts executing by first considering all the neighbouring pixels to the seed point and then joining those pixels that have similar characteristics to the region. The remaining pixels surrounding the region, which also have similar characteristics, are included as well. The process continues to iterate until all pixels have been considered for inclusion [64].

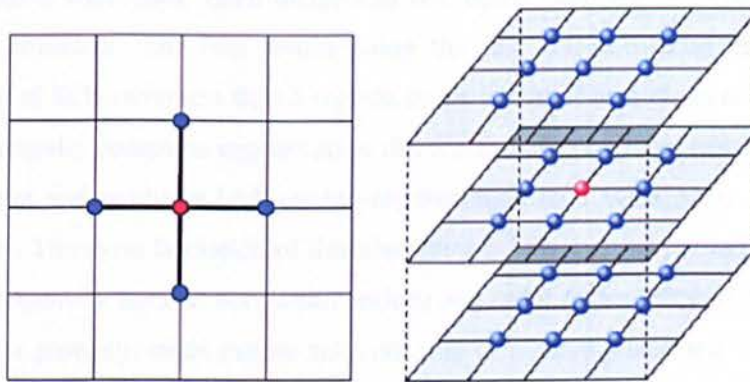


Figure 2.12: On the left a four-neighbour stencil in 2D. On the right a 26-neighbor stencil in 3D. In both illustrations the reference grid point is shown in red and its neighbours in blue.

The foundation of the method is the grouping of pixels of the same or similar brightness or colour into regions according to the given membership criteria. This membership criterion is derived from a threshold value. At times this can arise to be less than optimal, since there is a need for modifications according to particular applications, and even when the intensity or contrast of the image is changed. Further, the thresholds are always dependent upon the image intensity and imaging conditions. Results are also sensitive to the noise in the image [64].

The region-growing methods discussed below are amongst the most commonly encountered and a variety of algorithms have been proposed for their computational implementation.

Chang and Li in 1994 proposed a region growing structure for image segmentation. This process is guided by regional feature analysis and no parameter or a prior knowledge about the image is required. The algorithm developed in this study is known as Fast Adaptive Segmentation (FAS) algorithm. The image is first divided into many small primitive regions that are assumed to be homogeneous. These primitive regions are then merged to form larger regions until no more merges are possible. Two regions are merged if they pass the homogeneity test and also if the value of the edge connecting them is weak [65].

The focus of this study was on investigating how different merge criteria affect the quality of segmentation and the processing time. The experiments designed to evaluate the merge criteria were based on four important aspects of segmentation output: region merge ability, boundary accuracy, merge rejections, and number of iterations required. In these experiments, 300 images of size 50x50 pixels were used. Each image had two equal sized regions that share a simple straight 50-unit boundary. The best results using the fast merge method gives the correct classification rate of 86% (with less than 5 regions in the image). The authors concluded that the algorithm automatically computes segmentation thresholds based on local feature analysis. The algorithm is robust and produces high quality segmentation on a wide range of textured and grey scale images. The main limitation of this algorithm is however the limited applicability of the adaptive homogeneity tests on very small regions and order dependency of its segmentation results. For region growing, seeds can be automatically or manually selected. Their automated selection can be based on finding pixels that are of interest (e.g. the brightest pixel in an infra-red image can serve as a seed pixel). Seeds can also be selected manually for every object present in the image [65].

Also in 1994, Adams and Bischof studied the efficiency of seeded region growing approach for image segmentation of greyscale images, where the seeds are manually selected. The method is used to segment an image into different regions by making use of a set of seeds. Each seeded region is a connected component containing one or more points and is represented by a set S . The set of immediate neighbours bordering the pixel is then calculated. The neighbours are then examined and if they intersect any region from set S , then a measure d (difference between a pixel and the intersected region) is computed. If the neighbours intersect on more than one region, then the set is taken as that region for which difference measure d is maximum. The new

state of regions for the set then constitutes input to the next iteration. This process continues until the entire image pixels have been assimilated into regions. Hence, for each iteration the pixel that is most similar to a region that it borders is appended to that region [66].

The SRG algorithm is inherently dependent on the order of processing image pixels. One implication of this algorithm is that raster order processing and anti-raster order processing do not lead to the same tessellation. The algorithm was applied on images with different types of objects in them. The authors concluded that the method has the advantage that it is fairly robust, quick, and parameter free except for its dependency on the order of pixel processing [66].

In some studies, edge or gradient information has been used in combination with region growing for image segmentation. J. P. Gambotto proposed in 1993 an algorithm that combines the region growing and edge detection methods for segmenting the images. The method is iterative and sees both of these approaches in parallel. The algorithm starts with an initial set of seeds located inside the true boundary of the region. The pixels that are adjacent to the region are iteratively edged with it if they satisfy a similarity criterion. A second criterion uses the average gradient over the region boundary to stop the growth. The last stage refines the segmentation. The analysis is based on cooperation between the region growing algorithm and the contour detection algorithm. Since, the growing process is performed by adding segments to a region, some pixels which belong to the next region and to the previous region may be misclassified. To locally reclassify these pixels a nearest neighbour rule is then applied [67].

The algorithm was tested on a series of X-ray images. The authors concluded that the method uses both the statistical model of the region and the average gradient computed over its boundary. The system proved to behave in a similar way the snake class of algorithms but this can also be used for the segmentation of closed regions with unknown or complex shapes [67].

In 1995, Hojjatoleslami and Kittler proposed a new region growing approach for image segmentation which uses a measure of contrast information to specify the boundary of a region. The method has the capability of finding the boundary of a relatively bright/dark region in a textured background. The method relies on a measure of contrast of the region that represents the variation of the region grey-level as a function of its evolving boundary during segmentation. This helps to identify the best external boundary of the region [68].

The application of a reverse test using a measure of contrast then yields the region with high gradient boundary as the output. The unique feature of the approach is that in each step at most one candidate pixel will exhibit the required properties to join the region. The growing process is directional so that the pixels join the grown region according to a ranking list and the discontinuity measurements are tested pixel by pixel.

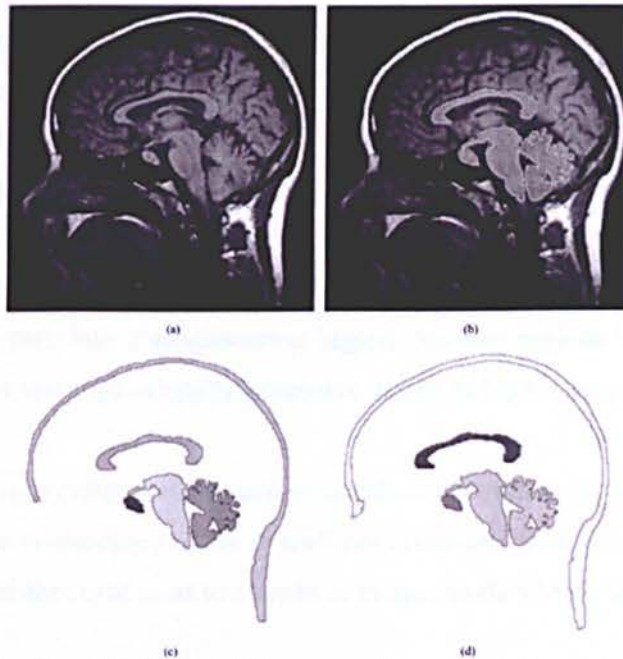


Figure 2.13: (a) Original head MR image. (b) Segmentation result of five regions superimposed on the original image (c), (d) peripheral contrast and average contrast regions and boundaries segmented out from image (a) [68].

The authors have performed a number of experiments on synthetic and real images. The authors concluded that the results are more reliable and consistent than conventional threshold methods. The algorithm is also insensitive to a reasonable amount of noise. The main advantage of the algorithm is that no knowledge is needed about the regions [68].

Later in 200, Singh and Al-Mansoori compared region growing and gradient based techniques for detecting regions of interest in digital mammograms. These regions of interest form the basis of applying shape and texture techniques for detecting cancerous masses. The study also proposes a two stage method where gradient based techniques are applied followed by region growing method which yields less number of regions for analysis. First, histogram equalization and fuzzy enhancement techniques improve the quality of image. Their utility is then compared

using three quantitative measures. After the enhancement step, the images are then subjected to region growing or gradient operations (masking) for segmentation purpose. The segmented image is then analysed for estimating the regions of interest and the results are compared against a previously known diagnosis of the radiologist. The authors concluded that the region growing segmentation gives a smaller number of regions for the analysis as compared to gradient based methods without disregarding quality [69].

Single linkage region growing method is another, commonly used, region algorithms. The method considers each pixel as a node in a graph. Any neighbouring pixels that have characteristics which are similar enough to the pixel (region) are merged. The image segments are maximal sets of pixels, all belonging to the same connected component [70].

This algorithm is by far simpler in design but it does have a problem with leakage: should one pixel from a region leak into a neighbouring region, the two regions would merge. Another disadvantage is that it is computationally expensive due to its highly iterative nature [70].

In its basic form, the algorithm used for conventional seeded region-growing has two important facets, which are the foundations of its overall performance: the manner in which seeds are selected, and the algorithm used to as to include or merge pixels into a single region.

An advantage to this technique is that similar pixels are spatially linked prior to any processing having been performed, with the effect of encouraging the connectivity of segmented regions. For that reason in the next section we review level set methods that would correct such problems that region growing has.

2.3.2.3. Level Set Methods

A level set of a real value function ϕ of n variables is a set of the form:

$$\{(x_1, \dots, x_n) | \phi(x_1, \dots, x_n) = c\} \quad (2.18)$$

where c is constant and x_i are the n variables. Therefore, a level set is the set of points where the function ϕ takes on a given constant c .

The concept of level sets was first introduced by Osher and Sethian . This method was initially designed for tracking the motion of a front whose speed depends on the local curvature. The evolution of the function ϕ is linked to the propagation of the interface through a time dependent level set equation. Using the implicit representation $\phi(x)$, where x is the position vector, a convection equation can be solved to propagate level sets transported by a velocity field v [71].

$$\phi_t + v \nabla \phi = 0 \quad (2.19)$$

In many cases, we are interested only in the motion normal to the boundary; hence the velocity v can be represented using the scalar function F and the normal direction n .

$$v = Fn = F \frac{\nabla \phi}{|\nabla \phi|} \quad (2.20)$$

The hyperbolic, Hamilton Jacobi equation, obtained from equations 2.19 and 2.20, is given by

$$\phi_t + F |\nabla \phi| = 0 \quad (2.21)$$

Integrating the level set equation is an initial value problem which tracks the evolution of the level sets $\phi = \text{constant}$ assuming F is given by the specifics of the evolution of the ϕ for a particular problem.

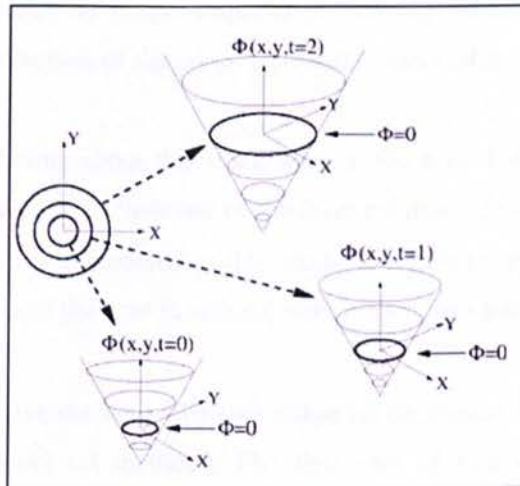


Figure 2.14: Illustration of the transformation of front motion into the level set [71].

The following first order up winded finite difference approximation can be used to integrate this equation 2.21, two dimensional in space.

$$\phi_{i,j}^{n+1} = \phi_{i,j}^n - \Delta t \left[\max(F,0) \nabla_{i,j}^+ + \min(F,0) \nabla_{i,j}^- \right] \quad (2.22)$$

where

$$\nabla_{i,j}^+ = \left[\max(D^{-x} \phi_{i,j}^n, 0)^2 + \min(D^{+x} \phi_{i,j}^n, 0)^2 + \max(D^{-y} \phi_{i,j}^n, 0)^2 + \min(D^{+y} \phi_{i,j}^n, 0)^2 \right]^{1/2}$$

$$\nabla_{i,j}^- = \left[\max(D^{-x} \phi_{i,j}^n, 0)^2 + \min(D^{+x} \phi_{i,j}^n, 0)^2 + \max(D^{-y} \phi_{i,j}^n, 0)^2 + \min(D^{+y} \phi_{i,j}^n, 0)^2 \right]^{1/2}$$

Here, D^{-x} is the first order backward difference operator in the x-direction, D^{+x} is the first order forward difference operator in the x-direction. Mathematically these operators are given by:

$$D^{-x} \phi_{i,j} = \frac{\phi_{i,j} - \phi_{i-1,j}}{\Delta x} \quad (2.23)$$

$$D^{+x} \phi_{i,j} = \frac{\phi_{i+1,j} - \phi_{i,j}}{\Delta x}$$

One of the most attractive features of the level set method is its ability to track the motion through topological changes. More specifically, an a priori assumption about the connectedness of the shapes of interest was no longer required. Following Santosa's work, Litman *et al.* in 1988 explored the reconstruction of the cross-sectional contour of a cylindrical target [72].

Two key distinguishing points about this work were in the way that the authors dealt with the deformation of the contour, and in their use of the level set method to represent the contour. The shape deformation method implemented in this work was enabled by a velocity term, and lead to a closed-form derivative of the cost functional with respect to a perturbation of the geometry.

Later in 200 Dom *et al.* introduced a two-step shape reconstruction method that was based on the adjointed field and level set methods. The first step of this algorithm was used as an initialization step for the second step and was mainly designed to deal with the non-linearity's present in the model. The second step of this algorithm used a combination of the level set and the adjointed field methods. Although inspired by the works of A. Littman *et al.*, S. Osher *et al.* and F.Santosa *et al.*, the level set method used by Dorn *et al.* was not based on a Hamilton-

Jacobi type equation. Instead, an optimization approach was employed, and an inversion routine was applied for solving the optimization [71, 72, 73, and 74].

The level set ideas in inverse problems were further developed to tackle more advanced problems such as having shapes with textures or multiple possible phases. Moreover, regarding the evolution of the level set function where usually gradient descent methods are the main minimization schemes applied, some authors such as Burger and Soleimani proposed using second order convergent methods such as the Newton and quasi-Newton methods [75, 76].

While level set methods provide large degrees of flexibility in shape representation, there are numerical concerns associated with these methods. Gradient descent methods used in these problems usually require a long evolution process.

Even though this problem may be overcome using second order methods, the performance of these methods for large problems such as 3D shape reconstructions remains limited and usually gradient descent type methods are the only option for such problems. Moreover re-initialization of the level set function to keep it well behaved and velocity field extensions to globally update the level set function through the evolution are usually inevitable and add extra computational costs and complexity to the problem [77].

In all traditional level set methods already stated, the unknown level set function belongs to an infinite dimensional function space. From an implementation perspective, this requires the discretization of the level set function onto a dense collection of nodes.

An alternative to this approach is to consider a finite dimensional function space or a parametric form for the level set function such as the space spanned by a set of basic functions.

Initially in 2004, Kilmer *et al.* proposed using a polynomial basis for this purpose in diffuse optical tomography applications. In this approach, the level set function is expressed in terms of a fixed order polynomial and evolved through updating the polynomial coefficients at every iteration [78].

One of the main contributions in this regard is the work by Wang *et al.* Here the level set function is spanned by multiquadric radial basis functions as a typical basis set in scattered data fitting and interpolation applications. Authors showed that through this representation, the Hamilton-Jacobi partial differential equation 2.24 changes into a system of ordinary equations and the updates for the expansion coefficient may be obtained by numerically solving an interpolation problem at every iteration [79].

$$F(x, u(x), Du(x), \dots, D^{k-1}u(x), D^k u(x)) = 0 \quad (2.24)$$

Where $u : \Omega \rightarrow \mathbb{R}$ and Ω is any open subset in \mathbb{R}^n . It often takes $\Omega = \mathbb{R}^n$. Here the notation $D^k u(x)$ denotes the vector containing all k th order partial derivatives. For example,

$$Du(x) = \left(\frac{\partial u}{\partial x_1}, \dots, \frac{\partial u}{\partial x_n} \right)^T \quad (2.25)$$

and

$$D^2 u(x) = \left(\frac{\partial^2 u}{\partial x_i \partial x_j} \right)^T \quad 1 \leq i, j \leq n \quad (2.26)$$

and so on.

Gelas *et al.* used a similar approach as the one by Wang *et al.* for image segmentation. As the basis set they used compactly supported radial basis functions, which not only reduce the dimensionality of the problem due to the parametric representation, but also reduce the computation cost through the sparsely that this class of functions provide. As advantages of the method they showed that appropriate constraints of the underlying parameters can avoid implementation of the usual re-initialization [79, 80].

Also the smoothness of the solution is guaranteed through the intrinsic smoothness of the underlying basis functions, and in practice no further geometric constraints need to be added to the cost function. As an alternative to this approach, Bernard *et al.* parameterized the level set function in terms of B-splines as in equation 10 below where $\beta^n(\cdot)$ is the uniform symmetric d -dimensional B-spline of degree n . One of the main advantages of their method was representing the cost function minimization directly in terms of the B-spline coefficients and avoiding the evolution through the Hamilton-Jacobi equation [81].

$$\phi(x) = \sum_{k \in z^d} c[k] \beta^n \left(\frac{x}{h} - k \right) \quad (2.27)$$

Due to a vessel curved shape anatomy, there is a difficulty in measuring true diameters of the vessel. There have been several methods previously proposed that use level set techniques to do so. But even though these methods are effective at finding the vessel boundary they suffer from a high computational complexity due to the level set approaches, particularly when working with 3D datasets such as DICOM images.

In section 2.3.2.4, we discuss a segmentation technique, ellipse fitting that is very suitable to use in the case of segmenting thoracic aorta aneurysm, as the aorta assumes an elliptical shape in the orthogonal plane to centre line in the CTA DICOM images.

2.3.2.4. Finding ellipses

There are five unknown parameters for a randomly selected ellipse, (x_0, y_0) for the centre, α for the orientation, (a, b) for the major and minor axes. Usually it is required to have a set of 5 edge pixels to calculate all parameters. If additional information is used at each edge pixel or choose special pixels, fewer pixels are required for determining an ellipse position [82].

For each pair of pixels (x_1, y_1) and (x_2, y_2) , it's assumed there are two vertices on the major axis of an ellipse. It can also be assumed that there are two vertices on the minor axis of an ellipse, but this will increase the computational time because it needs to check pixels in a larger range of the image. Then it is possible to calculate four parameters for the assumed ellipse as follows:

$$x_0 = (x_1 + x_2) / 2 \quad (2.28)$$

$$y_0 = (y_1 + y_2) / 2 \quad (2.29)$$

$$a = \left[(x_2 - x_1)^2 + (y_2 - y_1)^2 \right]^{1/2} / 2 \quad (2.30)$$

$$\alpha = a \tan \left[(y_2 - y_1) / (x_2 - x_1) \right] \quad (2.31)$$

Where (x_0, y_0) is the centre of the assumed ellipse, a the half-length of the major axis and α the orientation of the ellipse.

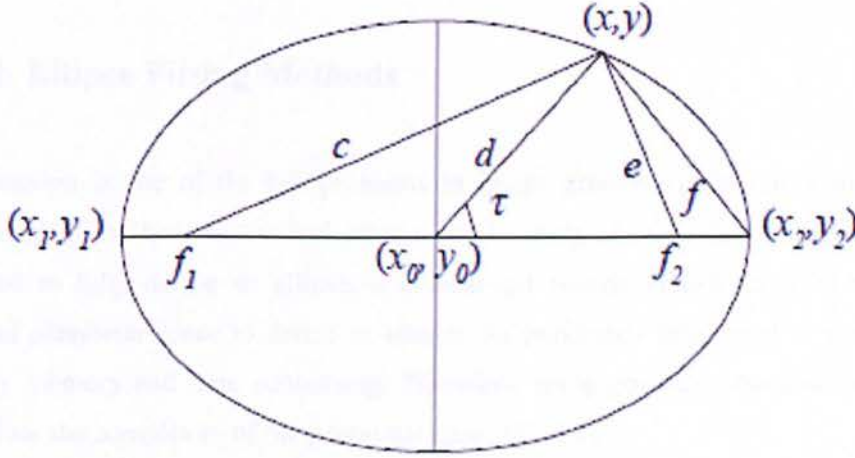


Figure 2.15: Ellipse geometry.

Figure 2.6 shows ellipse geometry. f_1 and f_2 are foci of the ellipse and (x, y) is the third point used to calculate the fifth parameter. The distance between (x, y) and (x_0, y_0) should be less than the distance between (x_1, y_1) and (x_0, y_0) or between (x_2, y_2) and (x_0, y_0) . So the half-length of the minor axis can be estimated by the following equation

$$b^2 = \frac{(a^2 d^2 \sin^2 \tau)}{(a^2 - d^2 \cos^2 \tau)} \quad (2.32)$$

Where $\cos \tau$ is

$$\cos \tau = \frac{(a^2 + d^2 - f^2)}{2ad} \quad (2.33)$$

and d is the distance between (x, y) and (x_0, y_0) .

It is therefore, possible to calculate all parameter of an ellipse by simply using equations 2.28-2.33. As it is only necessary to vote on the half-length of the minor axis, it is best to use a one-dimensional accumulator array. If the votes reach a threshold, an ellipse is found and we output the parameters for this detected ellipse and remove all pixels on this ellipse from the image.

After this pair of pixels is checked, accumulator array is cleared and it proceeds to the next pair [82].

2.3.2.4.1. Ellipse Fitting Methods

Ellipse detection is one of the key problems in image processing. Its importance is widely recognized and it has been researched using a good variety of methods. Since five parameters are required to fully define an ellipse, a generalized Hough Transform (HT) needs a five dimensional parameter space to detect an ellipse. As previously mentioned in section 2.3.2.4, that is very memory and time consuming. Therefore, some geometric constraints need to be used to reduce the complexity of the parameter space [83, 84].

In 1994, Yin and Chen introduced a new approach that is based on the geometrical property. The edge points in an input image were classified into several subimages. Ellipses with different symmetric axes lie in different subimages. In each subimage, symmetry was applied again to obtain those sets of five points that possibly lie on the same ellipse [85].

Later in 1995 Ho and Chen's constituted two midpoint arrays by considering pairs of edge points in the same horizontal and vertical positions. From these two arrays the straight lines are detected separately by the HT and their intersections provide possible centres for ellipses. Then, three other parameters of the angle and their major and minor axes remain to be estimated [86].

Aguado *et al.* in 1996 proposed a method that a mapping for ellipse extraction had been developed, which includes edge tangent information. In order to decompose the space required for the HT and retain the original advantages of the HT, they combined this mapping with local information computed from pair of edge points. Since edge direction information was included, the proposed method only involved pairs of points without any geometric constraints [87].

Lei and Wong proposed an approach to detect ellipses from symmetric contours in a picture efficiently. The idea is based on the detection of the symmetric axes from contours in a Hough-based approach, so as to transform a high-dimensional problem into two two-dimensional ones.

From this idea, they found symmetric axes from contours first and then find ellipse from the contours [88].

In order to overcome the excessive time and space requirements for ellipse extraction, most of previous techniques decompose the five-dimensional parameter space into several sub spaces of fewer dimensions. The decomposition is achieved by using geometric features that define constraints in the organization of edge data.

These constraints include distance and angular relationships that define relative positions between a set of edge points. Hence, the parameters are computed after labelling the points that satisfy the constraints in a computational intensive approach.

2.3.3. Finding Centreline Paths

Skeleton is useful shape interpretation for a 3D object, which has been found in many applications in medical visualization. More specifically, in our research for purposes of quantification of features such as those presented in the thoracic aorta.

The definition of skeleton of 3D object varies in image processing applications. In virtual navigation application the following characteristics must be possessed by resulted skeleton: centeredness, connectivity, smoothness and topology preserving.

There are three main catalogues of skeleton extraction methods, namely:

- *Thinning algorithm* to iteratively peel off the boundary/surface of the 3D object. Skeletonization algorithm based on thinning preserve the topology of 3D object, but is computationally expensive.
- *Voronoi method* based on triangular voronoi diagram. This method can guarantee the preservation of both topology and connectivity, but it is error prone to boundary noise and requires considerable post-pruning process.

- *Distant transform* to directly extract skeletal points by testing the points' local neighbourhood based on a distance map, which is an approximation of the Euclidean distance.

2.3.3.1. Hessian matrix

A first class of methods attempts to find centrelines of tubular structures as they are manifest directly in intensity images. These methods do not assume that the surfaces of such structures have first been extracted. Three representative approaches in this category are those of Aylward and Bullit, Deschamps and Cohen and Wink *et al.* [89, 90, and 91].

Aylward and Bullot present a centreline tracking approach which is based on a characterization of intensity ridges in 2D and 3D images. Centrelines of tubular structures are identified using properties of the Hessian matrix. They pay particular attention to the validation of their method, both quantitative and qualitative, demonstrating its robustness under parameter changes, changes in scale and simulated image acquisition noise. The method is an iterative one, where the centreline is continuously extended in the estimated direction of its local orientation [89].

Deschamps and Cohen relate the problem of finding centreline paths to that of finding paths of least action in 3D intensity images. This leads to a form of the well known eikonal equation where a front is propagated in the image with a seed determined by a scalar potential that depends upon location in the medium. The framework aims to infer the boundaries of tubular structures in a first stage, using a standard surface evolution method. The potential function is then designed to take into account a Euclidean distance function from the boundary, so that the minimal paths are centred. Beyond the requirement that the user must specify the starting and end points of a particular path, the logarithm requires little user interaction. The flow is implemented using fast marching schemes and is hence computationally efficient [90].

Wink *et al.* have presented an approach to centreline extraction, applied in the context of vessel tracking, which combines features of the above two approaches. More specifically, they use the vesselness measure proposed by Frangi *et al.*, which is based on properties of the Hessian

matrix, to characterize putative vessel centreline locations. They then formulate the problem of finding paths between user selected points as a minimum cost path problem which they solve computationally using wavefront propagation. Their method has been validated qualitatively in the presence of stenoses and imaging artifacts [91].

A second class of methods aims to find centrelines of tubular structures which have first been segmented from 3D CT intensity images. Some applications have been proposed before by authors such as Bitter *et al.* and Paik *et al.* [92, 93].

The method of Bitter *et al.* is related to Deschamps and Cohens minimal path approach, but is formulated in a discrete setting. A graph is first built from a coarse approximation of a 3D skeleton. Each edge of the graph is assigned a weight which is a combination of Euclidean distance from a user defined source node and Euclidean distance from the boundary of the object. A centreline is then extracted using Dijkstra's shortest path algorithm on this graph [90, 92, and 94].

Paik *et al.* suggest a different approach where a minimal path is found on the surface of a tubular structure and is later centred. The user chooses the two end points of a desired path. The voxel on the surface of the object closest to each of the user specified points are then obtained. A path on the surface which minimizes the distance between these two points is then found. This path is then centred in the structure by applying a modified form of an iterative thinning procedure [93].

2.3.3.2. Flux Driven

The property of the flux that is utilized to find the spherical shapes is that at the centre of such shapes will have high negative flux values, a technique first introduced by Vasilevski and Siddiqi [95].

Flux analysis is used as a complementary technique to the shape index and Hessian based dot analysis. This feature approximates the divergence of image gradients by measuring the gradient flux through the boundaries of multiscale spheres. Its response is maximal at central vessel

locations and corresponding scale. It has been proved to be able to detect even low-contrast and narrow vessels.

Blum's grassfire flow develops the level sets of the Euclidean distance function to the boundary of an object. The singularities of this flow, which are the shock-front of the grassfire flow, are the location of the central points and can be employed to estimate the centre of the object. In our 3D objects the boundary is a closed surface. Motion of the boundary (front) can be modelled by the following equation [96]:

$$\frac{\partial S}{\partial t} = \hat{N}, \quad (2.34)$$

acting on a closed 3D surface S , such that each point on its boundary is moving with unit speed in the direction of the inward normal \hat{N} .

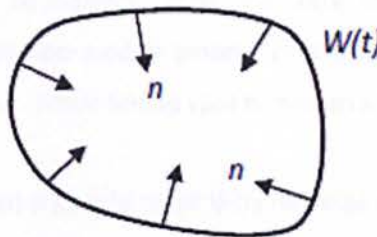


Figure 2.16: Blum's Glassfire Flow, moving forward and inward normal vectors [96].

Such equations are usually solved by looking at the evolution of the phase space of an equivalent Hamiltonian system. Let D be the Euclidean distance function to the initial surface S_0 . The magnitude of its gradient, $\|\nabla D\|$, is identical to 1 in its smooth regime. With $\mathbf{q}=(x,y,z)$, $\mathbf{p}=(D_x, D_y, D_z)$ and $\|\mathbf{p}\|=1$, the Hamiltonian system is given by $\dot{\mathbf{q}} = (0, 0, 0)$, $\dot{\mathbf{q}} = (D_x, D_y, D_z)$ with an associated Hamiltonian function $H = 1 + \|\nabla D\|$.

The discrimination of medial curve from non-medial surface points can be approached by computing the flux (F) of vector $\dot{\mathbf{q}}$ at a point. This quantity is given by

$$F(\dot{q}) := \frac{\int_{\partial R} \langle \dot{q}, \hat{N}_0 \rangle dS}{\text{area}(\partial R)} \quad (2.35)$$

where dS is a surface area element of the bounding surface ∂R of a volume R and \hat{N}_0 is the outward normal at each point on the surface. It can be shown that as a spherical volume shrinks to a point not on the medial surface, the flux through its surface approaches zero. In contrast, when such a volume shrinks to a medial surface point, the flux approaches a strictly negative number [97].

There is in fact a very precise relationship between the limiting values so obtained and the geometry of the object. The flux values are proportional to the sine of the object angle α , which is half of the angle between the vectors $\vec{P_1Q}$ and $\vec{P_2Q}$ in the plane passing through P_1 and P_2 and Q . Since these two vectors are perpendicular to the tangent planes to the boundary at P_1 and P_2 , respectively, the average outward flux measures the degree to which the medial manifold is parallel to the corresponding boundaries. Thus, the flux measure is an effective way to distinguish between medial and non-medial points. This calculation can be used to guide a thinning process in a cubic lattice, while taking care to preserve the objects topology [98].

A cubic lattice point is labelled a simple point if its removal does not change the topology of an object. Such a point has the property that its removal: i) does not create hole, ii) does not create a cavity and iii) does not disconnect a connected component. The classification of a simple point turns out to be one case of a more general categorization of a point x in a cubic lattice introduced. This categorization is based on two numbers:

- a) C^* : the number of 26- connected components 26-adjacent to x in $O \cap N_{26}^*$,
- b) \bar{C} : the number of 6-connected components 6 adjacent to x in $\bar{O} \cap N_{18}$.

Here, O is a 26 connected object N_{26}^* is the 26-neighborhood of x without x and N_{18} is the 18-neighborhood of x including x . Simple points can be identified by the condition $C^*=1$ and $\bar{C}=1$. The basic approach is to guide the thinning of the object by the average flux measure computed over a very small spherical neighbourhood, while taking care to only remove simple points. The

thinning process terminates when all surviving points are not simple, or have an average outward flux below some chosen value, or both. Unfortunately, the result is not guaranteed to be a thin set (without an interior). This last constraint can be satisfied by defining an appropriate notion of an end point in a cubic lattice. In R^3 , if there is a plane that passes through a point x such that the intersection of the plane with the object includes an open curve which ends at x , then x is an end surface. This criterion can be discretized easily to 26-connected digital objects examining 9 digital planes in the 26-neighborhood of x . The thinning process proceeds as before, but the threshold criterion for removal is applied only to end points [99].

In order to extract centreline paths, the medial surface of a cylindrical structure approaches a 3D curve centred in the objects interior. To compute centreline paths in single tubular 3D structures as well as more complex objects composed of segments that are tubular, the approach is to thin the medial surface to obtain a structure composed only of curves (the medial curve) and then prune the result to obtain well centred paths. A related algorithm for obtaining medial curves from digital manifolds was developed by Borgefors *et al.* The medial surface extraction algorithm described above can be modified to produce a point x that is an end point of a 3D curve or is on the rim or corner of a 3D surface will not be removed if its average outward flux is strongly negative [100].

In a cubic lattice, an end point of a 26-connected curve is defined as a point x whose 26-neighborhood $O \cap N_{26}^*$, only contains one point that is in the interior of the object. If the criterion for anchoring points is applied only to end points, every surface point will eventually be removed leading to a medial curve. Whereas this curve will lie on the medial surface, it will not necessarily be locally centred within a tubular object then the thinning is ordered by the flux. This measure sets the angle between the vectors $P\vec{1}Q$ and $P\vec{2}Q$.

A straightforward way to obtain centreline paths is to order the thinning by the Euclidean's distance function to the object's boundary, such that points which survive are as far away from the boundary as possible. The following steps of the algorithm described below in pseudo code presents the thinning procedure to extract medial curve.

Pseudo code for extracting the medial curve:

1. *For each given voxel X*
2. *Set the flux variable to zero*
3. *For each neighbour N of a voxel X*
4. *Compute the dot product of the vector field and central oriented vectors at N .*
5. *Add the result to the flux.*
6. *Divide Flux variable by the number of neighbour voxels*

The resulting medial curve is a 26-connected structure in a cubic lattice which is no more than one voxel thick. Thus, each point on a medial curve can be labelled by examining its 26-neighborhood, ensuring end points have only one neighbour, curve points have exactly two neighbours and junction points have at least three neighbours.

Once a centred medial curve is obtained some degree of pruning always needs to be carried out, depending on the desired output.

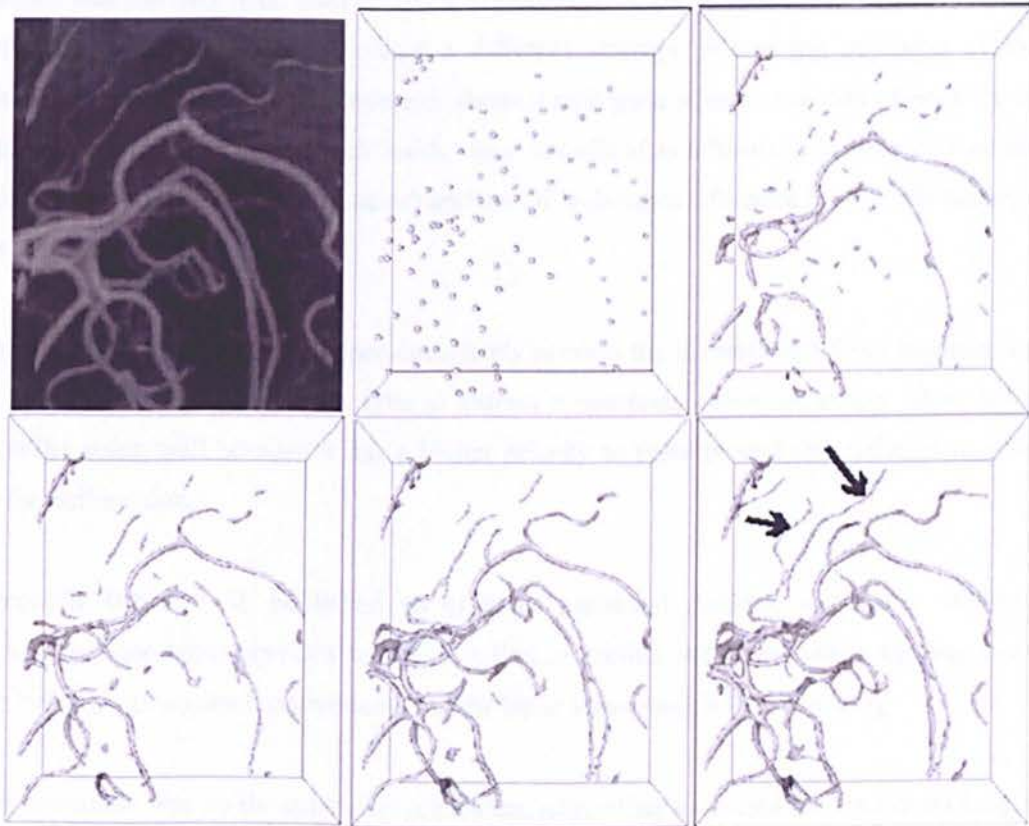


Figure 2.17: Flux-based level-set. [95]

Another recent approach exploiting the distribution of gradient vectors is the optimally oriented flux from Law and Chung (2008), where they developed a Fourier-based implementation and discuss the advantages of optimally oriented flux over Hessian-based measures, including more accurate and stable responses and higher robustness to disturbances from adjacent structures [95].

Similarly to the spherical flux Vasilevskiy *et al.* and M. Law *et al.* discussed above, the optimally oriented flux relies on the measure of gradient flux through the boundary of local spheres. The key difference lies in the exploitation of the vessel directionality through the estimation of an optimal gradient projection axis [101].

2.3.3.3. Distance Transform

An approach that has only been used on colon skeletisation is Bitter *et al.*, where he proposed a more efficient centreline algorithm using a different strategy, where the precision of the centreline is adjusted during the procedure of shortest path generation rather than afterwards. In this distance map the distance for each inside voxel is defined as a heuristic combination of the DFS-distance (distance from starting point) and the DFB-distance (distance from the boundary), which is called a penalty distance [92].

However, the penalty distance could not completely prevent the shortest path from hugging the corners. Furthermore, this algorithm fails to extract a complete colon centreline when holes appear on the colon wall because it has a higher priority to enter these holes rather than span through the entire colon.

More recently Bitter *et al.* published an efficient penalized distance volumetric skeleton algorithm, which combines previous work on finding centreline and its branches, and improves the work by making two small corrections, but the basic ideas remain the same [92].

The first correction was on the centreline algorithm, where they extracted the maximum length path instead of the maximum penalty path, among all the minimum cost paths in the penalized

distance field. Therefore, they could always extract the longest path as the centreline. Their second correction was in their branch extractor algorithm, where to extract a new branch, they computed a new penalty distance field from all voxels on the centreline and the branches detected so far, instead of always using the same penalty distance field from a fixed source voxel. In 2002 the branch extractor algorithm was once again improved to be more time efficient.

2.4. Summary

In this chapter we reviewed different methods to detect and segment various features, mainly related to the thoracic aorta in CAD systems.

The next chapter presents the detailed description of our fully automated CAD system developed for this project.

Chapter 3

Proposed CAD System

The proposed system consists of two major components, CAD and CAM, as illustrated in the diagram in figure 3.1.

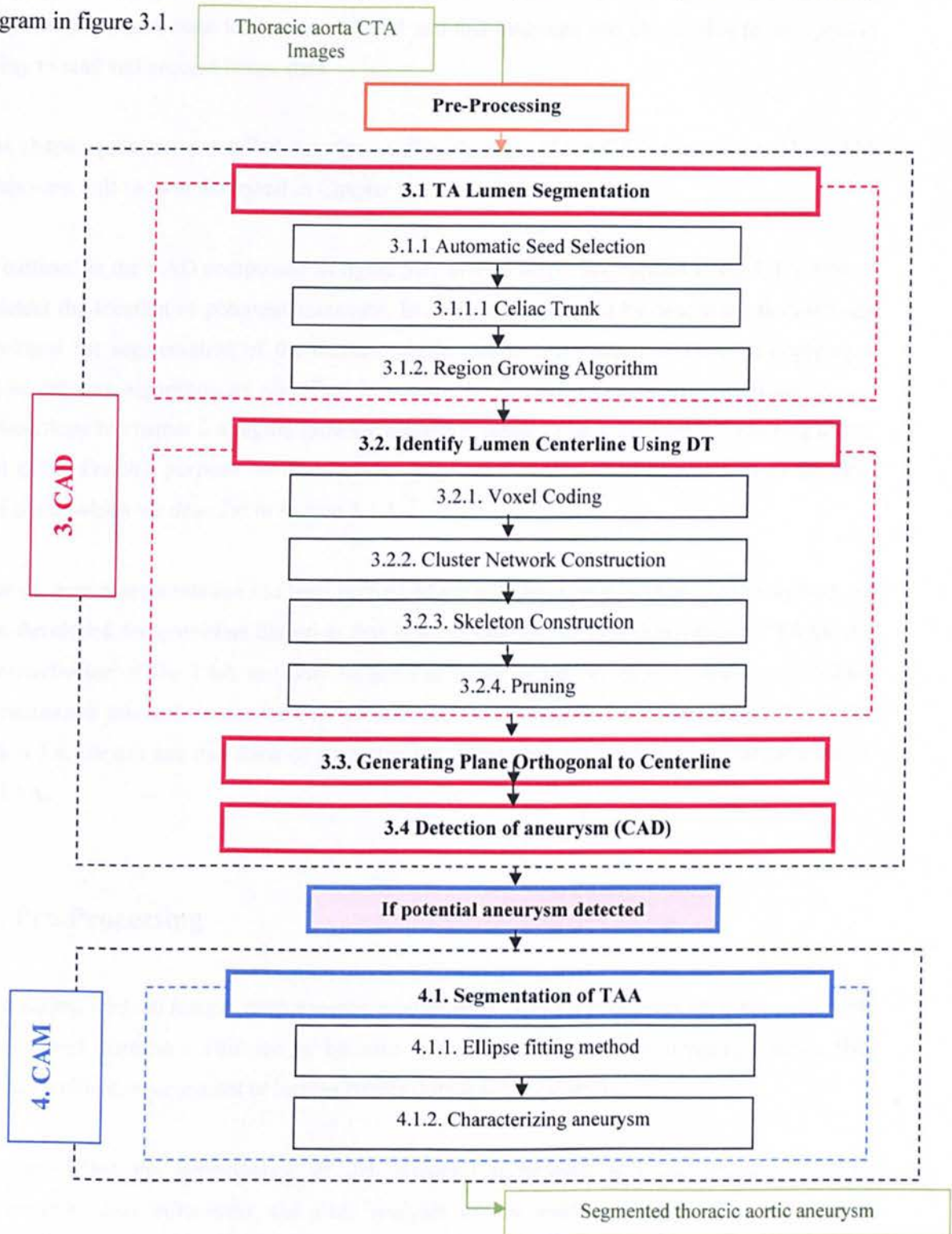


Figure 3.1: Flowchart of the proposed CAD/CAM system.

The first component CAD detects any potential thoracic aortic aneurysm. The second component of our system, the CAM component, characterizes the previously detected aneurysm. These methods have been implemented in C# and this language was chosen due to the specific ability to read and process image data.

This chapter provides a detailed description of each stage of the CAD component. The CAM component will be later described in Chapter 4.

As outlined in the CAD component in figure 3.1, several stages are applied to the CTA dataset to detect the location of potential aneurysm. In section 3.1 we start by describing the methods developed for segmentation of the thoracic aortic lumen. Our method consists of applying a region growing algorithm, as described in section 3.1.2. But as previously discussed in our methodology in chapter 2 a region growing algorithm needs to be initialized by selecting a first seed point. For this purpose we developed a fully automated method of selection of the first seed point, which we describe in section 3.1.1.

Once the lumen segmentation has been performed we will describe in section 3.2 the method we have developed for centreline detection that is important for the characterization of TAAs. As characterization of the TAA can only be done in slices of the orthogonal plane to centreline (reconstructed images), in section 3.3 we describe the method for generating them. Lastly in section 3.4, we can use this stack of reconstructed images to detect any potential algorithms in the TAA.

3.1. Pre-Processing

The acquired medical images from imaging modalities such as CTA devices are often corrupted by noise and distortion. This can be because of random disturbance in imaging devices, the effect of ambient environment or human factors during the acquisition.

This can affect the performance of the detection techniques and the accuracy of the segmentation thus influencing the final analysis of the medical images. Therefore, pre-processing the imaging data is the first step of the proposed CAD/CAM system which aims to smooth the image, remove noise while preserving the integrity of edges and enhancing the

features. The pre-processing technique used is based on the anisotropic diffusion filtering, which we describe in section 2.3.1.1.3.

3.2. TA Lumen Segmentation

To be able to identify potential aneurysm in the TA we first need to segment the TA lumen. In this section we will describe our developed algorithm for automatic segment the thoracic aorta.

Our main priority was to automate the method of seed selection so that there will be no manual interaction needed by the radiologist. Seed point will therefore, be used as the starting pixel for our segmentation algorithm, region growing.

3.2.1. Automatic Seed Selection

As previously mentioned, our goal was to develop a fully automated system. This would mean to automate the first seed point selection where no human interaction is needed.

After thorough research we have decided that the best method to automate the seed point selection was to find the position of the celiac trunk as it is one of the major branches out of the descending aorta and therefore, a common landmark in every human body. Once we have the location of the celiac trunk we can easily identify the largest vessel in the CTA slice and therefore we can start our segmentation algorithm.

In this section we will explain in more detail our method for selection of initial seed point.

3.2.1.1. Celiac Trunk

The first slice for automatic seed point detection is identified automatically by finding the positions of the junction of the Celiac Trunk, as illustrated in figure 3.2 (a). In figure 3.2 (b), our generated 3D image for easy visualization of the celiac trunk is illustrated.

The Celiac Trunk is located below the diaphragm, which is approximately where the lung ends. So, the lung region is identified initially before searching for the Celiac Trunk.

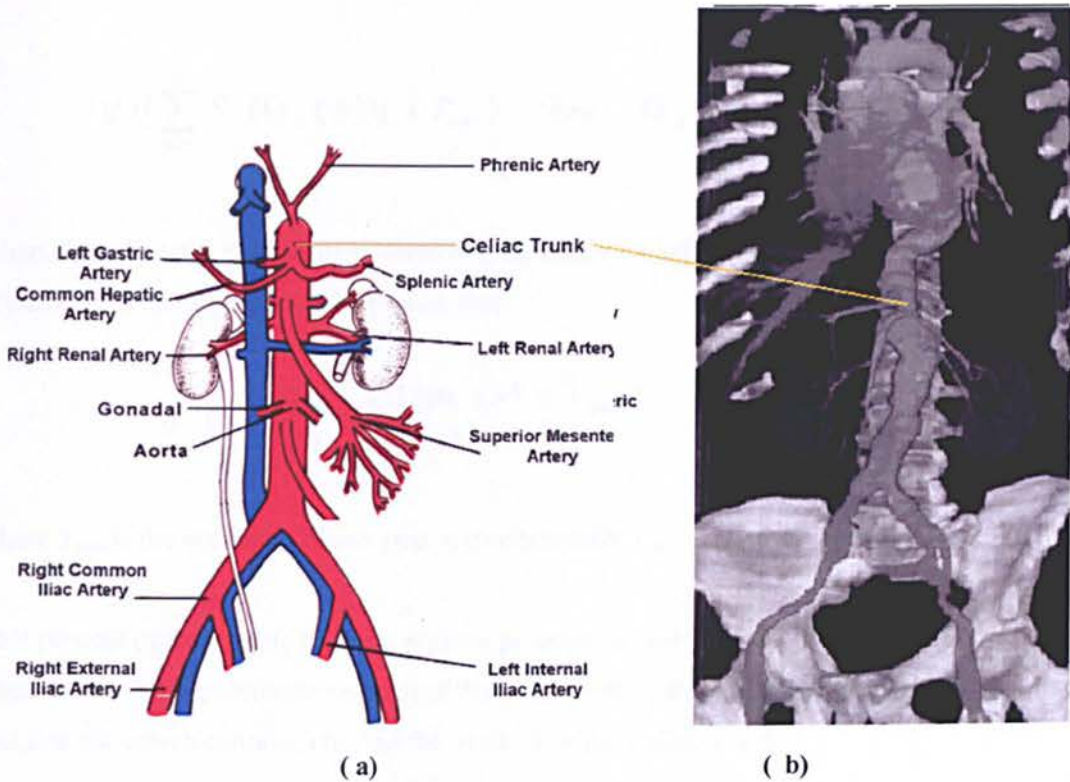


Figure 3.2: (a) schematic overview of the celiac trunk (b) generated 3D image of the celiac trunk.

Lung regions appear as hollowed objects in the CT images due to the presence of a large volume of air, as shown in figure 3.3(a) and 3.3(b). Using intensity threshold segmentation combined with morphological hole-extraction algorithms, lung regions can be extracted. Each extracted hollowed object (lung region) is then examined to see if it contains several small holes. These small holes are the result of cross-sectional views of many blood vessels in the lung region.

The cross-section of a segmented lung in figure 3.3(c) shows the presence of many small holes. In order to extract the small holes, each lung region, in each slice, is first flood-filled and then subtracted from the original segmented lung.

The identification of lung objects proceeds by counting the number of the isolated objects above a given size within the hollowed regions; i.e. small isolated objects are considered to be noise

and are ignored. Let O_k be the k th extracted hollowed object in the current slice, then O_k is part of the lung region ($O_k \in L$) if the following condition holds,

$$\text{if } ([\sum_{p=0}^N S(O_k(p))]) > T_{cnt} \text{ then } O_k \in L \quad (3.1)$$

where N is the total number of isolated objects inside the k th object O_k , $O_k(p)$ is the p th isolated object, T_{cnt} is the object count threshold, and

$$S(x) = \begin{cases} 1 & \text{if } (size(x) > T_{size}) \\ 0 & \text{otherwise} \end{cases} \quad (3.2)$$

where T_{size} is the minimum object size. Experimentally $T_{size} = 5$ and $T_{cnt} = 10$ are used.

This process of identifying the lung regions proceeds slice-by-slice until no lung region is found. This will be the approximate location of the diaphragm or the end of the lung regions. From this location the search continues to find the location of the Celiac Trunk.

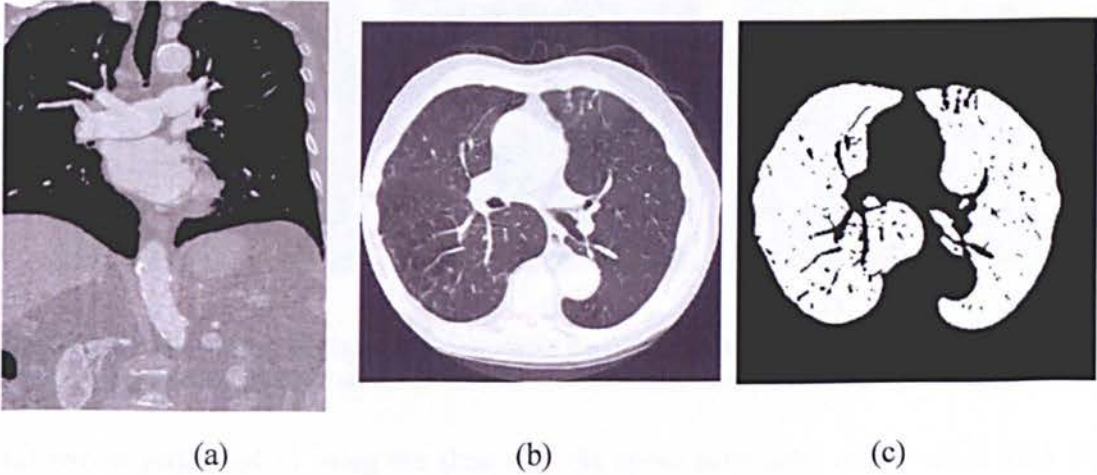


Figure 3.3: Lung regions. (a) Coronal view showing aorta below the lung regions (white arrow), (b) axial view of a lung, (c) extracted lung following thresholding and a morphological operation.

From the end location of the lung a sub-volume is obtained to confine the search volume. This search volume is taken from within a volume of an enlarged lumen (20% enlargement) and limited to 40mm above and 120mm below the end-of-lung location.

By using an adaptive segmentation such as Otsu, a new lumen is obtained within the search volume to ensure that a fully detailed lumen is obtained. Note that the previously extracted lumen lacks detail due to the morphological operation.

Two morphological operations of erosion and dilation with different window sizes will result in separating the branches from the main lumen. Based on the fact that the celiac trunk is the first branching off from the lumen below the diaphragm, it can be identified as the isolated region that is located on the upper-most part of the image in figure 3.4(c).

Once the isolated Celiac Trunk is found, the upper-most point that would join the projected lumen (figure 3.4(b)) is chosen as the start of the thoracic section of the lumen.

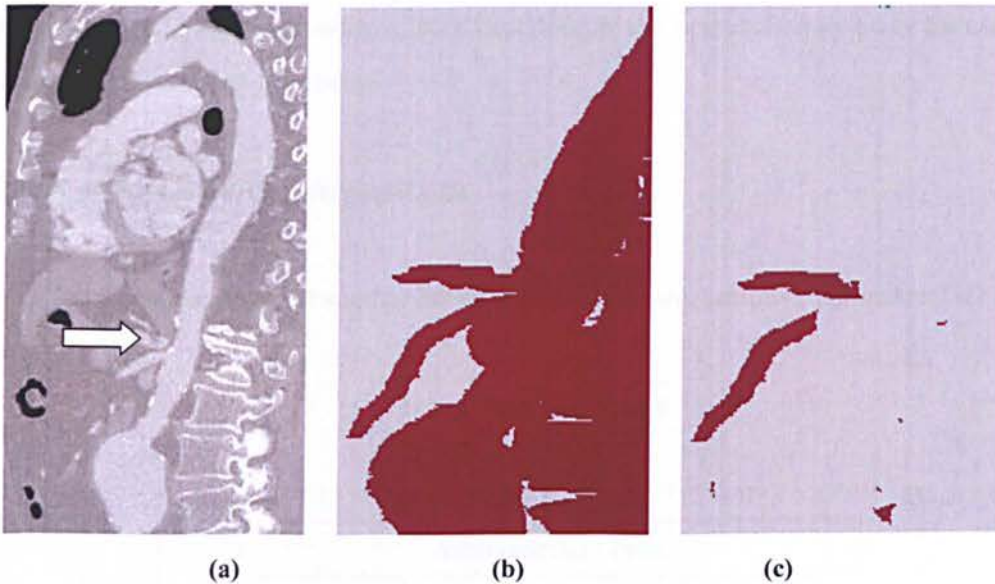


Figure 3.4: Celiac Trunk, (a) Sagittal view showing the Celiac Trunk (arrowed), (b) Projected sagittal view of a segmented aorta, (c) result of morphological operation performed on b).

This step is performed by using the slice with the upper most point of the celiac trunk and thresholding it, where we can distinguish the biggest object as the thoracic aorta due to the anatomical knowledge acquired before.

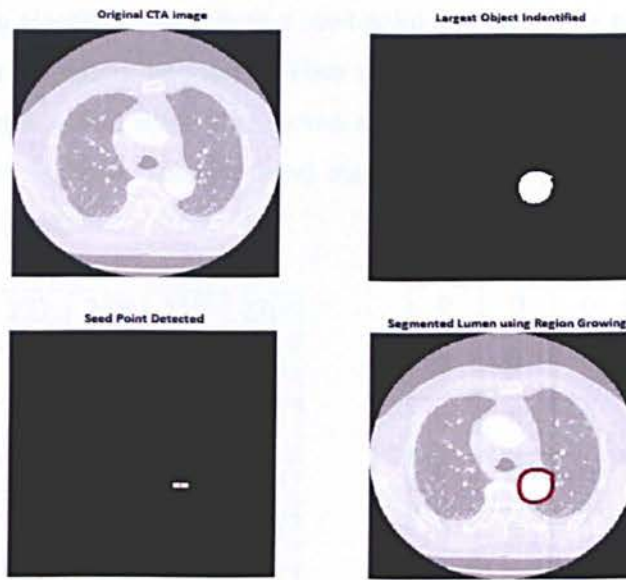


Figure 3.5: Detection of first seed point for region growing method illustration.

We can then start the region growing method described in the next section by using the centre point of the aorta as a first seed point.

3.2.2. Region Growing Algorithm

Once we have detected the first seed point we can initialize our adaptive parametric 3D region growing.

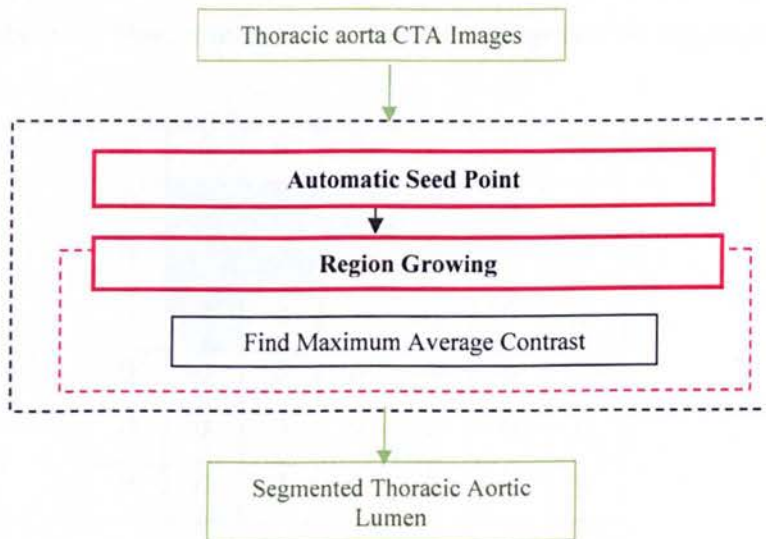


Figure 3.6: Flow chart of image segmentation of aortic lumen.

Our region growing algorithm starts from a seed point and extends it by absorbing the highest gray level point on its current boundary. When several pixels in the neighbourhood have the same gray level value a first come first served strategy is employed. If it is a homogeneous region and the process starts from the local maximum point, points with lower values will consecutively join the region.

195	255	243	222	248	212	230
230	252	254	239	241	220	118
241	222	255	250	253	230	244
223	223	249	256	250	250	230
255	244	240	195	252	192	298
198	255	230	248	249	212	234
188	166	200	197	239	240	246

0	0	0	0	0	0	0
0	0	0	0	0	0	0
0	0	0	0	0	0	0
0	0	0	1	0	0	0
0	0	0	0	0	0	0
0	0	0	0	0	0	0
0	0	0	0	0	0	0

Figure 3.7: First image on the left is the matrix of the input image. Picture on the right represents the matrix of the seed point on the output image matrix of zeros.

During the growing process the boundary changes dynamically. To describe the algorithm we show figure 3.7. The algorithm is applied to the image starting from the pixel (seed) with gray level 256.

Then the algorithm looks around in its 8-neighbourhood and finds the highest grey value and labels it with number two. Then, it finds new neighbours and updates the neighbouring points to the region.

0	0	0	0	0	0	0
0	0	0	0	0	0	0
0	0	2	0	0	0	0
0	0	0	1	0	0	0
0	0	0	0	0	0	0
0	0	0	0	0	0	0
0	0	0	0	0	0	0

Figure 3.8: Image shows second seed point labelled on the output image. The labelled neighbouring pixels to the region are labelled in yellow and blue.

Next the algorithm searches around the labels pixels looking for the highest gray level and finds it being 254 and labels it as being number 3. Followed by looking for new neighbours in the 8-neighborhood which are not labelled and record them as boundary points.

0	0	0	0	0	0	0
0	0	3	0	0	0	0
0	0	2	0	0	0	0
0	0	0	1	0	0	0
0	0	0	0	0	0	0
0	0	0	0	0	0	0
0	0	0	0	0	0	0

Figure 3.9: Image shows third seed point labelled on the output image. The image shows the neighbourhood of the region in zero with coloured background.

The algorithm stops when all the pixels in the image are labelled as the region or boundary points. During the process the average contrast is calculated. The average contrast is the mean of the region minus the mean of the boundary. The average contrast starts from low values and increases to a local maximum when all the points absorbed. It then reduces to lower values when the growing continues absorbing pixels in the background. An example is shown the average contrast in figure 3.10.

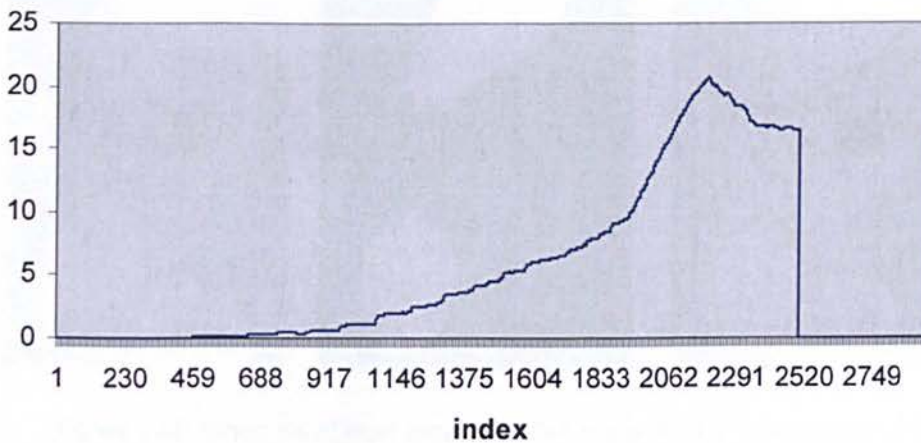


Figure 3.10: Graph of average contrast of CTA image 01087.

The peak with the highest average contrast is found when the pixels in the region are absorbed.

The average contrast, which uses grey level difference information, represents the final condition in order to produce the image segmentation. This is used to find the external boundary of the region, which is shown under in figure 3.11.

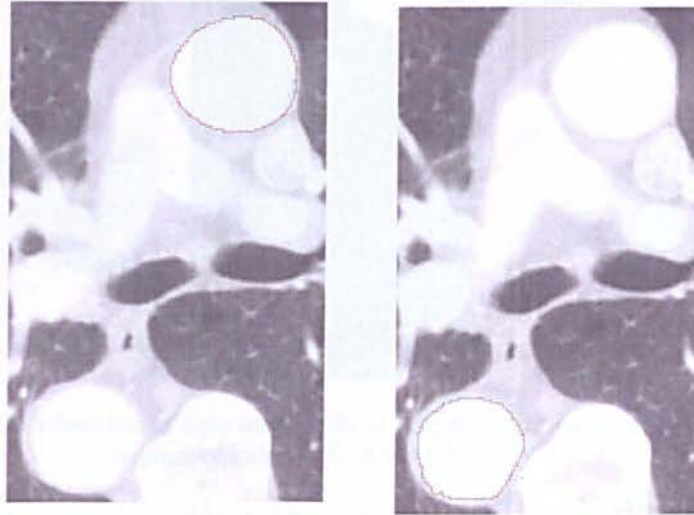


Figure 3.11: Labelled boundary of the aortic lumen.

In figures 3.12 -13, we can observe the three stages of the algorithm, from inputting the original image then the labelling of the boundary of the aortic lumen, and finally the output image which shoes the segmented aorta. This particular slice makes part of the aortic arch.

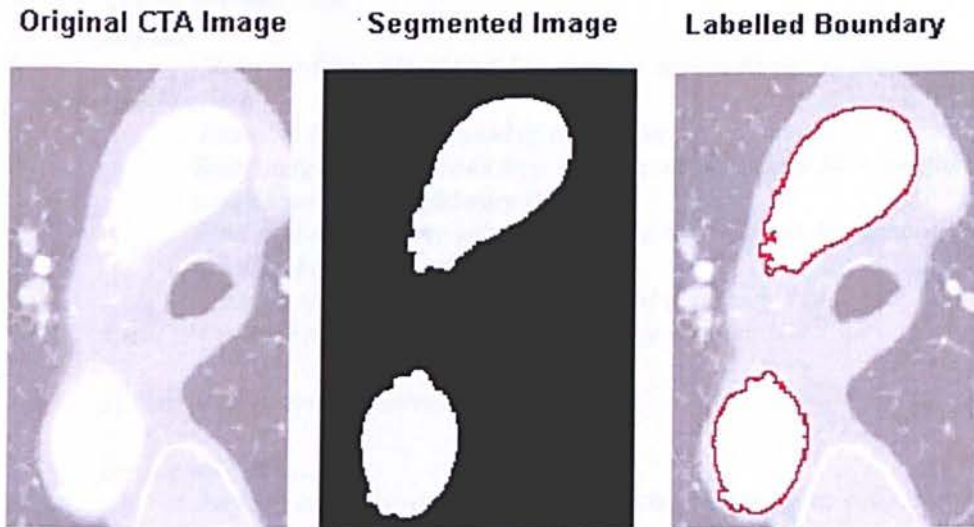


Figure 3.12: Schematic of input image, labelled region in the image, and output image (segmented image). (CTA slice 1053)

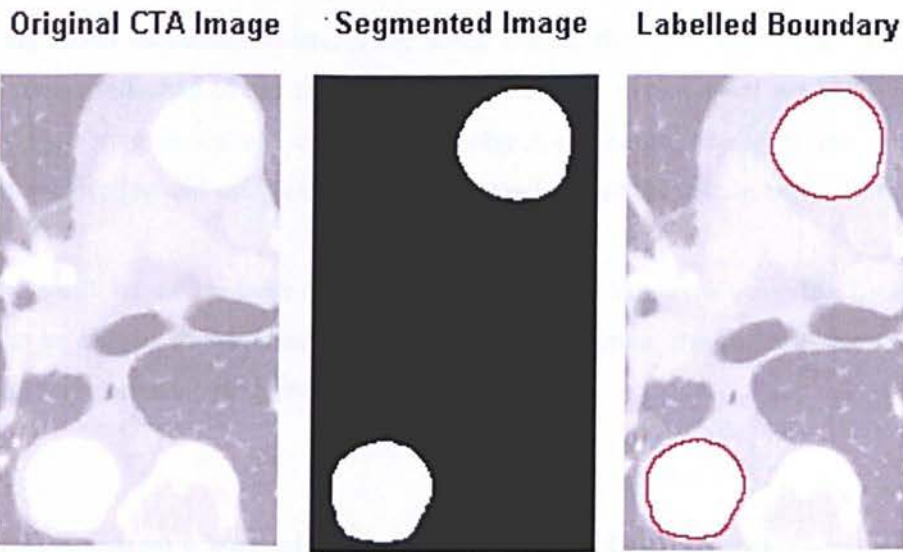


Figure 3.13: Schematic of input image, labelled region in the image, and output image (segmented image). (CTA slice 1068)

The following pseudo-code is written to load up all the images. It calls the region growing algorithm and saves the output images on a file.

Pseudo code of the basic steps of this algorithm can be outlined in 17 states:

1. *I* Input automatic seed point coordinates
2. Create region list
3. Create boundary list
4. **Repeat**
5. Store seed point in region list – create region $R_i = \{\text{seed point } 1, \text{seed point } 2, \dots, \text{seed point } i\}$
6. Examine 8-neighbourhood of seed point
7. Store neighbours in boundary list – create boundary $B_i = \{\text{neighbours } 1, \text{neighbours } 2, \dots, \text{neighbours } i\}$
8. Find highest intensity value pixel in the region's neighbourhood, not labelled before in region list
9. Change seed point coordinates to point determined at 4
10. **Until** the seed point reaches one of the image borders
11. **II** Calculate Average Contrast
12. **for** region = $R_1 \dots R_n$
13. Average contrast = difference between the average gray value for pixels in region R_i and the average gray value for pixels in region boundary B_i
14. store average contrast
15. **end for**
16. Create graph of average contrast
17. Inspect graph and determine index of peak
18. Inspect matrix find region labelled for index

The above algorithm successfully detects the aortic lumen. However, sometimes some small objects still remain attached to the thoracic aorta. In order to detach them we apply different methods for extracting in certain cases middle object or largest object of the image, all depending on its location and using our anatomical knowledge of the human body.

Only once the aortic lumen has been detected it is necessary to locate the centreline (or skeleton) of the aorta to be able to characterize it. Hence in the next section, the skeleton extraction and view direction calculation are described in detail.

3.3. Identify Lumen Centreline using Distance Transform

We have chosen to use a skeletonization method based on distance transform. As we are working with large 3D volumetric DICOM data sets, where computational time is extremely important factor, distance transform application was the most appropriate method due to its computational efficiency.

3.3.1. Voxel Coding

Voxel Coding plays a critical role in a proposed thoracic aorta skeleton extraction. It is responsible for skeleton extraction, refinement, smoothness and connection operations. Following a voxel by voxel propagation procedure within a 3D binary segmented aorta starting with a seed point, voxel coding generates a minimum distance field [102].

The algorithm employs two distinct coding operations: boundary-seeded (BS) voxel coding and single point seeded (SS) voxel coding. The BS coding generates a traditional minimum distance field (BS field) in the volumetric object based on the boundary points of the object, while SS-coding generates another similar minimum distance field (SS-field) corresponding to a single point as reference point rather than the object boundaries.

The propagation process is similar to the implementation of a discrete minimum distance transform or, more generally, a region growing operation.

Once a voxel is visited, a value is assigned, indicating how far away it is from the seed points of the growing region. A voxel value field is constructed after the propagation. A voxel propagation operation normally uses “ $n_f - n_e - n_v$ ” distant metric instead of Euclidean distance.

BS coding employs 3-4-5 distant metric. Initially, the BS code values of “Seed Set” with the object boundary points are set to be zero, the object voxels are set to be infinite, while the background voxels are set to a negative value. Iteratively, for each voxels with a value of n , its F-neighbour, E-neighbour and V-neighbour are replaced with values of $n+n_f$, $n+n_e$, and $n+n_v$, respectively, if these values are smaller than the existing values.

This coding process continues until the constraint conditions are met. Figure 3.13(a) shows a synthetic image and its BS field is shown in figure 3.13(b).

The region propagation processing for SS-coding is only based on single seed voxel as reference point, and the voxel code generated records propagation order. The distant metric for SS-coding is 1-2-3 in proposed system. The SS-field classifies the object into a collection of clusters. Each cluster consists of connected voxels with the same SS code.

The SS code field, which provides information of object connectivity and topology, plays important roles in both cluster network construction and skeleton extraction. Figure 3.14(c) shows the SS code of a synthetic 2D image in figure 3.14(a).

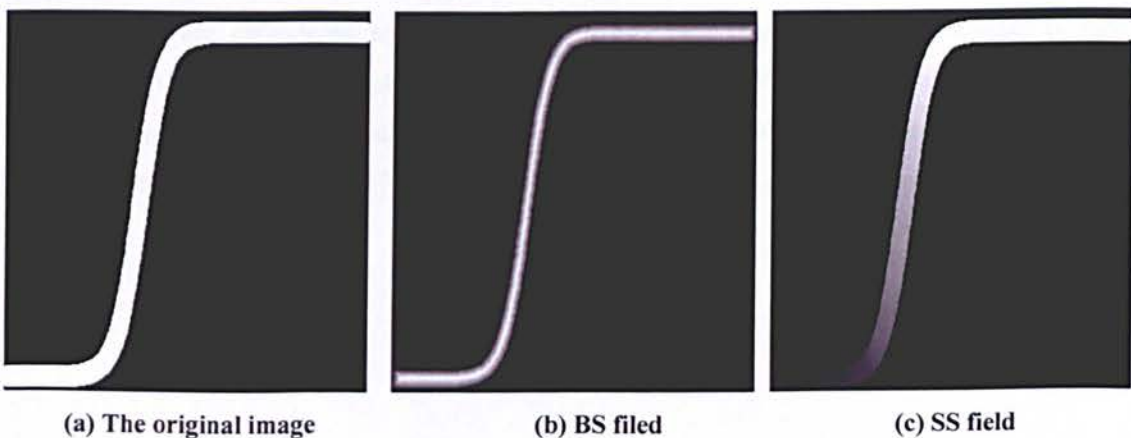


Figure 3.14: (a) shows a synthetic image (b) BS code of synthetic images (c) SS code of a synthetic 2D image.

3.3.2. Cluster network construction

The cluster generation is based on SS field from previous stage. Cluster network generation is to create a direct cluster graph based on the SS field, which provides the connectivity structure of the 3D object. The network construction consists of two steps, namely, cluster creation and cluster connectivity.

Cluster creation

After the SS-field distance transformation is first applied on the 3D binary object, each object voxel has one code value based on the simplest “1-2-3” metric, indicating how far away it is from the seed point, while the starting reference seed point is assigned to 0. The SS-coding classifies the object into a collection of clusters.

A cluster is defined as a connected set of object voxels with the same SS-code. The cluster is regarded as smallest element of volumetric object instead of single voxel. For all the voxels have the same SS code value, 3D region growing was used to group all the connected (26-connectivity) voxels as one cluster. More than one cluster can have same SS code.

Cluster Connectivity

Two clusters are considered to be connected if any two voxels from each cluster is face-connected. A cluster's parent clusters is defined as a connected cluster whose SS-code is one less than current one, and the children clusters is the connected cluster whose SS-code is one more than current one. Figure 3.15 shows the directed cluster graph constructed based on the SS-code.

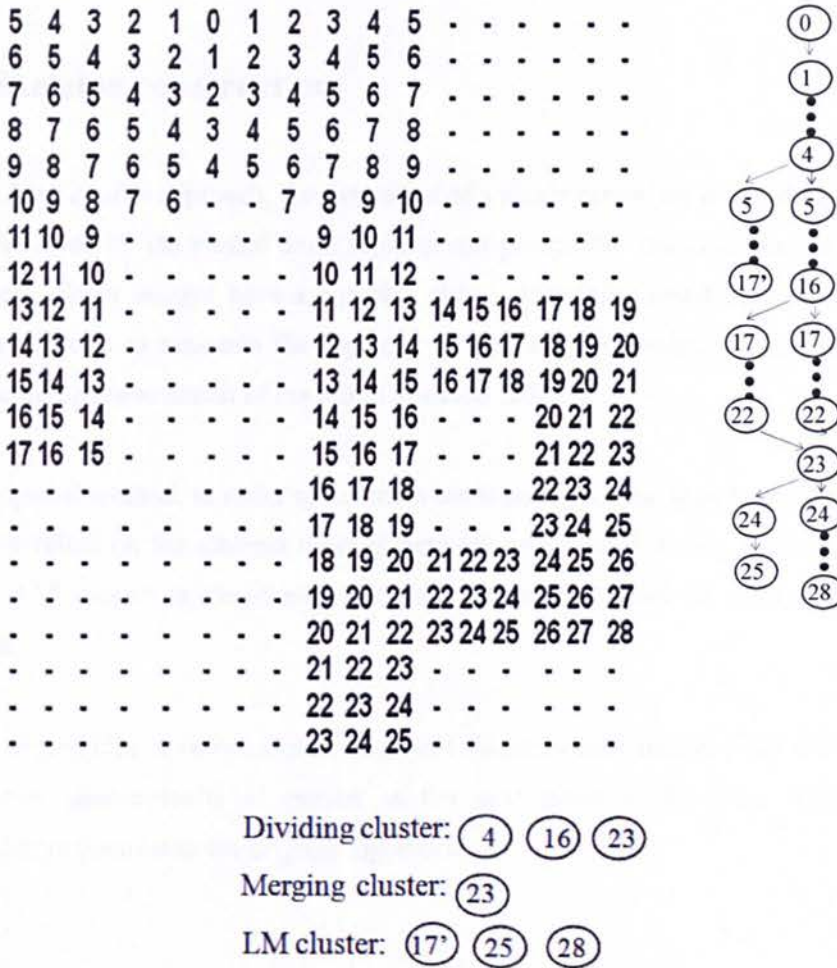


Figure 3.15: SS filed of synthetic image and its Cluster network.

The cluster graph provides the connectivity information for all the clusters contained in SS-field. The clusters with same SS-code belong to same layer. The cluster that has more than one parent is defined as merging cluster. The cluster that has more than one child is defined as dividing cluster. A local maximum (LM) cluster has no child cluster. The LM cluster, dividing cluster and merging cluster play an important role in skeleton extraction. They are the critical nodes in the cluster graph.

The cluster graph can be considered as connected centreline network, providing all the guideline for the extraction of the skeleton. In the next section we introduce the details of extraction procedure.

3.3.3. Skeleton construction

In Yong Zhou *et al.*'s approach, the extraction of a single centreline is based on the shorted path method followed by the medial point replacement procedure. The centreline is also referred as medial path. Some images have a complex shape, containing small holes as shown in figure 3.15 it is difficult to maintain the topology structure by following the original shortest path procedure in the construction of the initial skeleton [102].

In our proposed method, in order to maintain the topology of the object, the initial extraction is completely relied on the abstract clusters network constructed during previous stage. Starting from the LM cluster in the cluster network, the medial point of each adjacent cluster is connected.

When a merging cluster is met, one of its parent clusters whose medial point is closest to current medial point geometrically is chosen as the next point in the path. This is significant modification in contrast to the original algorithm.

3.3.4. Smoothing and Pruning

In relation to the refinement and smooth operation of centreline, in general, the medial points of two connected clusters are not 26-connected geometrically. The refinement procedure is needed to close the gap between two adjacent medial points in the initial extracted path since one of the basic requirements for skeletonization of an object is connectivity. The refinement procedure employs the shortest path procedure based on local SS coding with two adjacent medial points as starting and ending respectively.

After refinement of the skeleton, the medial path could be jagged or self-intersect in the middle. In order to remove the knotted and folded segment of the path, a simple voxel coding method is used to smooth the path. The SS coding is applied on the refined medial path, which is considered as binary 3D object; shortest path procedure is followed to obtain smoothed one-voxel thick medial path.

The final step to construct completed skeleton is to connect multiple medial paths together without destroying the topology of the object. The cluster network constructed in the previous stage provides the information of the relationship among individual medial paths. In the proposed method, the connection procedures are performed with an innovative introduction of a constrained area during connection between two clusters.

The local SS transform is done within the constrained area, which consists of all voxels belong to two adjacent clusters to be connected. The connection with constrained area guarantees that the newly added path between two individual centrelines will not intersect with any other existing medial paths, so that the topology of the object can be preserved after connection.

Figure 3.16(b) shows the completed skeleton using proposed method and 3.16(c) after pruning.

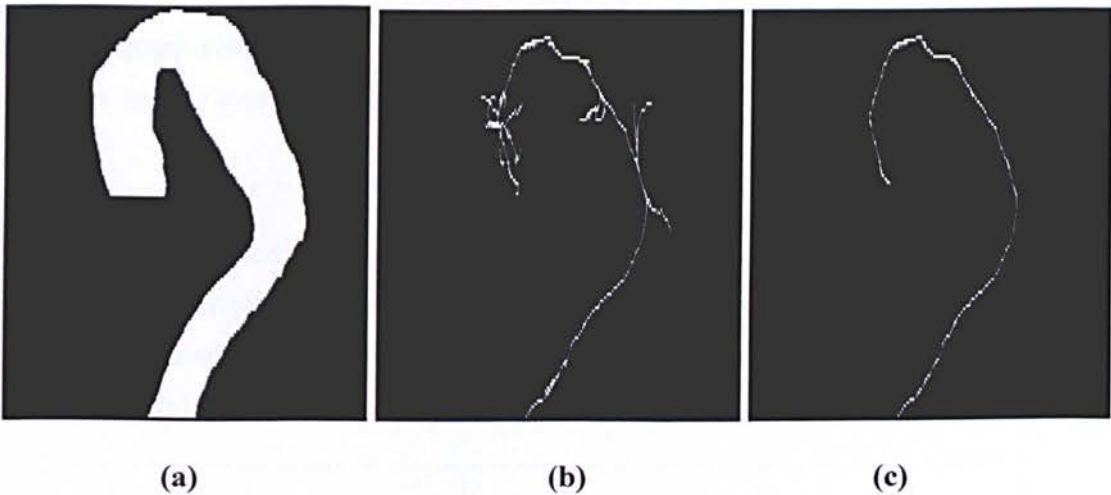


Figure 3.16: (a) original image, (b) resulted skeleton from original algorithm, (c) resulted skeleton from modified method.

Once a centreline is obtained, some degree of pruning has to be carried out. The goal is to extract a single centreline path, with the idea being to compute the shortest path from every end point on the medial curve to every other end point and then pick the longest path as the centreline path, as illustrated in figure 3.16(c).

3.4. Generating plane orthogonal to lumen centreline

For accurate detection and quantification of the thoracic aorta it is necessary to use the orthogonal image of the vessel. This step is applied following the detection of the centreline previously described in section 3.3.

The algorithm uses the Fast Harley transform (FHT). This is done because the Harley transform works on real valued functions and produces only real coefficients. The Fourier transform on the other hand would require us to store complex numbers which would double the memory requirement [103].

In this method we create multiple view aligned slices by creating multiple parallel planes at uniform distances from each other along the view vector (centreline).

The orthogonal plane is defined by using the coordinate of the considered point on the centreline and the average direction of the centreline at that point, as the normal vector of the plane.

Two vectors that passed through the centreline coordinate, orthogonal to the central axis and to one another, described an orthogonal plane with the vessel segment midpoint as the origin. Cubic interpolation was performed to obtain the values of the orthogonal slice. This procedure is also illustrated in figure 3.17.

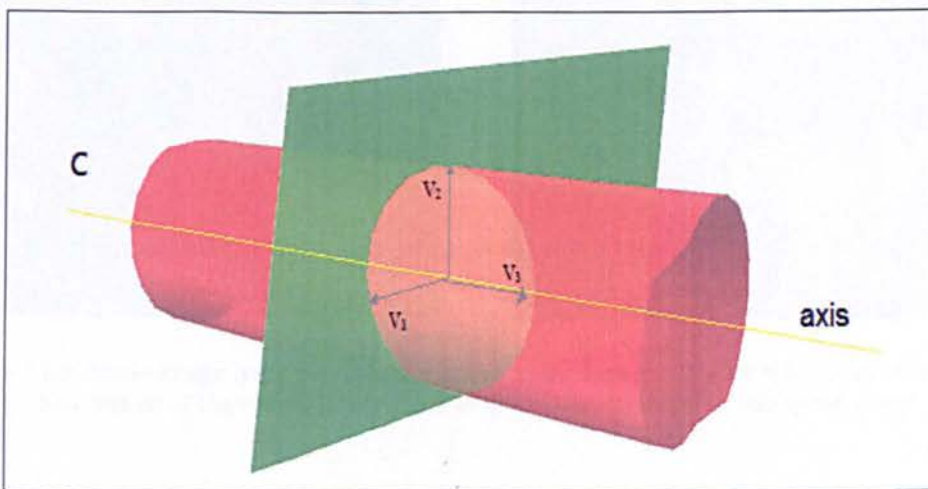


Figure 3.17: Schematic of vessel segment central axis and orthogonal plane through segment midpoint.

One characteristic that can be observed is how the thoracic aorta takes a circular shape in the transaxial slice of the CTA and an elliptical shape in the orthogonal slice to the centreline as can be seen in figure 3.18.

In this figure we have a schematic of the entire aorta and illustrating how the planes (transaxial and orthogonal) sit, as well as having an actual vessel segment cross-sections in of both planes.

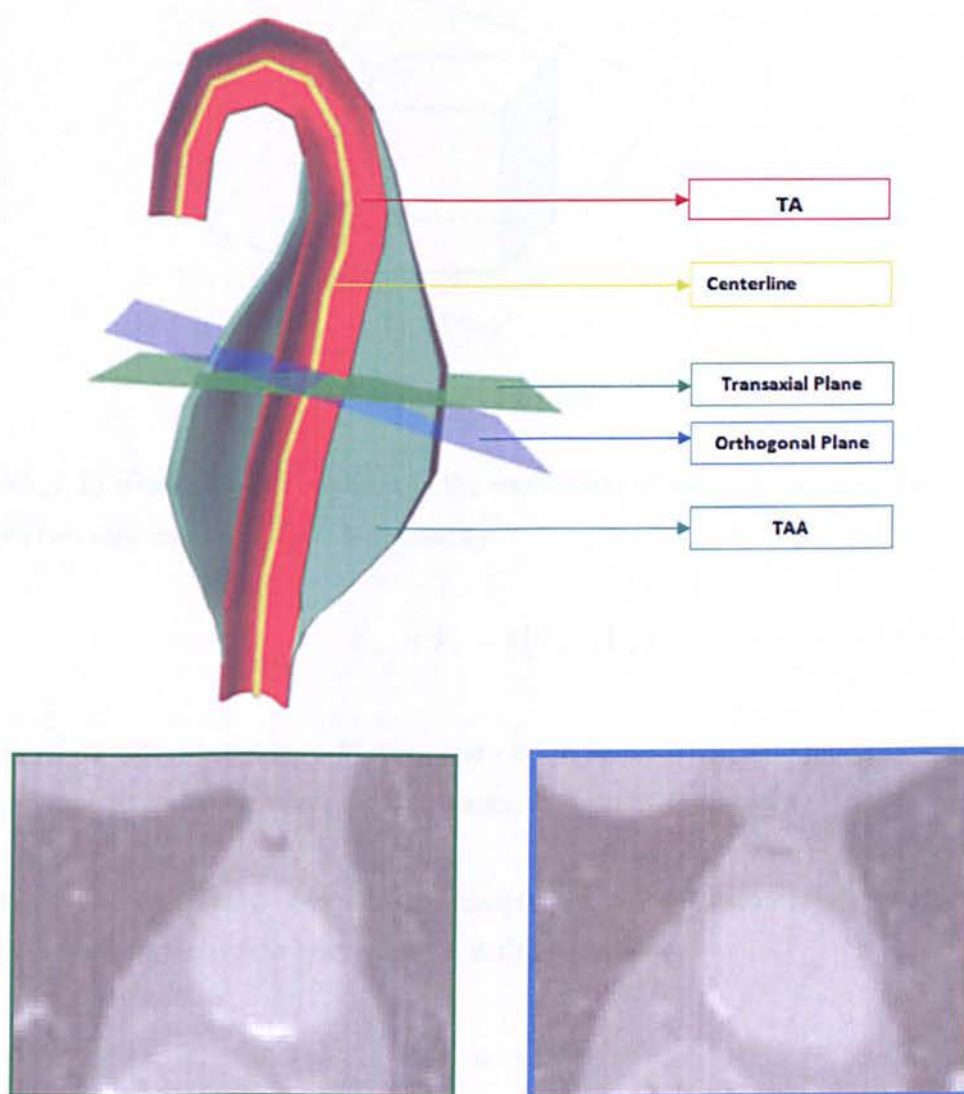


Figure 3.18: Above image is the 3D rendering of the aorta. Lower left: slice with its circular shaped cross section of the vessel. Lower right: elliptical shaped vessel in orthogonal plane.

A face of triangle method is applied to estimate the plane orthogonal to the centreline. We use coordinates of the centreline point to define the orthogonal plane, and average the direction of the centreline at that point, as being the normal vector of the plane [104].

The cube has 8 vertices and 12 edges, and the plane can cut at least 3 (and a maximum of 6 edges of the cube as shown in figure 3.19).

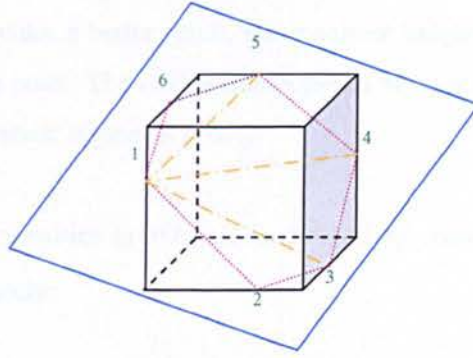


Figure 3.19: Cube.

If $V_i = (x_i, y_i, z_i)$ when $(i=1-8)$, represents the coordinates of the cube vertices, the edge lines between two vertices i and j (E_{ij}) is defined by

$$E_{ij} = V_i + s(V_j - V_i) \quad (3.3)$$

where i, j have values between $(1-8)$, $i \neq j$, and s is the fractional distance along the edge which is $[0, 1]$ for the points on the edges in other words, between two vertices.

To have a plane orthogonal to centreline we need to use a normal vector $n=(a,b,c)$ which passes through the point (x,y,z) of the centreline. It is defined as follows:

$$P = ax + by + cz \quad (3.4)$$

The point of intersection can be found by substituting values between $0 \leq s \leq 1$, in the edge equation 3.3, and replacing into the equation 3.4 the fractional distance can be calculated.

We choose one of the intersecting points as the reference point and the plane is divided into separate triangles by connecting this reference point to other intersected points (as shown in

figure 3.18). In this way, the plane can be reconstructed by considering all defined triangles (figure 3.19). The surface of each triangle can be traced to compute the coordinates of points on the intersected plane with an arbitrary resolution. Then the 3D coordinate is used to interpolate and estimate the intensity of the points on the plane.

There are several methods of 3D interpolation: nearest neighbour, linear interpolation, cosine interpolation and cubic interpolation. From these methods we have chosen to use cosine interpolation as it provides a better result, since nearest neighbour and linear interpolation have discontinuities at each point. The cosine interpolation has a smoother interpolating function and transition between adjacent segments [105].

For interpolation of intensities in 3D, $\varphi u2$ is defined by considering the difference along x, y, and z directions separately:

$$\varphi u2 = \left[\frac{1 - \cos(\varphi u.x \times \pi)}{2} \right]_i + \left[\frac{1 - \cos(\varphi u.y \times \pi)}{2} \right]_j + \left[\frac{1 - \cos(\varphi u.z \times \pi)}{2} \right]_k \quad (3.5)$$

Consider pix_0 is a point on the intersected plane and the intensity of this point is requested. This point is located between 8 points (pix_{000} to pix_{111}) as follows:

$$\text{pix}_{\forall (ijk) \in C} = (\text{pix}_0.x + i, \text{pix}_0.y + j, \text{pix}_0.z + k) \quad (3.6)$$

where $C = \{(000), (001), (010), (011), (100), (101), (110), (111)\}$.

The intensity of pix_0 is the interpolation of the intensities of all the points in equation 3.6. First, the interpolation is applied to intensities in the x direction and the four points are computed as follows:

$$\text{Int}_{\forall (ij) \in P} = (1 - \varphi u2.x) \times \text{Ints}(\text{pix}_{0ij}) + \varphi u2.x \times \text{Ints}(\text{pix}_{1ij}) \quad (3.7)$$

Where $P = \{00, 01, 10, 11\}$ and $\text{Ints}(\text{pix}_{000})$ estimates the intensity of the image at coordinate pix_{000} . Subsequently the interpolation is applied in the y direction and two further values are computed as follows:

$$Int\ 0 = (1 - \phi u 2, y) \times Int\ 00 + \phi u 2.y \times Int\ 10 \quad (3.8)$$

$$Int\ 1 = (1 - \phi u 2, y) \times Int\ 01 + \phi u 2.y \times Int\ 11 \quad (3.9)$$

Lastly another cosine interpolation is applied in the z direction on the previous results and the new result will be assigned to the intensity of the considered point:

$$Ints (pix\ 0) = (1 - \phi u 2.z) \times Int\ 0 + \phi u 2.z \times Int\ 1 \quad (3.10)$$

As result of this process the orthogonal planes to centreline have been detected as illustrated in figure 3.20

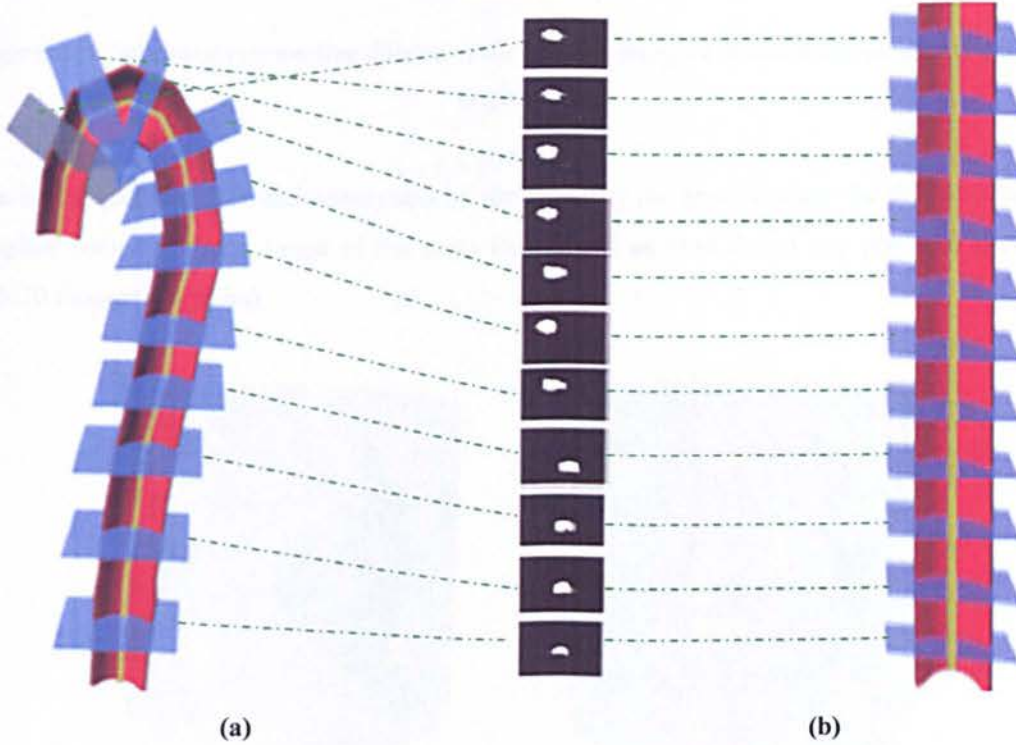


Figure 3.20: a) Orthogonal plane detected, b) stack of images converted.

3.5. Automatic detection of aneurysm (CAD)

Using the stack of reconstructed images (orthogonal) we once again apply the region growing method as previously described in section 3.2.1. for detection of the thoracic aortic lumen.

When the lumen is detected, a dilation is performed, enough to cover any potential aneurysms attached to the lumen.

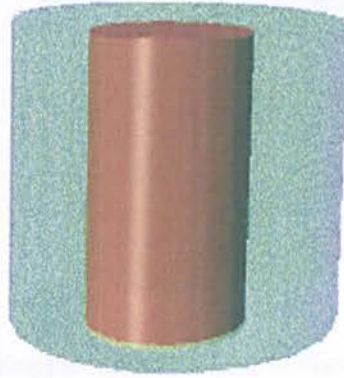


Figure 3.21: Schematic representing dilation of the aorta (in green we have the dilated aorta and in red the original aorta).

We investigate the potential aneurysms by thresholding the area between the dilated lumen and original lumen within a range of the aorta Hounsfield units to detect any potential aneurysms (10-70 Hounsfield units).

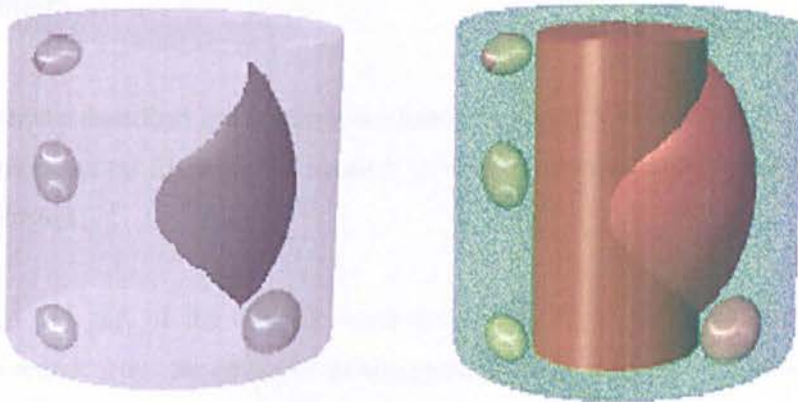


Figure 3.22: Schematic representing potential aneurysms.

Then a region labelling method is used to remove all isolated objects that have same unit value but are not attached to the lumen (removal of false positives).

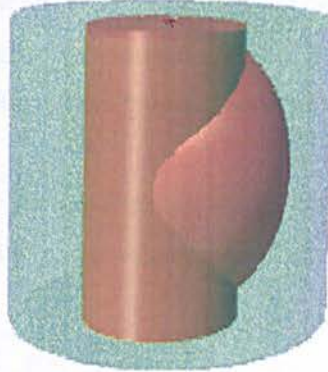


Figure 3.22: Schematic representing the removal of isolated objects with same Hounsfield unit to the aorta.

At the end of this process if any objects remain attached we consider it as being potential aneurysm. If there is no presence of aneurysm surrounding the lumen it is no longer necessary to perform CAM system. This will be further discussed in the next Chapter.

3.6. Summary

In this chapter we described the methods we have developed for the several stages outlined in our CAD component (as illustrated in figure 3.1), with the ultimate goal to detect the location of potential aneurysm.

As aneurysms are part of the thoracic aorta and are attached to it, the first step aimed to constrain the search scope for detection of aneurysm candidates by extraction the thoracic aorta and selection of slices which may include an aneurysm.

The algorithm developed started by automatically detecting the first seed point. For this a method was implemented which identifies where the celiac trunk is located and it is used as the first slice where the seed point is applied for the 3D region growing algorithm to segment the thoracic aortic lumen.

The region growing method works by selecting the x-y coordinates of a pixel and grows into a region depending on a certain predefined criteria. The criteria are that in the pixel

neighbourhood it will find the pixel with the highest intensity value and add it to the region and then update the boundary points. It calculates a measure of contrast of the region and records it. This process repeats until the region is expanded enough. The algorithm then finds the region with the highest average contrast during the growing processes.

After building the TA centreline we generate the reconstructed images (orthogonal plane to centre line) of the vessel that allows us to accurately detect the entire thoracic aorta with the potential aneurysm present.

Once again the region growing method was applied but this time on the reconstructed images, followed by a dilation, which gives us an area to search for loose connections with objects of similar intensity value such as the spine. Hence, it was necessary to use a method to eliminate them. A simple threshold technique using Hounsfield units of the TAA was applied and any detached objects that are considered to be false positives are removed, as well as any attached objects are considered to be potential aneurysms.

Therefore, in this Chapter the CAD component of our developed system has then been described where the thoracic aortic lumen has automatically been detected as well as any potential aneurysm. In the next Chapter we will describe the CAM component of our system.

These CAD components are needed for the possible generation of the final CAD model, and the segmentation and quantification of the TAA. The chapter includes a detailed description of each module of the CAM segmentation system.

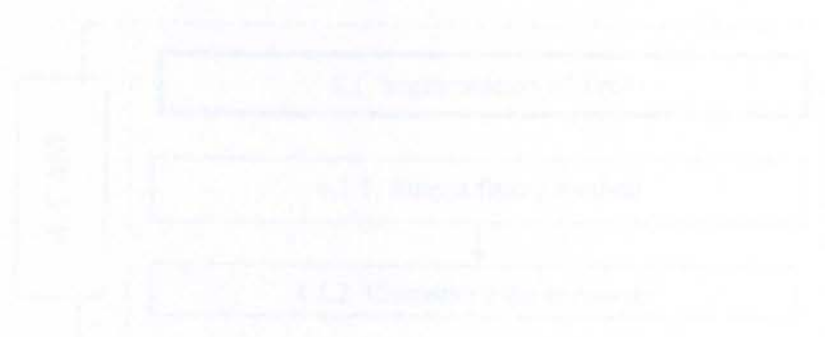


Figure 4.1: Block diagram of the proposed CAM system.

Chapter 4

Proposed CAM System

4.1. Segmentation of the thoracic cavity from chest X-ray image

In this chapter, we propose a new method for the segmentation of the thoracic cavity from chest X-ray images. The proposed method is based on the use of a deep learning-based approach, which is able to automatically segment the thoracic cavity from chest X-ray images.

The proposed method is based on the use of a deep learning-based approach, which is able to automatically segment the thoracic cavity from chest X-ray images. The proposed method is based on the use of a deep learning-based approach, which is able to automatically segment the thoracic cavity from chest X-ray images. The proposed method is based on the use of a deep learning-based approach, which is able to automatically segment the thoracic cavity from chest X-ray images.

Once CAD component has confirmed the potential presence of an aneurysm, the next step will be segmentation and quantification of the TAA. This chapter provides a detailed description of each stage of the CAM component of our system.

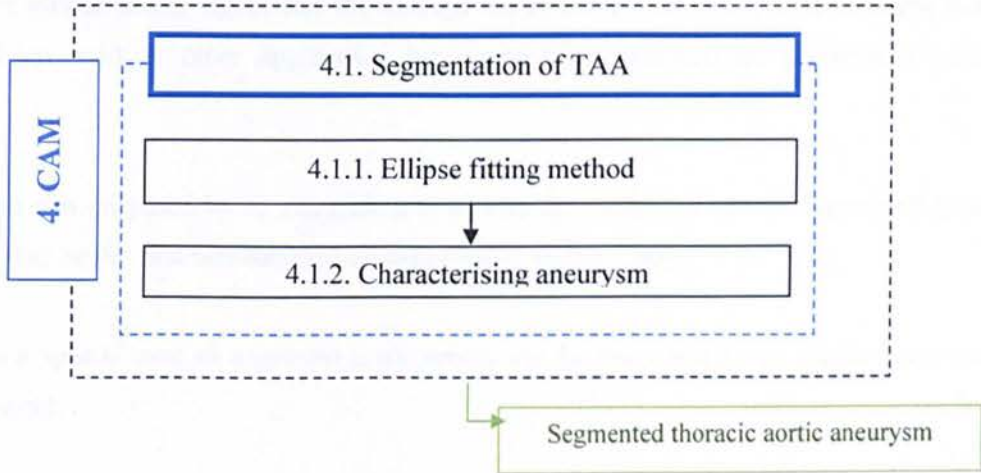


Figure 4.1: Illustration of CAM system

Segmentation of an aneurysm is a prerequisite for the volume measurement and shape characterization of the aneurysm. The proposed segmentation method is a multi-stage process as outlined in the system illustrated in figure 4.1.

4.1. Segmentation of the thoracic aorta (aortic aneurysms)

Previously in Chapter 3 section 3.5., we have removed all isolated objects that had same Hounsfield units, (61 Hounsfield units) value as the thoracic aorta but are not attached to the lumen.

As we know, in reconstructed images the thoracic aorta takes a shape of an ellipse. In this section we use the previously segmented thoracic aorta contour points to apply an ellipse fitting method to properly remove any attached tissue that does not belong to the TAA. Therefore, with this method we will be able to detach the tissue, such as muscle, that would still be attached to the thoracic aorta as it has the same Hounsfield units, (10-70 Hounsfield units).

4.1.1. Ellipse fitting method

Among other ellipse fitting algorithms the method we chose to use in our CAM system has previously been used in other application but never been explored its potential in real application.

This approach was proposed by A. Fitzgibbon *et al.* and the method works on segmented data and it is stated to be the first non-iterative ellipse-specific fitting [106].

An ellipse is a special case of a general conic which can be described by an implicit second order polynomial:

$$F(x, y) = ax^2 + bxy + cy^2 + dx + ey + f = 0 \quad (4.1)$$

With an ellipse-specific constraint:

$$b^2 - 4ac < 0 \quad (4.2)$$

Where a,b,c,d,e,f are coefficients of the ellipse and (x,y) are coordinates of the points lying on it. The polynomial F(x,y) is called the algebraic distance of the point(x,y) to the given conic. By introducing vectors:

$$a = [a, b, c, d, e, f]^T \quad (4.3)$$

$$b = [x^2, xy, y^2, x, y, 1]$$

it can be rewritten to the vector form:

$$F_a(x) = x \cdot a = 0 \quad (4.4)$$

The fitting of a general conic to an aneurysm contour point (x_i, y_i) , $i = 1 \dots N$ may be approached by minimizing the sum of squared algebraic distance of the points to the conic which is represented by coefficients \mathbf{a} :

$$\begin{aligned} \min_{\mathbf{a}} \sum_{i=1}^N F(x_i, y_i)^2 &= \min_{\mathbf{a}} \sum_{i=1}^N (F_{\mathbf{a}}(x_i))^2 \\ &= \min_{\mathbf{a}} \sum_{i=1}^N (x_i \cdot \mathbf{a})^2 \end{aligned} \quad (4.5)$$

The problem Equation 4.5 can be solved directly by the standard least squares approach, but the result of such fitting is a general conic and it does not need to be an ellipse.

To ensure an ellipse-specificity of the solution, the appropriate constraint equation 4.2 has to be considered. In A. Fitzgibbon *et al.* paper it was shown that such system is hard to solve in general [106]. However, because $\alpha \cdot \mathbf{a}$ represents the same conics as \mathbf{a} for any $\alpha \neq 0$, we have a freedom to arbitrarily scale the coefficients \mathbf{a} . Under a proper scaling, the inequality constraint equation 4.2 can be changed into an equality constraint:

$$4ac - b^2 = 1 \quad (4.6)$$

And the ellipse-specific fitting problem can be reformulated as:

$$\min_{\mathbf{a}} \|\mathbf{D}\mathbf{a}\|^2 \quad \text{subject to} \quad \mathbf{a}^T \mathbf{C} \mathbf{a} = 1 \quad (4.7)$$

Where the design matrix \mathbf{D} ,

$$\mathbf{D} = \begin{pmatrix} x_1^2 & x_1 y_1 & y_1^2 & x_1 & y_1 & 1 \\ x_i^2 & x_i y_i & y_i^2 & x_i & y_i & 1 \\ x_N^2 & x_N y_N & y_N^2 & x_N & y_N & 1 \end{pmatrix} \quad (4.8)$$

represents the least squares minimization equation 4.5 and the constraint matrix \mathbf{C} of the size 6×6 ,

$$C = \begin{pmatrix} 0 & 0 & 2 & 0 & 0 & 0 \\ 0 & -1 & 0 & 0 & 0 & 0 \\ 2 & 0 & 0 & 0 & 0 & 0 \\ 0 & 0 & 0 & 0 & 0 & 0 \\ 0 & 0 & 0 & 0 & 0 & 0 \\ 0 & 0 & 0 & 0 & 0 & 0 \end{pmatrix} \quad (4.9)$$

Express the constraint equation 4.6. The minimization problem equation 4.7 is ready to be solved by a quadratically constrained least squares minimization as proposed in Grande *et al.* First, by applying the Lagrange multipliers we get the following conditions for optimal solution **a** [107].

$$\begin{aligned} Sa &= \lambda Ca \\ a^T Ca &= 1 \end{aligned} \quad (4.10)$$

Where S is the scatter matrix of the size 6x6,

$$\begin{aligned} S &= D^T D \\ &= \begin{pmatrix} S_{x^4} & S_{x^3y} & S_{x^2y^2} & S_{x^3} & S_{x^2y} & S_{x^2} \\ S_{x^3y} & S_{x^2y^2} & S_{xy^3} & S_{x^2y} & S_{xy^2} & S_{xy} \\ S_{x^2y^2} & S_{xy^3} & S_{y^4} & S_{xy^2} & S_{y^3} & S_{y^2} \\ S_{x^3} & S_{x^2y} & S_{xy^2} & S_{x^2} & S_{xy} & S_x \\ S_{x^2y} & S_{xy^2} & S_{y^3} & S_{xy} & S_{y^2} & S_y \\ S_{x^2} & S_{xy} & S_{y^2} & S_x & S_y & S_1 \end{pmatrix} \end{aligned} \quad (4.11)$$

In which the operator S denotes the sum

$$S_{x^a y^b} = \sum_{i=1}^N x_i^a y_i^b \quad (4.12)$$

Next, the system equation 4.10 is solved by using generalized eigenvectors. There exist up to six real solutions (λ_j, a_j) , but because

$$\|Da\|^2 = a^T D^T D a = a^T S a = \lambda a^T C a = \lambda \quad (4.13)$$

We are looking for the eigenvector a_k corresponding to the minimal positive eigenvalue λ_k . Finally, after a proper scaling ensuring $a_k^T C a_k = 1$, we get a solution of the minimization problem equation 4.7 which represents the best fit ellipse for the given contour points of the aneurysm.

Based on this derivation, A. Fitzgibbon *et al.* proposed an effective and robust algorithm for an ellipse specific fitting of data points.

Apart from its theoretical correctness, the original approach described in the previous section has several drawbacks. The matrix C (equation 4.9) is singular and the matrix S (equation 4.11) is also nearly singular (it is singular if all data points lie exactly on an ellipse). Regarding that, the computation of the eigenvalues of equation 4.10 is numerically unstable and can produce wrong results (as infinite or complex numbers).

Another problematic part of the algorithm is a localization of the optimal solution of the fitting. In A. Fitzgibbon *et al.*, authors proved that equation 4.10 has exactly one positive eigenvalue and they stated that the corresponding eigenvector is an optimal solution of equation 4.7. Unfortunately, this is not true. In an ideal case, when all the data points lie exactly on an ellipse, the eigenvalue is zero. Moreover, regarding a numerical computation of eigenvalues the optimal eigenvalue can be a small negative number. In such situations, the proposed localization can produce non-optimal or completely wrong solutions.

To overcome the drawbacks of the original approach, we should follow on a theoretical analysis of equation 4.10. Both matrices S (equation 4.11) and C (equation 4.9) have special structures which allow a simplification of the problem of finding the eigenvalues. First, we decompose the design matrix D (equation 4.8) into its quadratic and linear parts:

$$D = (D_1 | D_2) \quad (4.14)$$

Where,

$$D_1 = \begin{pmatrix} x_1^2 & x_1 y_1 & y_1^2 \\ x_i^2 & x_i y_i & y_i^2 \\ x_N^2 & x_N y_N & y_N^2 \end{pmatrix} \quad (4.15)$$

and

$$D_2 = \begin{pmatrix} x_1 & y_1 & 1 \\ x_i & y_i & 1 \\ x_N & y_N & 1 \end{pmatrix} \quad (4.16)$$

Next, the scatter matrix S (equation 4.11) can be split as follows:

$$S = \left(\begin{array}{c|c} S_1 & S_2 \\ \hline S_2^T & S_3 \end{array} \right) \quad \text{where} \quad \begin{aligned} S_1 &= D_1^T D_1 \\ S_2 &= D_1^T D_2 \\ S_3 &= D_2^T D_2 \end{aligned} \quad (4.17)$$

Similarly, the constraint matrix C (equation 4.9) can be expressed as:

$$C = \left(\begin{array}{c|c} C_1 & 0 \\ \hline 0 & 0 \end{array} \right) \quad \text{where} \quad C_1 = \begin{pmatrix} 0 & 0 & 2 \\ 0 & -1 & 0 \\ 2 & 0 & 0 \end{pmatrix} \quad (4.18)$$

Finally, we split the vector of coefficients a (equation 4.3) into:

$$a = \begin{pmatrix} a_1 \\ a_2 \end{pmatrix} \quad \text{where} \quad a_1 = \begin{pmatrix} a \\ b \\ c \end{pmatrix} \quad \text{and} \quad a_2 = \begin{pmatrix} d \\ e \\ f \end{pmatrix} \quad (4.19)$$

Based on these decompositions, the first condition of equation 4.10 can be rewritten as:

$$S = \left(\begin{array}{c|c} S_1 & S_2 \\ \hline S_2^T & S_3 \end{array} \right) \cdot \begin{pmatrix} a_1 \\ a_2 \end{pmatrix} = \lambda \cdot \left(\begin{array}{c|c} C_q & 0 \\ \hline 0 & 0 \end{array} \right) \cdot \begin{pmatrix} a_1 \\ a_2 \end{pmatrix} \quad (4.20)$$

Which is equivalent to the following two equations:

$$S_1 a_1 + S_2 a_2 = \lambda C_1 a_1 \quad (4.21)$$

$$S_2^T a_1 + S_3 a_2 = 0 \quad (4.22)$$

The matrix S_3 :

$$S_3 = D_2^T D_2 = \begin{pmatrix} S_{x^2} & S_{xy} & S_x \\ S_{xy} & S_{y^2} & S_y \\ S_x & S_y & S_1 \end{pmatrix} \quad (4.23)$$

is exactly a scatter matrix of the task of a fitting a line through the contour points. It is known that this matrix is singular only if all the points lie on a line. In such situations there is no real solution of the task of a fitting an ellipse through these points [108].

In all other cases the matrix S_3 is regular. Regarding that, a_2 can be expressed from equation 4.22 as:

$$a_2 = -S_3^{-1} S_2^T a_1 \quad (4.24)$$

Including equation 4.24 into equation 4.21 yields:

$$(S_1 - S_2 S_3^{-1} S_2^T) a_1 = \lambda C_1 a_1 \quad (4.25)$$

Matrix C_1 (equation 4.18) is regular, thus equation 4.25 can be rewritten as:

$$C_1^{-1} (S_1 - S_2 S_3^{-1} S_2^T) a_1 = \lambda a_1 \quad (4.26)$$

The second condition of equation 4.10 can also be reformulated by using the decomposition principle. Due to the special shape matrix C (equation 4.18) we simply get:

$$a_1^T C_1 a_1 = 1 \quad (4.27)$$

Regarding all the decomposition steps (equation 4.14-4.27), the conditions equation 4.10 can be finally expressed as the following set of equations:

$$\begin{aligned} Ma_1 &= \lambda a_1 \\ a_1^T C_1 a_1 &= 1 \\ a_2 &= -S_3^{-1} S_2^T a_1 \\ a &= \begin{pmatrix} a_1 \\ a_2 \end{pmatrix} \end{aligned} \quad (4.28)$$

Where M is the reduced scatter matrix of the size 3×3 ,

$$M = C_1^{-1} (S_1 - S_2 S_3^{-1} S_2^T) \quad (4.29)$$

Now we return to the task of fitting an ellipse through the contour points of the aneurysm detected in the previous chapter. As we saw before, the task can be expressed as the constrained minimization problem (equation 4.7), whose optimal solution corresponds to the eigenvector a of equation 4.10, which yields a minimal non negative value λ . Equation 4.10 is equivalent with equation 4.28, which is enough to find appropriate eigenvector a_1 of the matrix M .

The improved fitting algorithm proposed previously was implemented in the same straightforward way as the original method. Two tricks which improve numerical stability of the computation are used. First, due to the special structure of the matrix C_1 (equation 4.9) the pre multiplication by C_1^{-1} as requested in equation 4.29 is done directly.

The second trick gets rid of the problem of the localization of the minimal non-negative eigenvalue of the reduced scatter matrix M . The matrix has three real eigenvalues, typically two negative and one positive.

Unfortunately, we cannot simply find the positive eigenvalue. When M is close to a singular matrix, the optimal value can be zero or even a small negative number. Instead of the localization of such as eigenvalue, we evaluate the condition equation 4.27 for all eigenvectors

of the Matrix M . It can be proven that there exists only one eigenvector which gives a positive value - the one which corresponds to the optimal solution of TAA.

That eigenvector is localized and finally, the rest of the ellipse coefficients are computed and the complete solution provided.

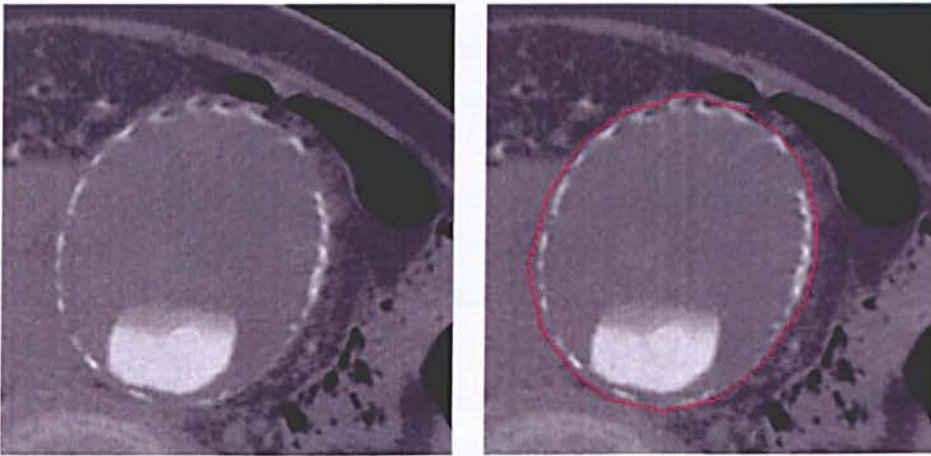


Figure 4.2: TAA detection using ellipse fitting.

In figure 4.3, we can visualize that the ellipse fitting method was useful to detach some of the muscle attached to the aorta as a result from our initial segmentation in section 3.4. In CAD component the resulting detection of the TAA incorrectly included some of the muscle tissue attached to the thoracic aorta as they have the same range of Hounsfield unit.

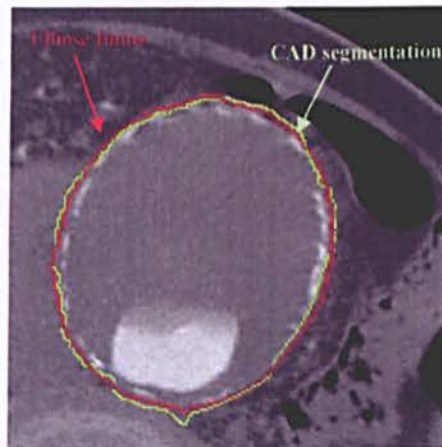


Figure 4.3: TAA segmentation using ellipse fitting (red colour) and CAD segmentation result (green colour).

Now that the TAA have been segmented using the ellipse fitting method we are able to characterize aneurysm.

4.2. Characterization Aneurysm

Once we have a fine segmentation of the aneurysm, it can be characterized by extracting different features of the aneurysm such as volume, maximum diameter etc.

Measurements such as diameter and length of the aorta can be characterized straightforwardly by using the eigenvectors (\mathbf{a}) and eigenvalues (λ) of the counter points obtained from our ellipse fitting method previously described in section 4.1.1.

Using the previously calculated eigenvalues (λ) and eigenvectors (\mathbf{a}) in the previous section, we are able to determine the eccentricity of the aneurysm (how elongated it is) by looking at the ratio of the eigenvalues, and we can determine the direction of elongation by using the direction of the eigenvector with whom's corresponding eigenvalue has the largest absolute value.

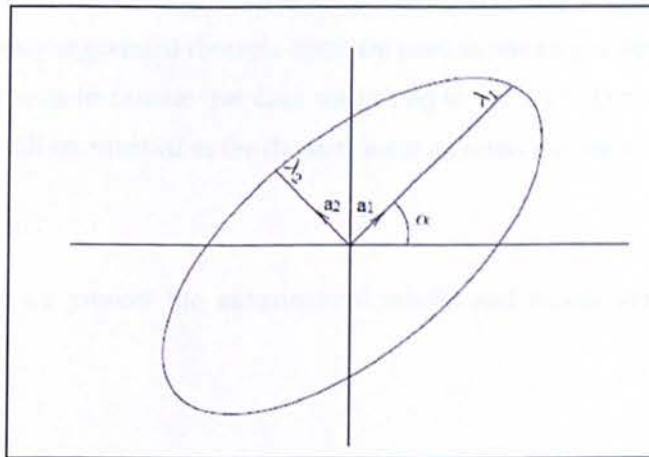


Figure 4.4: Ellipse diameter calculation.

To compute the volume of the aneurysm, the number of voxels of the segmented aneurysm is computed. The volume of each voxel is computed based on the voxel spacing extracted from the

DICOM header of the CTA scan, where we are able to access information such as; x-spacing, y-spacing and slice thickness.

We can compute the volume of a voxel using the following equation:

$$\text{Volume of voxel} = x\text{-spacing} * y\text{-spacing} * \text{slice-thickness}.$$

The volume of the aneurysm is then computed as such:

$$\text{Volume of the aneurysm} = \text{number of voxels of aneurysm} * \text{volume of voxel}.$$

Knowledge of aneurysm size, location and morphology will prove invaluable for a physician to be able to monitor the development of a potential fatal TAA. It will also prove essential in predicting and planning whether intervention is justified, and if so which intervention to choose and how to perform it. In addition, to predict stability of the aortic stent over time.

4.3. Summary

In this chapter we used the reconstructed images generated previously in chapter 3. The contour points of the previously segmented thoracic aorta are used in our ellipse fitting method to properly remove any attached tissue that does not belong to the TAA. Detaching tissue, such as muscle, that would still be attached to the thoracic aorta as it has the same Hounsfield units, (61 Hounsfield units).

In the next chapter we present the experimental results and assess the performance of the proposed system.

Chapter 5

Experimental Results and Validation

(CAD & CAM)

As discussed in chapters 3 and 4 we have developed a CAD/CAM system for detection and segmentation of thoracic aortic aneurysms. In this chapter we will evaluate and validate the main steps of our CAD and CAM components.

As described in our methodology, our CAD component has several stages to detect potential aneurysm in the CTA datasets. One of our main priorities was to be able to make our system free of manual interaction. Therefore, we start section 5.2.1 by evaluating the method for first seed point detection to be able to apply a region growing algorithm for segmentation of the thoracic aortic lumen. Following the detection of the thoracic aortic lumen, we present the detection of the centreline of the thoracic aorta that will enable us to generate orthogonal slices (reconstructed images). These reconstructed images allow us to implement our thoracic aortic aneurysm detection algorithm. We finish section 5.2.1 by validating the results of our CAD component.

In section 5.2.2 we present the results of our segmentation of the thoracic aortic aneurysms and evaluate it against another method to prove we have chosen the most accurate and time efficient method. Finally, we validate our CAM component results by comparing our automatic segmentation of the TAA against the radiologist manual segmentation.

For the radiologist to be able to manually annotate the CTA datasets and so we could compare it with our automated CAD/CAM system a Medical Images Processing, Seamless and Secure Sharing Platform (MIPS³), has been developed using .NET (as illustrated in Figure 5.1). Not only is it useful for the annotation of ROI of TAA but also a great prototype to demonstrate our program.

MIPS³ loads DICOM image dataset, runs the CAD and CAM system (automatically) and saves the detected ROI. The annotation is then used to compare CAD/CAM system against the radiologist's manual annotations, as we use the radiologist manual segmentation as a gold standard. MIPS³ is also useful used to measure the number of false positives and true negatives.

As MIPS³ is such an essential tool to evaluate any other CAD/CAM systems, we will dedicate section 5.1 to describe more in detail some of its most important features.

5.1. MIPS³

A customized image software platform, MIPS³, has been developed using .NET for the annotation of ROI of TA as well as being a prototype to develop and demonstrate CAD systems. Figure 5.1 demonstrates the MIPS³ application diagram.

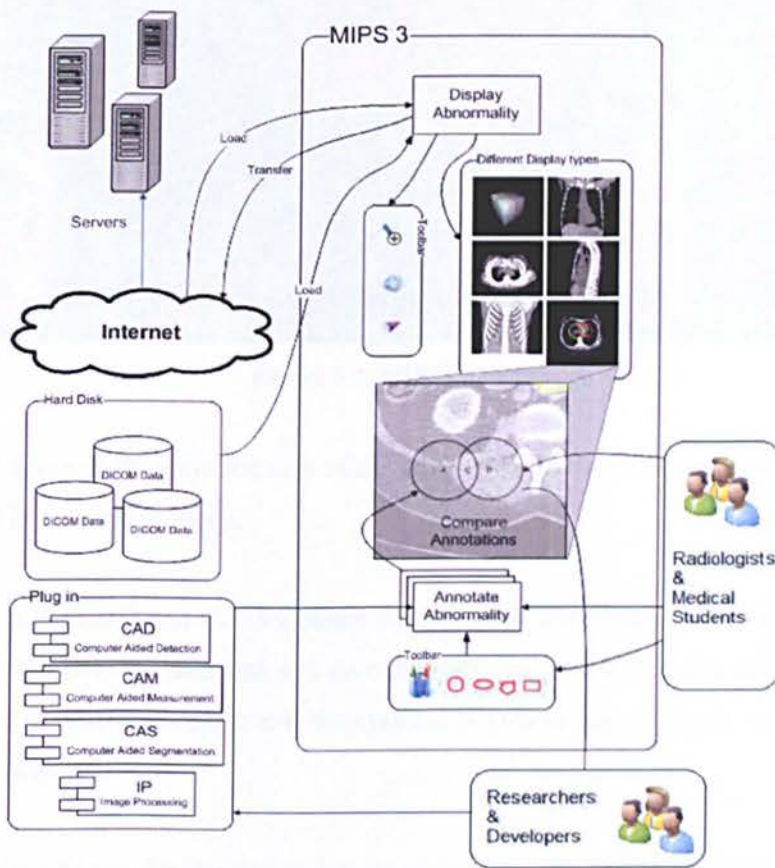


Figure 5.1: Diagram of MIPS³ application.

Some of the main functions of MIPS³ include: loading DICOM data sets, visualization tool (sagittal, axial, coronal view, zoom, etc.), annotation tool of region of interest (ROI), facility to plug image processing algorithms such as CAD and CAM, detecting false positives and false negatives using two sets of annotated data and generates ROC curve, and provides a safe platform for developers and radiologists to share medical images and annotations.

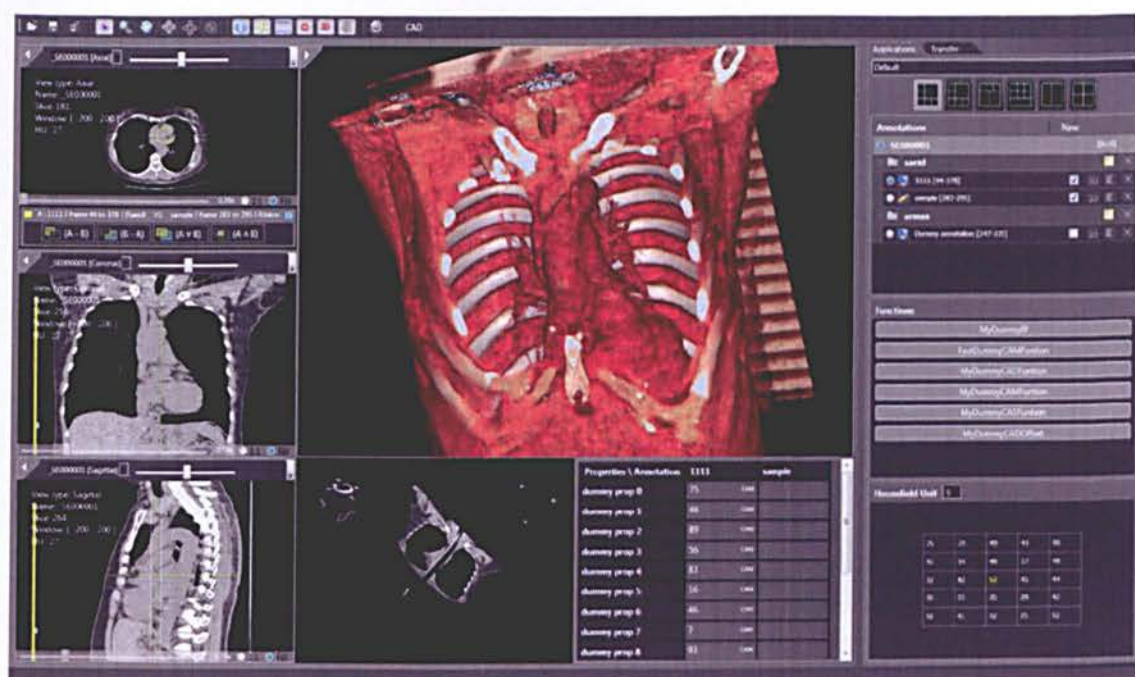


Figure 5.2: MIPS3 platform.

These are just some of the main features of our developed platform. We will be discussing them in more detail in the next sections.

MIPS3 plugs in the CAD and CAM systems developed in our research then automatically runs the routines in the DICOM data sets and save the resulting annotation. The radiologist can then upload his/hers manual annotation and the systems is able to highlight any true/false positives and true/false negatives.

For the radiologist to use the annotation feature of the developed platform MIPS3 he/she simply needs to click the annotation button in the toolbar as shown in Figure 5.2 and it will automatically switch to annotation mode.

When the radiologist chooses to start a new annotation, the system automatically loads the annotation window, as in figure 5.3, and adds a new annotation object to the DICOM data. It has features such as loading and saving the changes done, and the data will be overlaid on the image when it is rendering in the viewer.

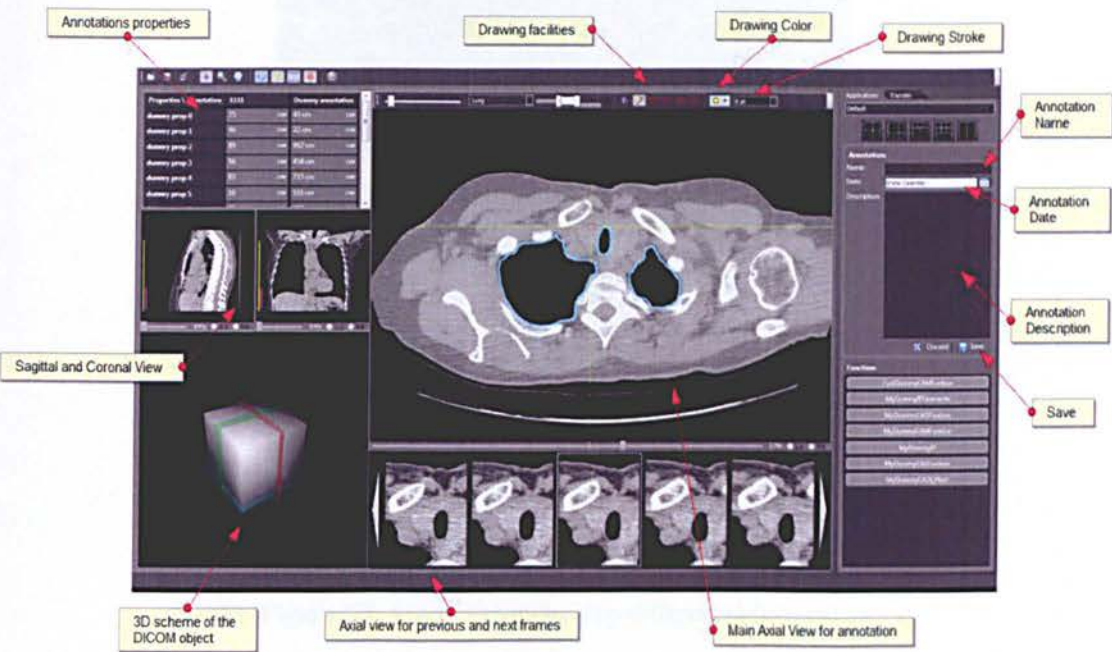


Figure 5.3: Annotation window.

If the radiologist chooses to open previously saved annotation, the system will load the annotation list as represented below in figure 5.4.

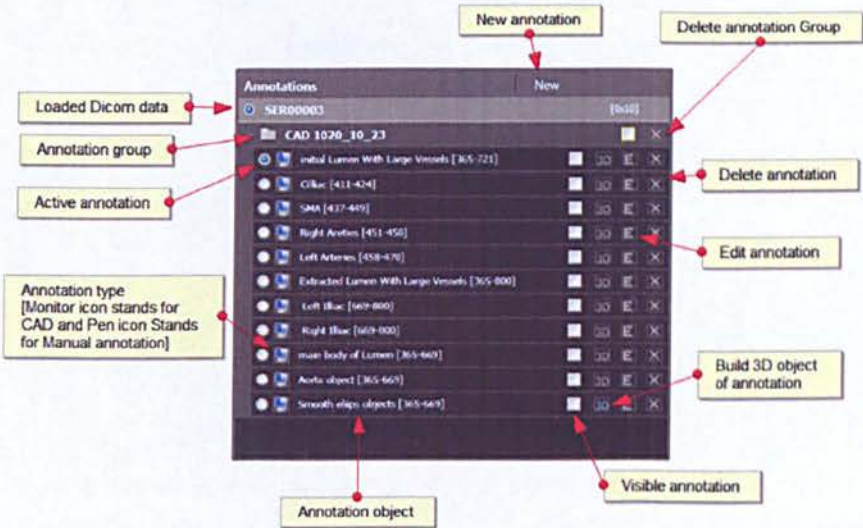


Figure 5.4: Annotation list.

One of the essential features of our MIPS3 system is that for the diagnosing of data sets, different radiologists can save their annotations and a list will be created as can be seen in figure 5.5.



Figure 5.5: List of annotations by different radiologists.

If two annotations are selected two different annotations are displayed as shown below in figure 5.6.

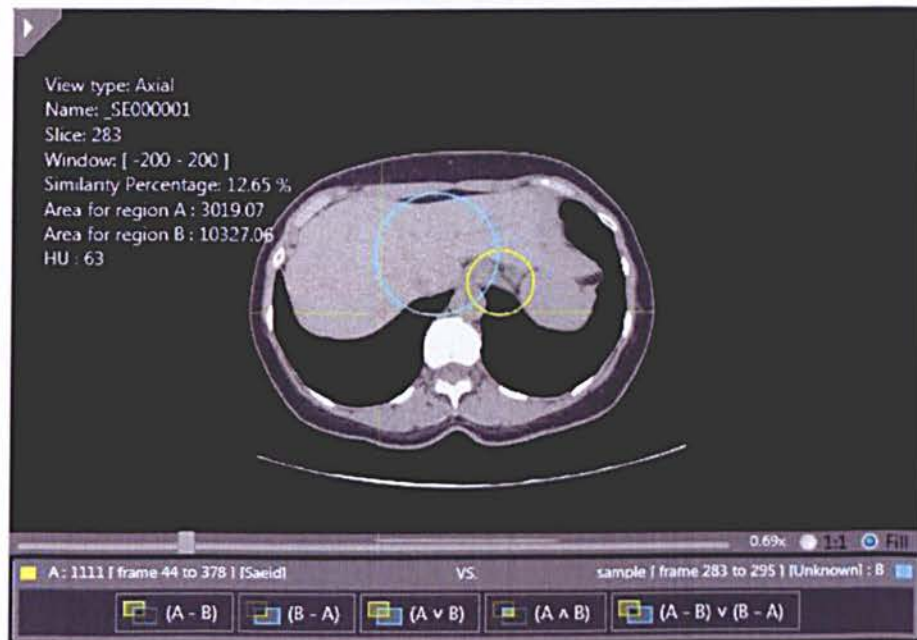


Figure 5.6: Two annotations selected.

In addition to the main features referred above, there are several other useful features such as inter and intra observability measurements which are worth mentioning, although it has not been utilised in our study.

As humans are susceptible to committing errors, their analysis is usually subjective due to the inter and intra observer variability issue. Therefore, being able to visualise in the platform the different annotations of different radiologist leads to a more accurate diagnostic decision by the physician.

Different radiologists may well interpret data differently due to their work experience. For example, the inter observer variability involves the difficulty the radiologist may have to find the exact border of abnormalities in the CT scan being inspected, but there is also the intra observer variability where the radiologist may identify regions differently even when analysing the same data different times, sometimes due to simple shaking action of the hands when delineating the borders of the abnormality in the computer.

Dehmeshki *et al.*, in 2006 conducted a study to prove inter and intra observer variability. In the study, three radiologists analysed 42 datasets where there was a difference in slice thickness that varied from high to low resolution with an average of 180 slices per dataset. Each radiologist were independently asked to locate the nodules present in the datasets scans and as below in figure 5.7 we can observe the large number of inter and intra observer variability. [109]

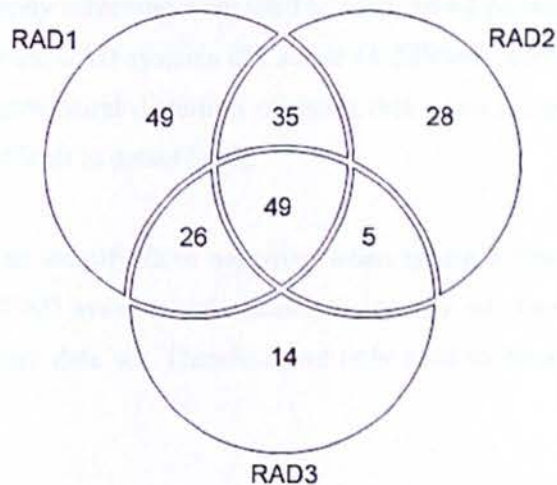


Figure 5.7: Diagram illustrating intra and inter observer variability between three radiologists.

Our developed system will therefore be a vital tool to help the radiologist with the vast amount of data one needs to analyse for each dataset and hopefully speed the process and make it more accurate. But as we know humans are error prone. Radiologist diagnosis is based on subjective judgement and is therefore prone to error. Hence the radiologists might for example identify a false positive or false negative due to the difference in their work experience.

In most CAD systems such as colon, lung or mammography, where many polyps or nodules are present in each data set, the identification of false positives and false negatives is paramount.

A false positive is when for example the CAD system detects several nodules that are later discarded by a physician after closer inspection. If we take for example the case of lung nodules where they are always in large amounts present in the data sets they can easily be confused with normal tissue. The CAD system is usually good at identifying what it seems to be abnormal tissue and detecting as nodules, then after it is the radiologist's job to detect the false positives and eliminate them from the diagnosis.

False negative represents when for example a breast cancer tissue is not detected by the CAD systems. If we take for example the work discussed in J. Baker *et al.* in 2003, where two CAD systems for mammography screening were used to analysed 43 patient datasets. They were able to identify the fact that the CAD systems did detect 45 different lesions in the mammography's but failed to detect architectural distortion of tissue that takes the appearance of overlapping tissue therefore very difficult to detect [110].

Hence they were able to identify false negatives when taking a closer look. Unlike the cases discussed above, our CAD systems only needs to identify whether there is presence of an aneurysm for each patient data set. Therefore, we only need to detect false positives and true negatives.

In this project we were able to use the annotation features of our MIPS3 program to identify any false positives and true negatives. In figure 5.8 for example, we can see in the figure bottom part that when two annotations are detected by the system (one from our algorithm and another by a radiologist manual annotation), a percentage text box and VS will appear. If the radiologist clicks the VS button will compare the two annotations.

Therefore, the false positives and true negatives are identified based on the comparison via tolerance of the given percentage.

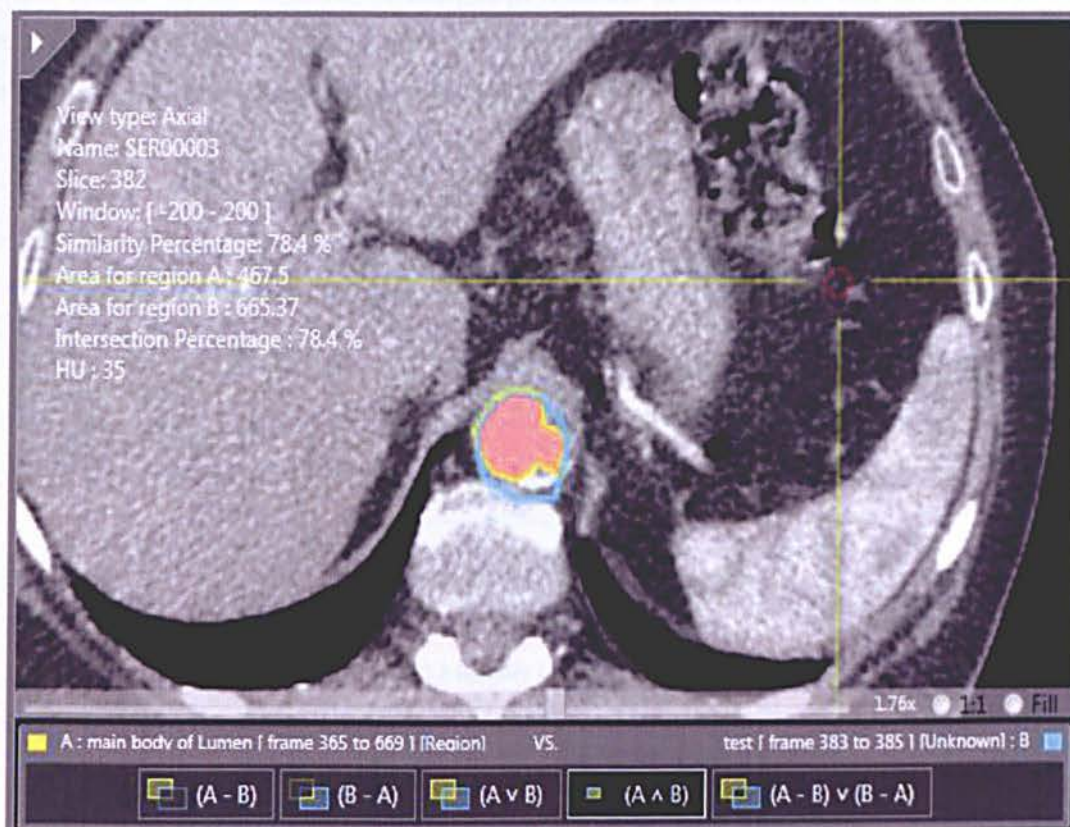
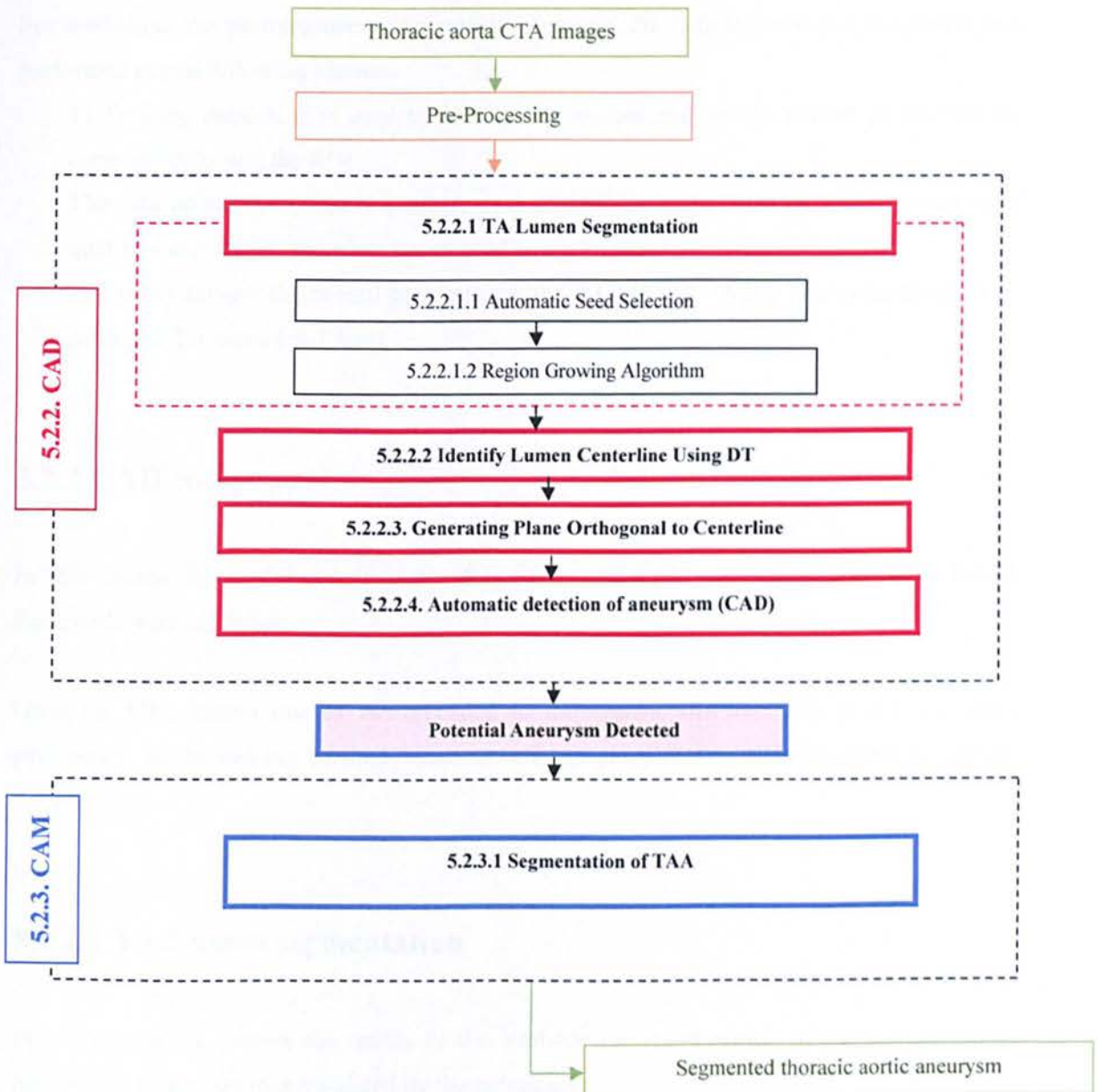


Figure 5.8: Annotations of three different segmentations, two manual one automatic by our system.

Our developed systems will therefore, be a vital tool to help the radiologist with the vast amount of data one needs to analyse for each dataset and hopefully speed the process and make it more accurate.

5.2. Evaluation of CAD and CAM performance

In this section we will evaluate the main steps from our proposed CAD and CAM components, which have been previously described in detail in our methodology, Chapter 3 and 4. We will follow the same steps as illustrated in the diagram.



5.2.1 Data Acquisition

To evaluate and validate our CAD/CAM system we use data provided by Lausanne Hospital that was all scanned with the same parameters (120kV, 749 mA, slice thickness 0.6 mm and the total number of slices for each scan varied from 300 to 400 with an average of 350 per scan).

For evaluating the performance using patient's datasets, the radiologist visual judgement was performed in two following phases:

- 1) Training dataset: It is used to develop the system and set the correct parameters for correctly detecting the ROI.

The data set has been used to evaluate each step of CAD and CAM by visual inspection of qualified radiologist, therefore it was used as a gold standard.

- 2) Testing dataset: the overall performance of the CAD and CAM system was tested on 30 patients CTA scans (real data).

5.2.2 CAD component

In this section some of the main steps of our proposed CAD component will be evaluated. Followed by its validation.

Once the CTA dicom images are uploaded to the system, the first step of our algorithm performs a pre-processing method based on anisotropic diffusion filtering (refer to section 2.3.1.1.3.).

5.2.2.1 TA Lumen segmentation

In this section we present the results of the methods for segmentation of the thoracic aortic lumen. Our results are then validated by the radiologist

5.2.2.1.1 Automatic Seed selection

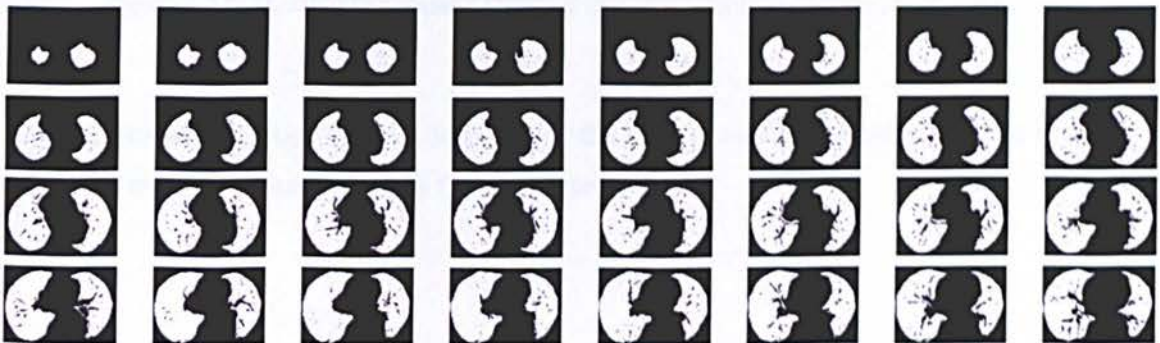
As previously described in our methodology, Chapter 3, the CAD component of our system automatically starts by detecting a first seed point by locating the celiac trunk.

The process begins by locating the end of the lungs. In figure 5.10 we can see an example of the segmented lung in a CT scan illustrated in blue colour using the MIPS3 window for visualisation that is used to detect the end of the lung.



Figure 5.10: Lung segmentation.

Once the segmentation of the lung has been performed we can then identify the slice with end of the lungs.



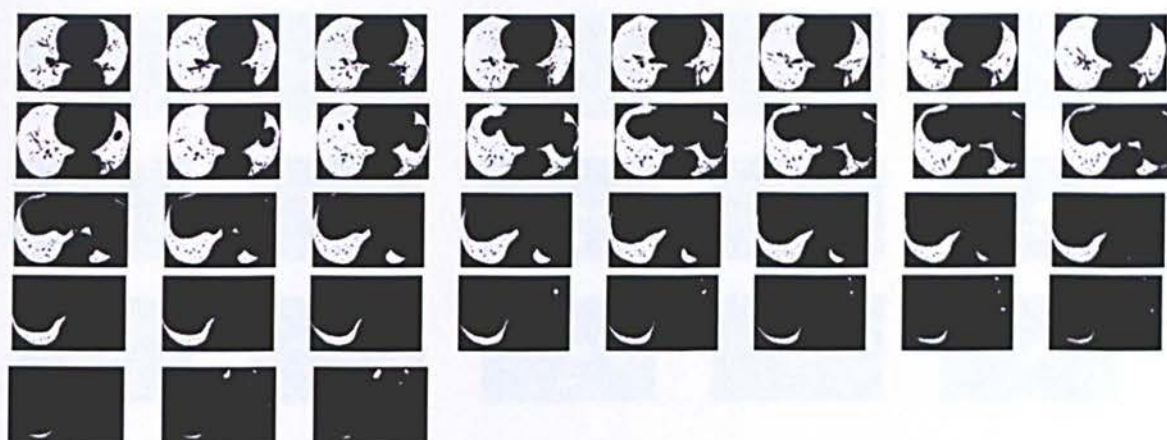


Figure 5.11: End of lung slice detection.

Once we detect the lungs we identify the last slice where the lung is present and use that slice as the starting point to locate the lumen, consequently the seed point. For this we use a thresholding method followed by a shape analysis (degree of circularity). An example can be seen in figure 5.12.

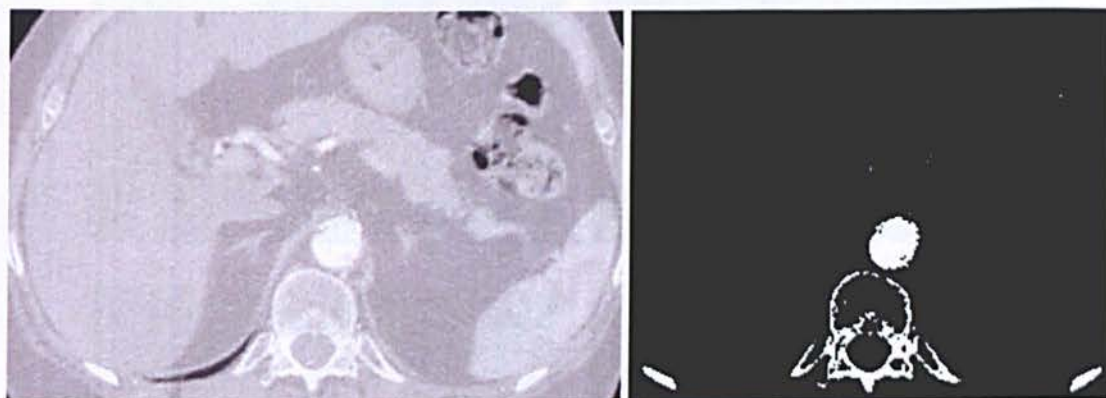


Figure 5.12: Thresholding method followed by a shape analysis (degree of circularity).

However instead of using one slice to represent the lumen, we use 5 slices in order to separate the lumen from other tissues such as the spinal cord.

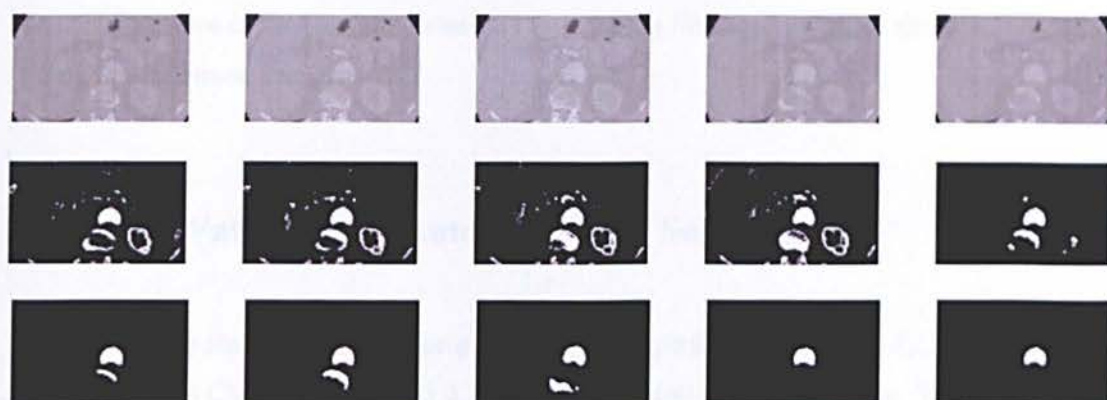


Figure 5.13: slice “box” for the detection of the thoracic aorta.

To make sure we have identified the correct object in the image we find within the previous 5 slice search the celiac trunk. By using contextual information, we know that the aorta is attached to the celiac trunk.

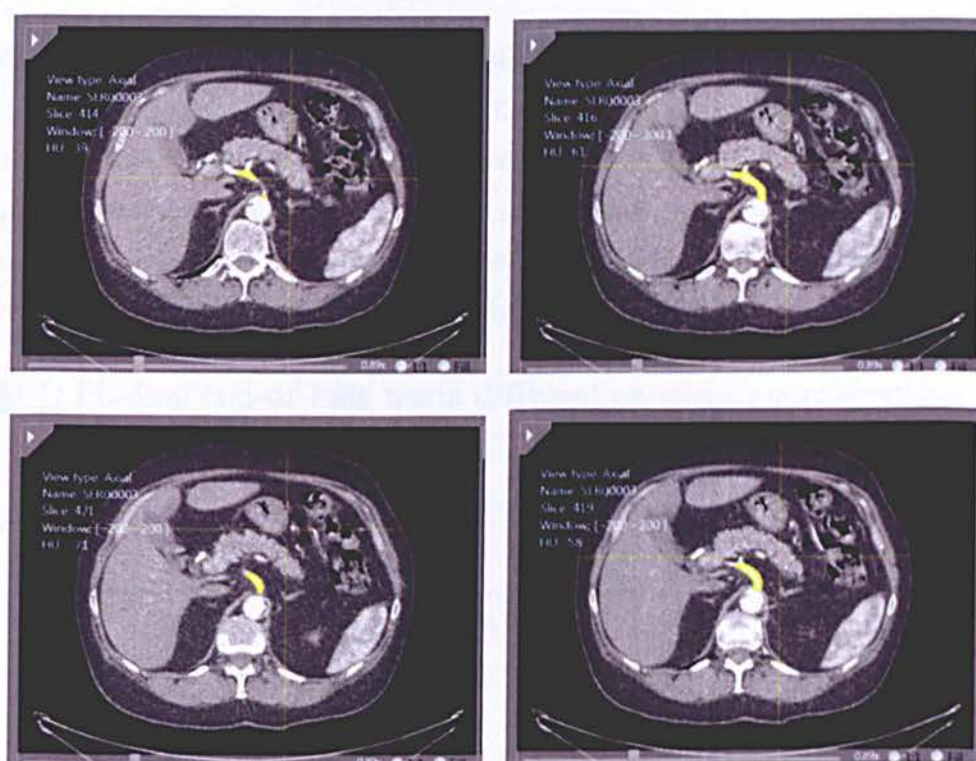


Figure 5.14 : Detection of the celiac trunk.

We use the centre of the partially detected lumen as the first seed point for the next stage of our system, entire lumen detection.

5.2.2.1.1 Validation of Automatic Seed Selection

We investigated the sensitivity of the algorithm to the parameters T_{size} and T_{cnt} in Equations 3.1 and 3.2 (refer to Chapter 3 section 3.2.1.1) to find the end-of-lung location. Table 1 shows the results of finding the end-of-lung positions using different parameters.

The minimum, maximum and average distance, in millimetres, of the 40 datasets between the end-of-lung location and the actual position of the Celiac Trunk are given. The latter location was provided by one of the radiologists.

The algorithm failed on one dataset when the size limit for identifying the isolated objects was small ($T_{size}=3$). This is because some of the artifacts from the segmented lung were identified as valid isolated objects. Apart from the choice of the small size limit, the algorithm was robust for a range of experimental values, but due to the space limitations, many of the combinations of the parameters are not shown in Table 1. Out of these results, the parameters of $T_{size}=6$, $T_{cnt}=6$ were chosen to optimize the trade-off between robustness and accuracy.

Table 1: Finding end-of-lung using different parameter combinations

Parameters	Min, Max distance to Celiac (mm)	Average distance to Celiac (mm)
$T_{size}=3, T_{cnt}=3$	-239, 80	35.6
$T_{size}=4, T_{cnt}=4$	-159, 80	33.9
$T_{size}=5, T_{cnt}=5$	-12, 80	30.8
$T_{size}=6, T_{cnt}=6$	-12, 80	31.69
$T_{size}=10, T_{cnt}=10$	-4, 100	44.7
$T_{size}=5, T_{cnt}=10$	-12, 80	33.7
$T_{size}=5, T_{cnt}=20$	6, 88	48.6

Figure 11 shows the distance between the end-of-lung location, obtained by the algorithm using the parameters $T_{size}=6$, $T_{cnt}=6$, and the actual location of the Celiac Trunk for the 30 CT scans.

As can be seen, in majority of the images the Celiac Trunk is located after the lung position found by the algorithm. From this result, it can be concluded that a safe search limit for finding the Celiac Trunk automatically is from 40 mm above and 120 mm below the end-of-lung position (see Section 3.1.1.).

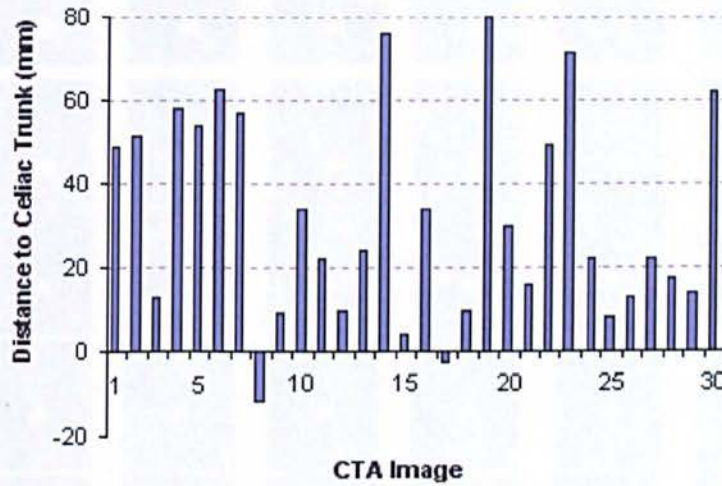


Figure 5.15: Distance between end-of-lung and the Celiac Trunk for 30 CTA images using the parameters $T_{size}=6$, $T_{cnt}=6$. The x-axis indicates the 40 CTA images and the y-axis denotes the distance between the obtained end-of-lung and the actual Celiac Trunk locations.

5. 2.2.1.2 Region growing algorithm

Once the seed point has been successfully detected, the automated 3D contrast based region growing method is applied. As we can see in figure 5.14, we have the first slice used as seed point for the region growing algorithm.

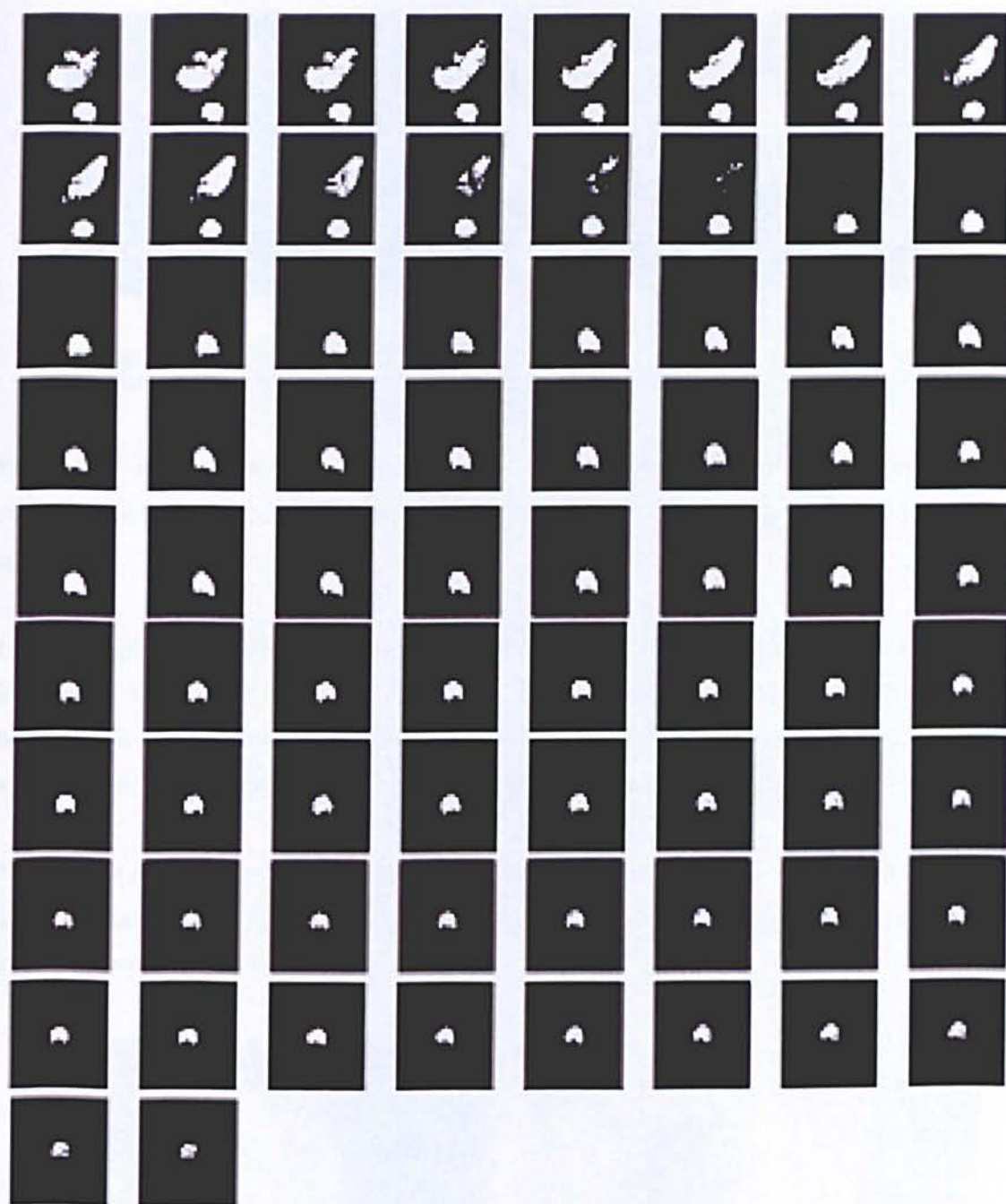


Figure 5.16: Region growing segmentation.

As can be seen in figure 5.16, there are surrounding organs and vessels such as the superior vena cava or the pulmonary artery still attached due to its similar intensities. It is therefore, necessary to detach those objects from the lumen.

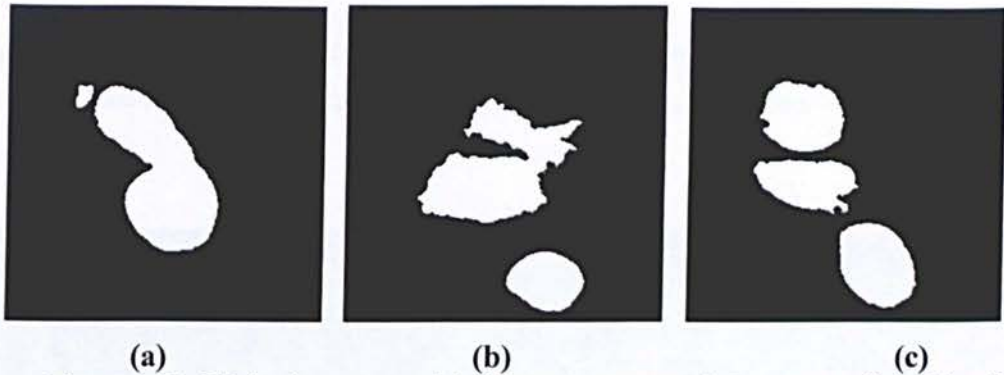


Figure 5.17: Elimination process with different parameters (a) Remove smallest object if less than $\frac{3}{4}$ of largest object (b) Remove largest object if twice the size of small object (c) If three objects present in one slice remove middle object.

Figure 5.17 demonstrates the vulnerability of the region growing methods when the anatomical structures to be segmented do not have a homogeneous statistical distribution over the image space.

Using contextual information we have the necessary knowledge to know that the object in such location, as for example, in figure 5.17(c) we have the superior cava in between the ascending aorta and descending aorta. Figure 5.17 (a) show us the right subclavian artery that in 3D is attached to the thoracic aorta. These different objects are analysed and removed in 2D slices.

There are also often some loose connections with objects of similar intensity value such as the spine, as can be seen in figure 5.18 below, which we call bleeding, once again we use contextual information to separate them.

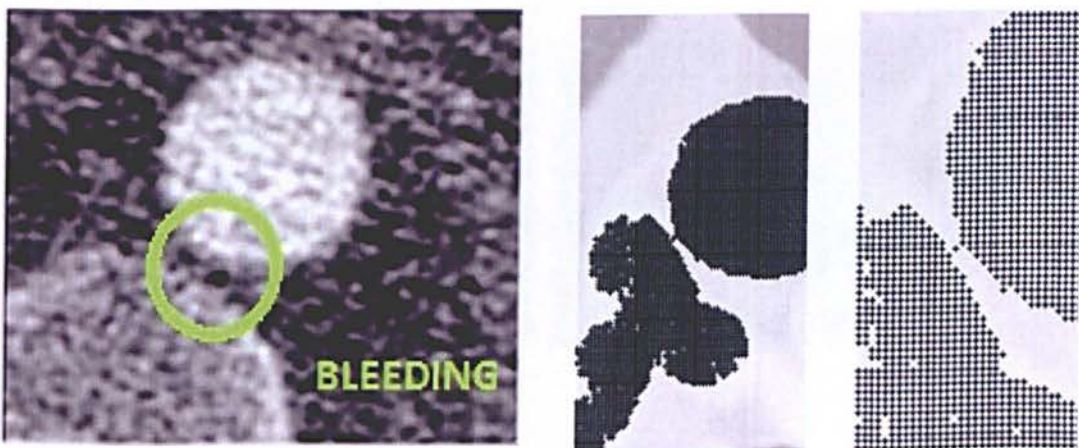
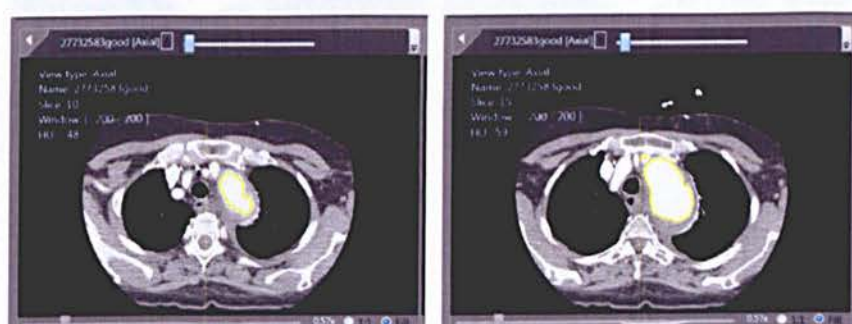
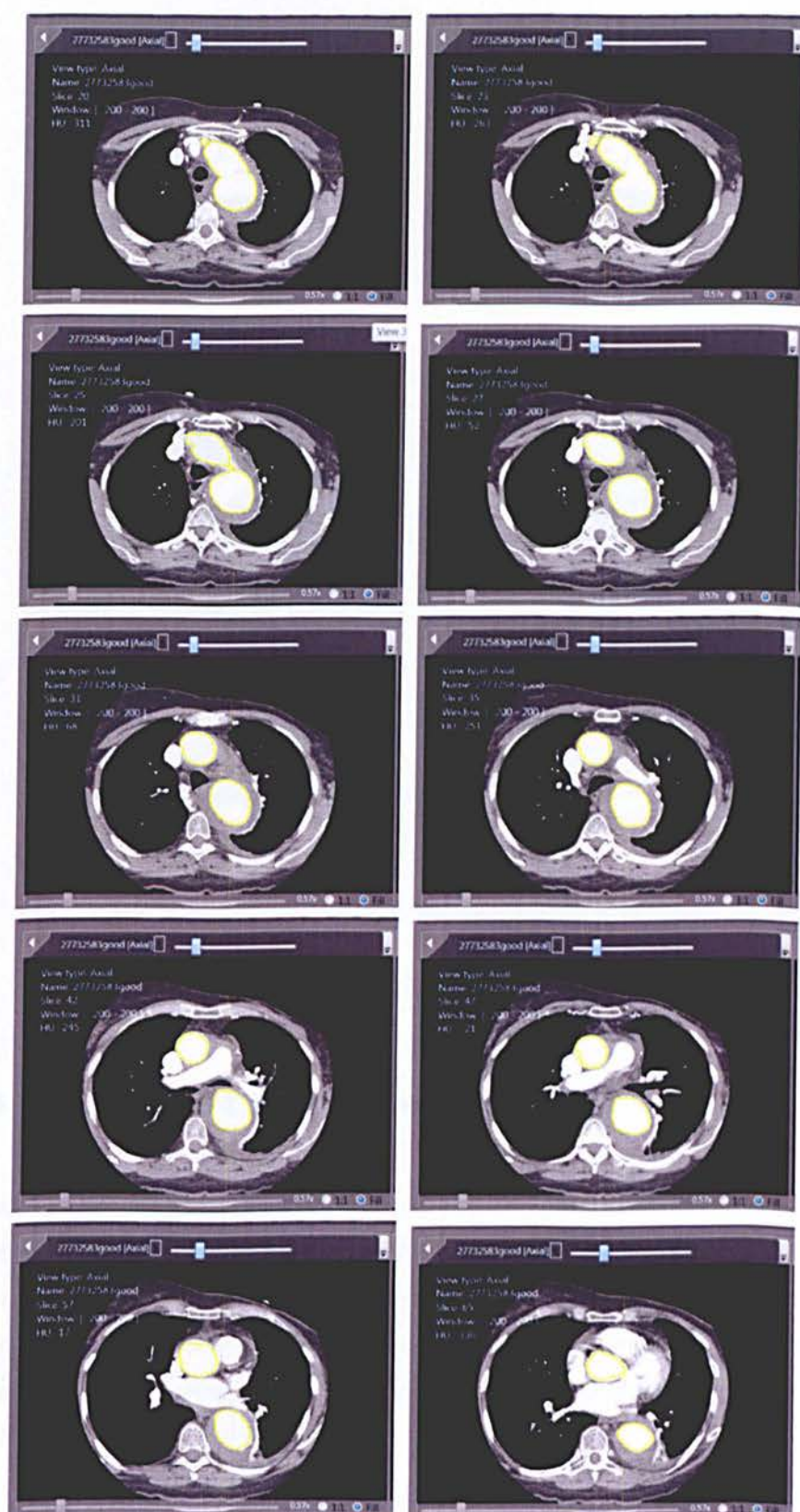


Figure 5.18: Example of bleeding region in CTA image, reason two regions merge.

In figure 5.19 we have the final output of the detected lumen using the 3D region growing algorithm. Illustrated in MIPS3 the colour yellow represents the region where the lumen has been detected.





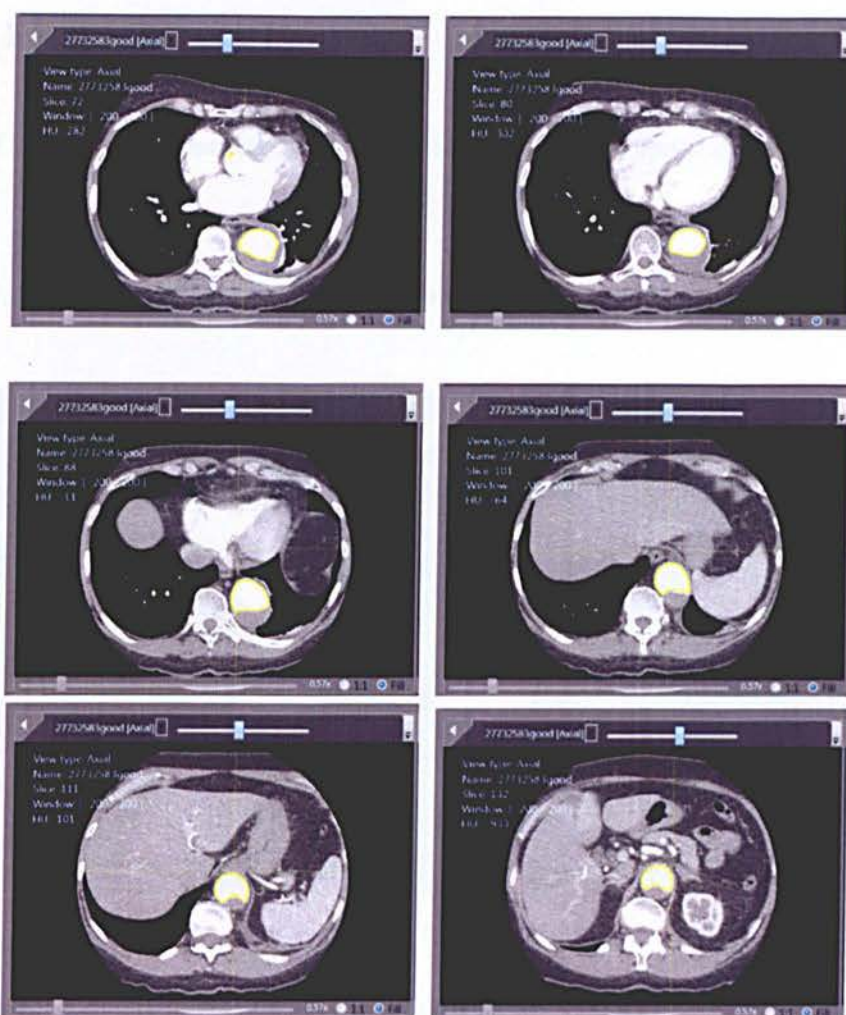


Figure 5.19: Output of detection and segmentation of thoracic aortic lumen.

5.2.2.1.3. Validation of Lumen segmentation

We successfully created an automated starting point by using as a landmark for the first the seed point of the region by using the end of the lungs that includes the celiac trunk which is attached to the thoracic aorta. The result of seed point selection on 30 training dataset showed that the seed points were correctly selected on all 30 dataset (100% sensitivity). The region growing algorithm successfully detected the aortic lumen on all 30 training dataset, and this has been confirmed by a radiologist visual inspection.

5.2.2.2. Identify Lumen Centreline Using DT

Once the TA has been segmented the skeletisation method previously described in section 4 is applied.

In figure 5.19 (a) we have a sagittal view of the thoracic aortic lumen and in (b) is the extracted centre line.

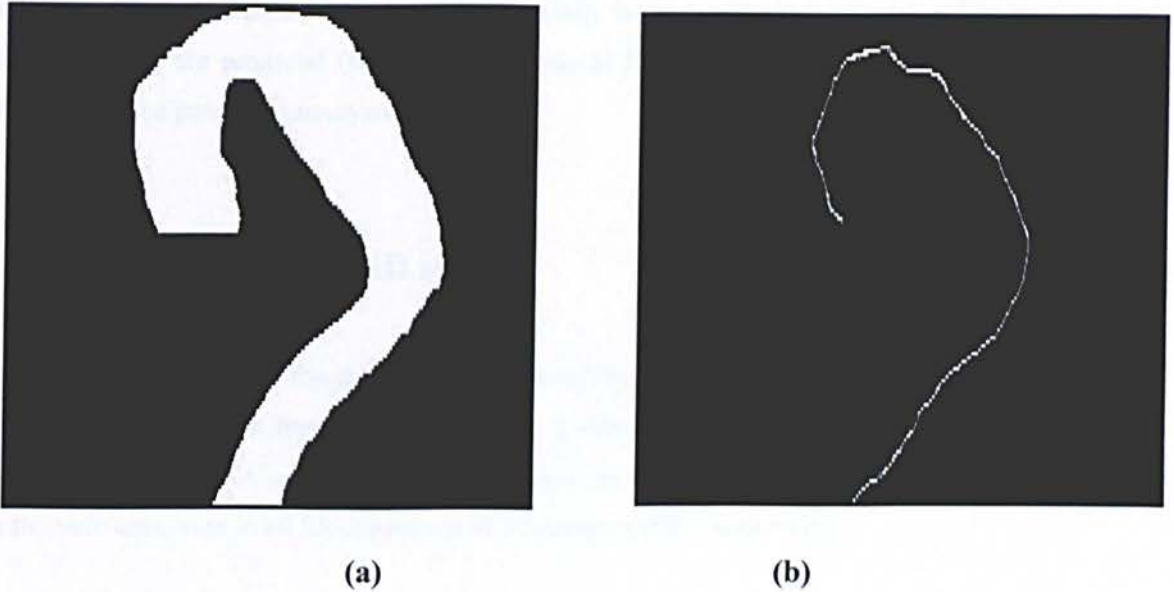


Figure 5.20: (a) Sagittal view of lumen segmentation (b) Centreline extraction after pruning.

After detecting the centreline and to be able to accurately detect the complete thoracic aorta with the potential aneurysm, it is important to use the reconstructed image of the vessel (orthogonal plane to centreline).

5.2.2.3. Generating Plane Orthogonal to Centreline

The orthogonal planes to centerline are generated (refer to section 3.3, figure 3.20). We will therefore be able use the reconstructed images for the detection of the thoracic aortic aneurysm in the next step of our CAD component.

5.2.2.4. Automatic detection of aneurysm (CAD)

Once again the region growing method is applied but this time on the reconstructed images to detect any TAA.

It is then followed by dilation of the aorta (refer to illustration in figure 3.21), where a simple thresholding technique using the same range of Hounsfield units for thoracic aorta aneurysm is applied and any objects that have been successfully been detached are considered to be false positives hence are removed (refer to illustration in figure 3.23). Any attached objects are considered to be potential aneurysms.

5.2.2.4.1 Validation of CAD system

The CAD system successfully removes the connectivity of small objects present in 21 of the 30 training scan datasets. It has been validated on a clinical dataset of 30 CTA scans where 28 contained aneurysms. A radiologist has confirmed the CAD system has successfully detected the thoracic aneurysm in all 28 dataset out of 30 dataset (100% sensitivity).

The result of CAD was good enough as the initial segmentation for CAM: There were 0 false positives and 100% true positives (each slice of TAA was initially segmented by CAD)

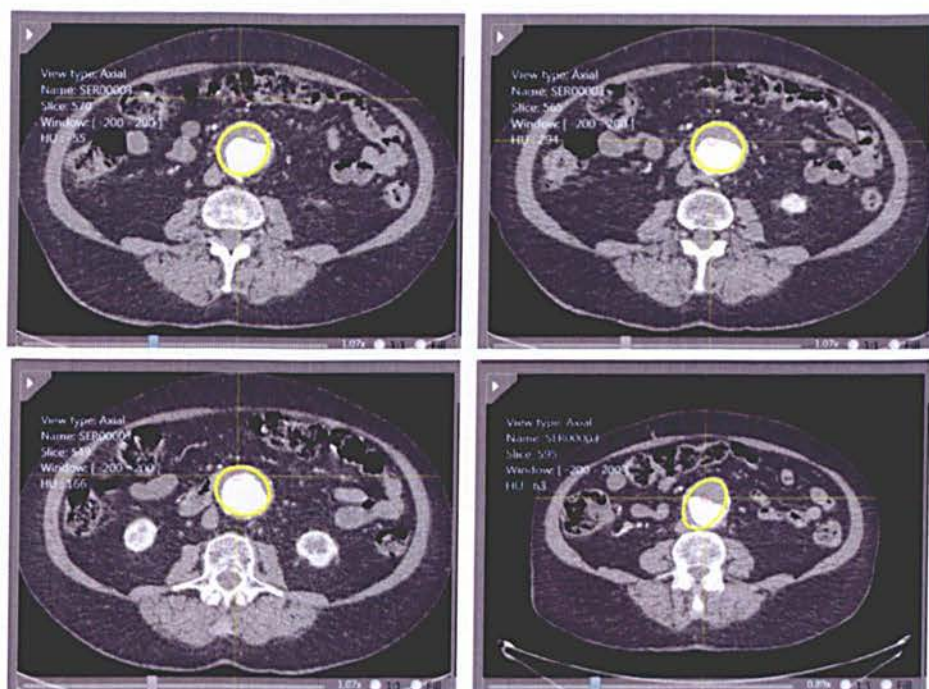


Figure 5.21: View of TAA including annotation of the Aorta and quantification features.

Once the thoracic aorta aneurysm is detected, other parameters such as diameters (maximum, minimum, and average), perimeter, aneurysm volume and the volume all using the eigenvector and eigenvalues calculated while creating the ellipse, using the contour values of the aorta.

5.2.3.1.1 Validation of CAM system

In section, 5.2.1.4.1, our CAD component had detected the presence of aneurysm in 28 out of 30 data sets. We can see some slices in the figure 5.22, where our previous CAD had successfully detected the aneurysm, however some of the muscle tissue is still attached to the aorta as being part of the aneurysm, represented in green colour.

We use the segmentation of CAD as our initial segmentation for CAM, but to be able to characterize the aneurysm we need to have a fine segmentation of the borders' of the TA, therefore as we can see below in figure 5.22, our ellipse fitting method has correctly delineated the aneurysm border, delineated with red colour.

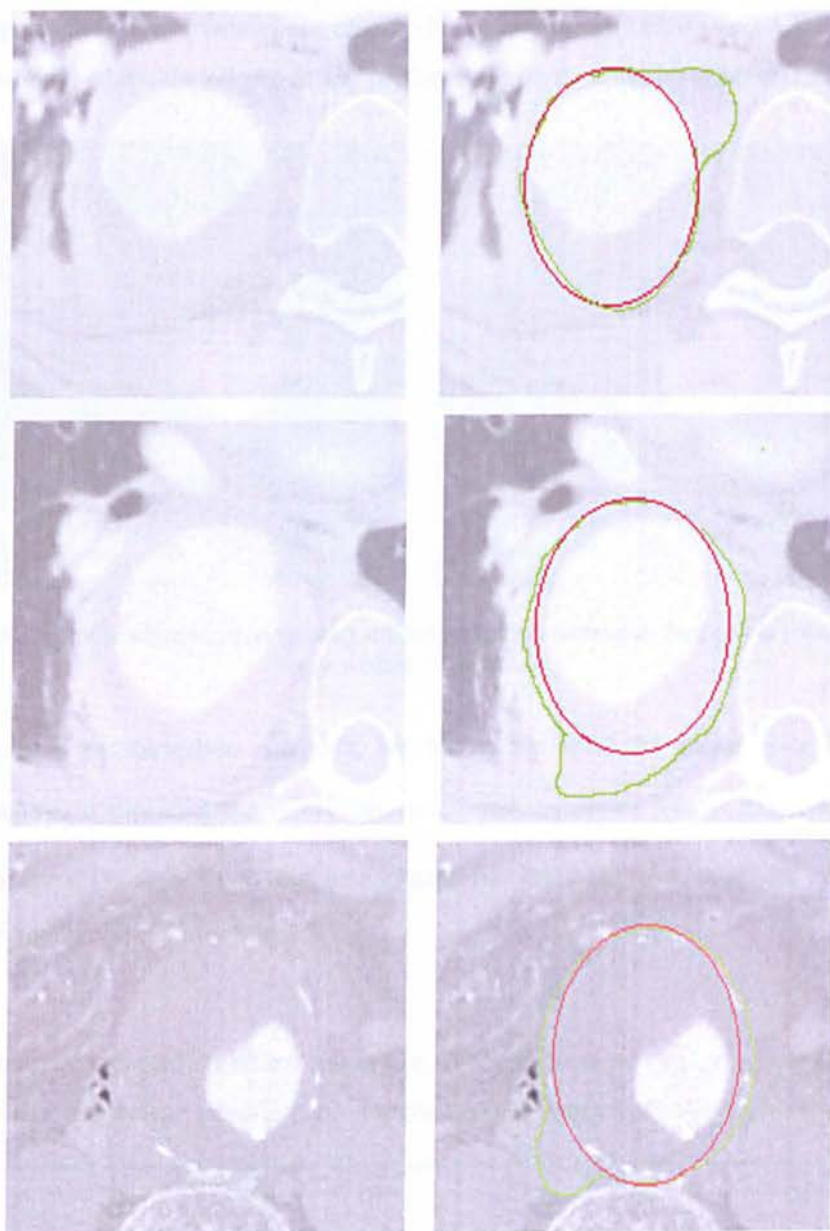


Figure 5.22: Original image (left) and right image shows the comparison between initial segmentation of CAM (green) and CAM aneurysm segmentation result using ellipse fitting (red).

As previously mentioned in our literature review, there were different possible methods for segmenting the TAA. To prove our method has definitely got the edge over other methods such as level set, we have decided to test the ellipse fitting algorithm against a level set algorithm. (refer to section 2.3.2.3).

Below in figure 5.23, we have a slight change in the segmentation of the TAA when applying different methods, where the ellipse fitting performs better than the level set method

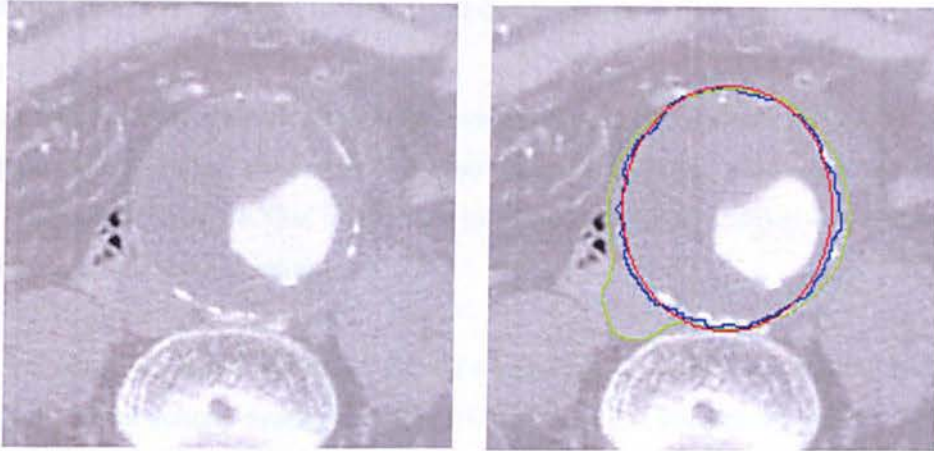


Figure 5.23: Initial segmentation (green), ellipse fitting segmentation (red colour) and level set segmentation (blue colour).

To quantify both segmentation methods, we have computed the mean error for clinically relevant measures comprising the minimum, mean and maximum vessel diameter, $\bar{e}_{D_{\min}}$, $\bar{e}_{D_{\text{mean}}}$ and $\bar{e}_{D_{\max}}$ respectively, as well as the mean error for the centreline position, which we had acquired previously, refer to section 5.3.1.1.

Table 2: Mean errors and standard deviation of the diameters $\bar{e}_{D_{\min}}$, $\bar{e}_{D_{\text{mean}}}$ and $\bar{e}_{D_{\max}}$, and for the centreline position \bar{e}_{x_0} for the two approaches investigated.

Approach	Accuracy			
	$\bar{e}_{D_{\min}}$	$\bar{e}_{D_{\text{mean}}}$	$\bar{e}_{D_{\max}}$	\bar{e}_{x_0}
Level Set	3.69±1.57	1.96±2.63	6.40±6.68	1.03±0.95
Ellipse fitting	1.80±1.02	0.60±0.74	1.57±1.37	0.76±0.69

We took into consideration that the vessel cross-section in the real data is not circular hence to compute the $\bar{e}_{D_{min}}$, $\bar{e}_{D_{mean}}$ and $\bar{e}_{D_{max}}$ we defined the diameter by the length of a straight line that connects two points in the vessel boundary and that passes through the centre x_0 .

Hence as ellipse fitting method performance was more accurate (table2) and as we know level set method usually suffers from a high computational complexity particularly when working with 3D datasets such as DICOM images, we have come to the conclusion that ellipse fitting is the best method in our application.

To validate our automated CAM result, we use a quantitative comparison based on two different criteria: (a) percent volume overlap as defined in equation 5.1, (b) percent volume difference as defined in equation 5.2, (c) correlation between automated measures and manual tracing, and (d) 3-D shape difference analysis.

Given two different labelling of a structure, L_1 and L_2 , and a function $V(L)$, which takes a label and returns its volume, the percent volume overlap is given by:

$$M(L_1, L_2) = \frac{V(L_1 \cap L_2)}{\left(\frac{V(L_1) + V(L_2)}{2} \right)} \times 100 \quad (5.1)$$

For identical labelling, $M(L_1, L_2)$ achieves its maximum value of 100, with decreasing values indicating less perfect overlap.

Note that the overlap between two different labelling will be reduced by slight shifts in the spatial location of one label with respect to another.

Given that many organ segmentation studies are only interested in quantifying volumetric changes, we quantified volume difference between two labelling that is insensitive to spatial shift.

$$N(L_1, L_2) = \frac{|V(L_1) - V(L_2)|}{\left(\frac{V(L_1) + V(L_2)}{2}\right)} \times 100 \quad (5.2)$$

For labels with identical volume, $N(L_1, L_2)$ achieves its optimal value of zero, with increasing values indicating a greater volume difference between the two labelling. Note that greater values of $N(L_1, L_2)$ lead directly to reduce statistical power to detect subtle volumetric changes in aorta.

The performance was compared using Multivariate Analysis of Variance (MANOVA) on two dependent variables, volume overlap and volume difference, with 2 factors: region, method (manual, automatic).

Table 3: Comparison of automated measures to manual tracing

Automated measure	Average column ± SD	% Volume overlap	% volume difference	Correlation with manual segmentation
CAM	4190±526.7	82%±1.5	4%±2.1	$r=0.86$, y-intercept=496

To measure the ability of automated methods to capture the true variability in volume within a group, we computed Pearson correlation.

We computed correlations between manual tracing and the automated segmentation method (CAM). A strong correlation yields small volumes for small structures and large volumes for large structures.

We assume that volumes calculated by manual tracing are closest to the true volumes for a given structure. The intercept of the fitted line provides information about systematic differences estimates between segmentations.

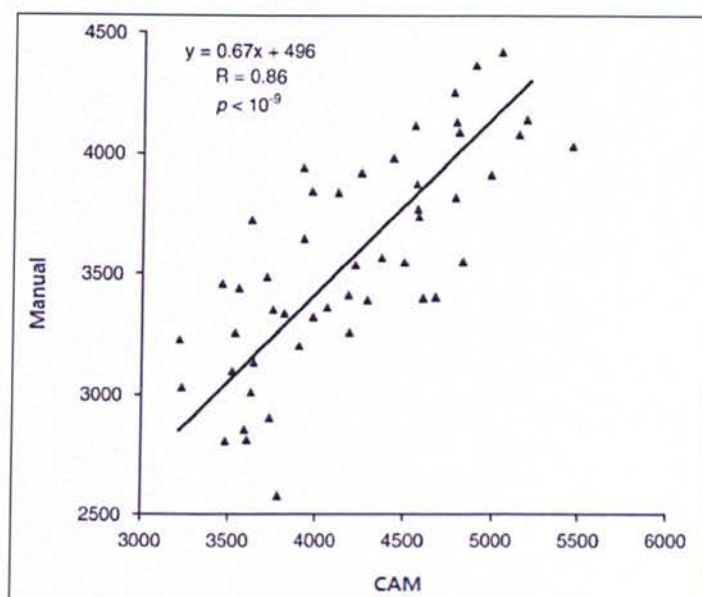


Figure 5.24: Volume correlation derived from manual segmentation and CAM($R=0.86$).

5.4 Summary

In this chapter we presented the experimental results and analysis of performance of our automatic approach for detection and quantification of thoracic aortic aneurysms in the CAD and CAM component.

Our CAD system has been validated on a clinical dataset of 30 CTA scans where 28 contained aneurysms with an average of 300 slices per scan. 30 CTA scans have been used as training dataset for parameter selection and as a test dataset. CAM performance was evaluated by computing the correlation between our automated system and the radiologists manual segmentation and proved to have a successful correlation of $R=0.86$.

The radiologist has also visually inspected the CAM system results and confirmed it correctly selected the TAA on all the 28 datasets, proving to have 100% sensitivity. The detection and segmentation performance as well as computer efficiency of the system indicate the approach has potential in clinical applications, and could successfully be applied in the daily routine of a radiologist work environment in the near future.

Chapter 6

Conclusions

This chapter concludes the dissertation. In section 6.1, we summarise our contributions to the field of medical imaging. In the following section, we highlight remaining open issues and limitations of the proposed solutions as well as a number of avenues for future research. Finally, closing remarks are provided in section 6.3.

6.1. Conclusions

The aorta is the largest blood vessel, with an internal diameter around 2.5cm and a wall thickness of 2mm in an adult human body, directing the flow of oxygenated blood away from the heart into the progressively smaller branches of the systemic arterial circulation. The ascending aorta originates from the left ventricle of the heart and briefly extends upward before arching down through the thoracic and abdominal cavities, where it terminally branches into the two common iliac arteries. Thus, the aorta is divided into three anatomically and developmentally distinct segments: the ascending aorta, the aortic arch, and the descending aorta.

An aneurysm is defined as dilatation of the aorta of greater than 1.5 times its normal diameter for a given segment. For the thoracic aorta, a diameter greater than 3.5 cm is generally considered dilated, whereas greater than 4.5 cm would be considered aneurismal. The rate of incidence of thoracic aortic aneurysms (TAA) is 5.9/100,000 people per year, with an average age of 65 and slightly higher prevalence in males than females. However, risk of rupture does not differ between genders.

Most thoracic aneurysms are asymptomatic and are typically detected when imaging studies (chest x-rays, CT scans, MRI, etc) are being obtained. Aneurysms tend to lead to high rates of morbidity and mortality. If an aneurysm is not diagnosed or treated within time its progressive growth may eventually cause a rupture of the aorta. The likelihood of a rupture occurring in the TAA (thoracic aortic aneurysm) depends on its size. Therefore, our main motivation for this project is the need for a segmentation of the aneurysm for a subsequent accurate measurement. As general practice, the aneurysm regions are manually segmented from the CT Angiography

(CTA) images by expert radiologists before the measurement. This is an expensive, time consuming and prone to error method.

In this project we proposed a fully automated computer aided detection (CAD) and measurement (CAM) system for the detection of potential aneurysm in the entire thoracic aorta, which is robust and accurate and requires no human interaction, and ultimately would greatly alleviate the workload burden on the radiologist, as well as improving accuracy of detection.

Developing this algorithm has proven to be challenging due to the anatomical shape of the thoracic aorta and its aneurysms, as well as the similarities in pixel intensities of organs(tissues, bone, etc).

Our priority was to fully automate the system, to find a seed point that would be consistent from patient to patient. We decided celiac trunk to be a perfect landmark which would be used as a starting point to correctly locate the thoracic aorta and use that slice as a start point for the remaining algorithm.

Due to a vessel curved shape anatomy, it is difficult to measure the true diameter of the aorta. We investigated several methods previously proposed that use level set techniques. But even though these methods have been effective at finding the vessel boundary they suffer from a high computational complexity particularly when working with 3D datasets such as DICOM images. We overcame this by using a skeletonization method based on distance transform. As we work with large 3D volumetric DICOM data sets, where computational time is extremely important factor, distance transform application was the most appropriate method due to its computational efficiency.

We found a completely novel way to detect aneurysms by applying an ellipse fitting algorithm in our CAM system. Our method was based on a previously developed algorithm used for a different application, and its potential had never been explored in real application such as CAM system.

One of the main challenges was to make our CAD/CAM system computer efficient, so it will be viable to be used in the radiologist work environment. We have successfully managed to

make the algorithm fast which we believe will serve to alleviate greatly their workload burden on by reducing image reading time.

Moreover, due to the high volume of scans to be read, reader fatigue and the complexity of images, it is inevitable that some aneurysms are currently being missed without the use of a computer assist tool. As a result, the utilization of this CAD/CAM tool would serve to improve not only the efficiency but the accuracy of aneurysms detection when screening is performed on patients.

The CAD/CAM system will also prove to be invaluable to when planning surgeries for the introduction of stents for repair of the thoracic aorta as all measurements required are calculated in the system. Therefore the surgeon has already the idea of the size of stent necessary for each specific patient.

In this thesis we successfully developed a fully automated Computer Aided Detection (CAD) and Measurement (CAM) systems, which is able to segment and visualize the often difficult geometry of the rare but potentially fatal thoracic aortic aneurysm. Although other CAD/CAM systems have been developed for other organ detection and even small sections of the thoracic aorta, to date no fully automated CAD/CAM of the entire thoracic aorta has been developed hence its complete novelty.

The system has been validated on a clinical dataset of 30 CTA scans with average 300 slices per scan, where 28 contained aneurysms. 30 CTA scans have been used as training dataset for parameter selection and another 30 CTA scans as a test dataset, in total 60 for clinical evaluation. The radiologist visually inspected the CAD and CAM component results and confirmed it correctly segmented the TAA on all the 28 datasets, proving to have 100% sensitivity. The detection and segmentation performance indicate the approach has potential in clinical applications.

In conclusion, the automated thoracic aorta detection is comparable with the manual segmentation concerning its accuracy, and the automated segmentation gives more reproducible results than the segmentations performed by medical experts.

Our automated approach therefore shows great potential for successful integration into the clinical workflow.

6.2. Future Research

This project has enormous scope for further investigation. There are further characteristics of the thoracic aorta that can in the future be included in the system according to the requirements of radiologists.

Radiologists consulting in this research have expressed interest in applying a similar system in other cases not only of thrombosis as in our case. But for example, in aortic dissection cases that also affects a large amount of the population in the UK.

St Georges Hospital of London have funded this project and are looking to take it further by conducting a clinical study in the next 1-2years to evaluate our developed CAD system integrating it in MIPS3 platform .

Inter and intra observability measurements are one of the additional main features of the platform. This has not been utilised in our study, but is very important to take into account in the future as humans are susceptible to committing errors and their analysis is usually subjective due to the inter and intra observer variability issue.

Different radiologists may well interpret data differently due to their work experience. For example the inter observer variability involves the difficulty the radiologist may have to find the exact border of an abnormalities in the CT scan being inspected, but there is also the intra observer variability where the radiologist may identify regions differently even when analysing the same data different times, sometimes due to simple shaking action of the hands when delineating the borders of the abnormality in the computer. Therefore being able to visualise in the platform the different annotations of different radiologist will lead to a more accurate diagnostic decision by the physician.

6.3. Closing Remarks

Our contributions proved to be especially useful in greatly alleviating the workload burden on radiologists by reducing image reading time as well as meeting a previously described need for an automated system for detection and characterization of thoracic aorta. Our automated approach shows the great potential for successful integration into the clinical workflow.

Finally, the presented contributions are intended to motivate future research in the area of detection and quantification of other cardiovascular diseases.

References

- [1] Tortora, Gerard J, "Principles of anatomy and physiology" Hoboken, 11th Edition, N. J. Wiley, 2006.
- [2] Normal Aorta Anatomy <http://www.teamt.us/Bicuspid_Aortic_Valve.htm>[Accessed 5 November 2008].
- [3] Pressler V, McNamara JJ, "Aneurysm of the thoracic aorta." Surgery, 1985.
- [4] Bickerstaff LK, Pairolero PC, Hollier LH, "Thoracic aortic aneurysms: a population-based study" Surgery, 1982.
- [5] Thoracic aortic aneurysm <http://www.slrcsurgery.com/Thoracic%20aortic%20aneurysms.htm#_What_is_a_thoracic%20aortic%20aneurysm?> [Accessed 5 of November 2008]
- [6] Oleg S. Pinykh, "Digital Imaging and Communications in Medicine (DICOM): A Practical Introduction and Survival Guide" Second Edition Springer, 2010.
- [7] JE Aldrich, AM Bilawich, and JR Mayo, "Radiation doses to patients receiving computed tomography examinations in British Columbia" Canadian Association of Radiologists Journal, vol 57:2 pag 79-85, 2006.

[8] Product Details: Aquilion One. Product information for Toshiba CT Scanners<<http://www.auntminnie.com/index.asp?sec=vdp&sub=products&pag=searchproductdetail%?typeid=10216&productid=48562/idl>>[Accessed 8 November 2008].

[9] LW Goldman, "Principles of CT and evolution of CT technology." RSNA Categorical Course in Diagnostic Radiology Physics: CT and US Cross-sectional Imaging, 2000.

[10] AM Cormack, "Representation of a function by its line integrals, with some radiological applications." Journal of Applied Physics volume 34 pages 2722, 1963.

[11] GN Hounsfield, "Computerized transverse axial scanning (tomography) part 1: Description of system" British Journal of Radiology volume 46 page 552, 1973.

[12] Willi A. Kalender, "Computed Tomography: Fundamentals, System Technology, Image Quality, Applications" Wiley VCH, 3rd Edition, 2011.

[13] G. Hahn, R. Hupke, G. Kohl, and J. Leppert, "Developing an Ultrafast radiation Detector for CT Scanning", Siemens, Research and Innovations, Sensors 1997.

- [14] E Seeram, "Computed Tomography: Physical Principles, Clinical Applications and Quality Control" W. B. Saunders, 1994.
- [15] F Attix, "Introduction to radiological physics and radiation dosimetry" Wiley, 1986.
- [16] MS Panajkar, AA Majmudar, and C Gophinathan, "Radiation induced polymerization of N,N'-methylenebisacrylamide in aqueous solution" Journal of Macromolecular Science volume 12 pages 2423-2433, 1997.
- [17] Rubin GD. "Helical CT angiography of the thoracic aorta." RSNA, Categorical Course in Diagnostic Radiology: Thoracic Imaging-Chest and Cardiac, 2001.
- [18] Gavant ML, Menke PG, Fabian T, Flick PA, Graney MJ, Gold RE. "Blunt traumatic aortic rupture: detection with helical CT of the chest." Radiology. 1995.
- [19] Greenberg RK, O'Neill S, Walker E, "Endovascular repair of thoracic aortic lesions with the Zenith TX1 and TX2 thoracic grafts: intermediate-term results", Surgery volume 41 pages 589-96, 2005.
- [20] Songyang Yu, Ling Guan, "A CAD system for the automatic detection of clustered microcalcifications in digitized mammogram films" Medical Imaging, IEEE Transactions, 2000.

- [21] S. Liu, C. F. Babbs, and E. J. Delp, "Multiresolution detection of spiculated lesions in digital mammograms" *Image Process , IEEE Transactions*, 2001.
- [22] R. Bellotti, F. D. Carlo, S. Tangaro, G. Gargano, G. Maggipinto, M. Castellano, R. Massafra, D. Cascio, F. Fauci, R. Magro, G. Raso, A. Lauria, G. Forni, S. Bagnasco, P. Cerello, E. Zanon, S. C. Cheran, E. L. Torres, U. Bottigli, G. L. Masala, P. Oliva, A. Retico, M. E. Fantacci, R. Cataldo, I. D. Mitri, and G. D. Nunzio, "A completely automated CAD system for mass detection in a large mammographic database" *Medical Physics* volume 33 pages 3066-75, 2006.
- [23] N. H. Eltonsy, G. D. Tourassi, and A. S. Elmaghraby, "A concentric morphology model for the detection of masses in mammography," *IEEE Trans. Med. Imag.*, 2007.
- [24] S. Timp, C. Varela, N. Karssemeijer, and B. Dacolian, "Temporal change analysis for characterization of mass lesions in mammography" *IEEE Transactions Medical Imaging* volume 26 pages 945-53, 2007.
- [25] Kobashi, S., Kondo, K., Hata, Y, "Computer-aided diagnosis of intracranial aneurysms in MRA images with case-based reasoning" *The Institute of Electronics, Information and*

Communication Engineers (IEICE) Transactions on Information and Systems volume 89 pages 340-50, 2006.

[26] Yoshikazu Uchiyama, Ryujiro Yokoyama, Hiromichi Ando, Takahiko Asano, Hiroki Kato, Hiroyasu Yamakawa, Haruki Yamakawa, Takeshi Hara, Toru Iwama, Hiroaki Hoshi, and Hiroshi Fujita, "Improvement of Automated Detection Method of Lacunar Infarcts in Brain MR Images" Proceedings of the 29th Annual International Conference of the IEEE Eng Med Biol Soc pages 1599-602, 2007.

[27] Lauric, A., Miller, E., Frisken, S., Malek, A., "Automatic Detection of Intracranial Aneurysms Based on Parent Vessel 3D Analysis" Medical Image Analysis volume 14 pages 149–159, 2010.

[28] Robert D. Ambrosini, Peng Wang, Walter G. O'Dell, "Computer-Aided Detection of Metastatic Brain Tumors Using Automated 3-D Template Matching" Journal Magnetic Resonance Imaging volume 31 pages 85-93, 2010.

[29] T. W. Way, L. M. Hadjiiski, B. Sahiner, H.-P. Chan, P. N. Cascade, E. A. Kazerooni, N. Bogot, and C. Zhou, "Computer-aided diagnosis of pulmonary nodules on CT scans: segmentation and classification using 3D active contours" Medical Physics, 2006.

- [30] J IA Tong, ZHAO Da-Zhe, WEI Ying, ZHU Xin-Hua, WANG Xu "Computer-Aided Lung Nodule Detection Based on CT Images" IEEE/ICME International Conference on Complex Medical Engineering, 2007.
- [31] Ye, X., Lin, X., Dehmeshki, J., Slabaugh, G. and Beddoe, G "Shape based computer-aided detection. of lung nodules in thoracic CT images" IEEE Transactions on Biomedical Engineering volume 56 pages 1810-20, 2009.
- [32] J. Dehmeshki, H. Amin, "A smooth and stable fly- through scheme for virtual navigation of 3D colonography" 3DTV Conference, 2007.
- [33] Vincent F. van Ravesteijn, Cees van Wijk, Frans M. Vos, Roel Truyen, Joost F. Peters, Jaap Stoker, Lucas J. van Vliet "Computer-Aided Detection of Polyps in CT Colonography Using Logistic Regression" IEEE Transactions on Medical Imaging volume 29 pages 120-31, 2010.
- [34] D. Rueckert, P. Burger, S. M. Forbat, R. D. Mohiaddin, and G. Z. Yang, "Automatic tracking of the aorta in cardiovascular MR images using deformable models" IEEE Transactions on Medical Imaging volume 16 pages 581-90 , 1997.

- [35] L. Flórez Valencia, J. Montagnat, M. Orkisz, “3D models for vascular lumen segmentation in MRA images and for artery-stenting simulation” IRBM, 2007.
- [36] V. Bombardier, M.C. Jaluente, A. Bubel, and J. Bremont, “Cooperation of two fuzzy segmentation operators for digital subtracted angiograms analysis” IEEE Conference on Fuzzy Systems, 1997.
- [37] T. Kitasaka, K. Mori, J. Hasegawa, J. Toriwaki, and K. Katada, “Automated extraction of aorta and pulmonary artery in mediastinum from 3D chest x-ray CT images without contrast medium” SPIE Medical Imaging, 2002 .
- [38] T. Kovacs, Ph. Cattin, G. Székely, “Automatic Segmentation of the Vessel Lumen from 3D CTA Images of Aortic Dissection” Bildverarbeitung für die Medizin, 2006.
- [39] U. Kurkure, O. C. Avila-Montes, and I. A. Kakadiaris, “Automated segmentation of thoracic aorta in non-contrast CT images” Proceedings of the fifth IEEE International Symposium on Biomedical Imaging, 2008.
- [40] M. Feuerstein, T. Kitasaka, and K. Mori, “Automated anatomical likelihood driven extraction and branching detection of aortic arch in 3-D chest CT” Second International Workshop on Pulmonary Image Analysis, 2009.

- [41] I. Išgum, A. Rutten, M. Prokop, and B. van Ginneken, "Automated calcium scoring in the aorta in low dose computed tomography scans of the thorax" *Medical Physics*, 2010.
- [42] Ivana Išgum, Marius Staring, Annemarieke Rutten, Mathias Prokop, Max A Viergever, Bram Van Ginneken, "Multi-atlas-based segmentation with local decision fusion--application to cardiac and aortic segmentation in CT scans" *IEEE Transactions on Medical Imaging* volume 28 pages 1000 - 10, 2009.
- [43] A. K. Jain, "Partial differential equations and finite-difference methods in image processing" *Journal Optimized Theory Applications* volume 23 pages 817 – 34, 1977.
- [44] J. J. Koenderink, "The structure of images" *Biology Cybernetics*, volume 50 pages 363-70, 1984.
- [45] A. P. Witkin, "Scale-space filtering" In *Proceedings International Joint Conference Artificial Intelligence*, 1983.
- [46] P. Perona and J. Malik., "Scale-space and edge detection using anisotropic diffusion" *IEEE Transactions Pattern Analysis Machine Intelligence*, 1990.

- [47] L. Alvarez, P. Lions, and J. Morel., "Image selective smoothing and edge detection by nonlinear diffusion" SIAM Journal Numeric Analysis Volume 29 pages 182-193, 1992.
- [48] C. Price, P. Wambacq, and A. Oosterlink., "Image enhancement and analysis with reaction-diffusion paradigm." IEE Proceedings, 1990.
- [49] J. Weickert, "Coherence-enhancing diffusion filtering" International Journal of Computer Vision volume 31 pages 111–127, 1999.
- [50] J. Weickert, "A review of nonlinear diffusion filtering" In Scale-space Theory in Computer Vision, 1993.
- [51] T. Lindeberg., "Scale-Space Theory in Computer Vision" Kluwer Academic, 1994.
- [52] J. Sporring, M. Nielsen, L. Florack, and P. Johansen, "Gaussian scale-space theory" Kluwer, 1997.
- [53] A. Witkin and M. Kass. "Reaction-diffusion textures" Computer Graphics, 1991.
- [54] X. Li and T. Chen., "Nonlinear diffusion with multiple edginess thresholds" Pattern Recognition, 1994.

- [55] W.Niblack., "An Introduction to Digital Image Processing" Prentice/Hall International, 1986.
- [56] D.R. Ney, E.K. Fishman, "Editing Tools for 3D Medical Imaging", IEEE Computer Graphics and Applications, 1991.
- [56] Gonzalez R. C, Richard E. Woods, "Digital image processing" 3rd Edition, Upper Saddle River, N.J. Pearson Prentice Hall, London, Pearson Education, 2008.
- [57] D.R. Ney, E.K. Fishman, "Editing Tools for 3D Medical Imaging" IEEE Computer Graphics and Applications, 1991.
- [58] S. Shiman, G.D. Rubin, S. Napel, "Semiautomated editing of computed tomography sections for visualization of vasculatures Medical Imaging: Image Display, 1996.
- [59] M. Fiebich, M.M. Tomiak, R.M. Engelmann., "Computer Assisted Diagnosis in CT Angiography of Abdominal Aortic Aneurysms" Medical Imaging: Image Processing, 1997.
- [60] Y. Yang and H. Yan, "An adaptive logical method for binarization of degraded document images" Pattern Recognition, 2000.

- [61] Otsu, N, "A threshold selection method from gray-level histograms" IEEE Transactions on Systems, Man, Cybernetics volume 9 pages 62-66, 1979.
- [62] J. Kittler, J. Illingworth, J. Foglein, and K. Paler, "An automatic thresholding algorithm and its performance" Proceedings 7th International Conference Pattern Recognition pages 287-289, 1985.
- [63] M. H. F. Wilkinson, "Rapid automatic segmentation of fluorescent and phase-contrast images of bacteria" Fluorescence Microscopy and Fluorescent Probes, 1996.
- [64] Slobodan Ilic and Branislav Ulicny. "Seeded region growing method for image segmentation" Swiss Institute of Technology, 2000.
- [65] Y.L. Chang and X. Li, "Adaptive image region growing" IEEE Transactions on Image Processing volume 3 pages 868-72, 1994.
- [66] R. Adams and L. Bischof, "Seeded region growing" IEEE Transactions on Pattern Analysis and Machine Intelligence volume 16 pages 641-47, 1994.

- [67] J.P. Gambotto “A new approach to combining region growing and edge detection” Pattern Recognition Letters, 1993.
- [68] S.A. Hojjatoleslami and J. Kittler, “Region growing: a new approach”, CVSSP, 1995.
- [69] S. Singh, R. Al-Mansoori “Identification of regions of interest in digital mammograms” Journal of Intelligent Systems volume 10 pages 212–218, 2000.
- [70] W.Niblack. “An Introduction to Digital Image Processing” Prentice/Hall International, 1986.
- [71] S. Osher and J.A. Sethian, “Fronts propagating with curvature-dependent speed: algorithms based on Hamilton-Jacobi formulations” Journal of Computational Physics volume 79 pages 12-49, 1988.
- [72] A. Litman, D. Lesselier, and F. Santosa, “Reconstruction of a two-dimensional binary obstacle by controlled evolution of a level-set” Inverse Problems, 1998.
- [73] O. Dorn, E.L. Miller, and C.M. Rappaport, “A shape reconstruction method for EM tomography” Inverse problems, 2000.

- [74] F. Santosa, "A level-set approach for inverse problems involving obstacles" ESAIM: Control, Optimisation and Calculus of Variations, 1996.
- [75] Levenberg-Marquardt, "Level set methods for inverse obstacle problems" Inverse problems, 2004.
- [76] M. Soleimani, "Computational aspects of low frequency electrical and electromagnetic tomography: A review study" International Journal of Numerical Analysis and Modelling, 2008.
- [77] S. Osher and R.P. Fedkiw, "Level set methods and dynamic implicit surfaces" Springer Verlag, 2003.
- [78] M. Kilmer, E. Miller, M. Enriquez, and D. Boas, "Cortical constraint method for diffuse optical brain imaging" Proceedings of SPIE, 2004.
- [79] S. Wang and M. Yu Wang, "Radial basis functions and level set method for structural topology optimization" International Journal for Numerical Methods in Engineering, 2006.
- [80] A. Gelas, O. Bernard, D. Friboulet, R. Prost, V. INSA, "Compactly supported radial basis functions based collocation method for level-set evolution in image segmentation" IEEE Transactions on Image Processing volume 16 pages 1873-87, 2007.

- [81] O. Bernard, D. Friboulet, P. Thevenaz, and M. Unser, "Variational B-Spline level-set: a linear filtering approach for fast deformable model evolution" IEEE Transactions on Image Processing, 2009.
- [82] E. R. Davies, "Finding ellipses using the generalized Hough transform" Pattern Recognition Letters, 1989.
- [83] Qiang Ji and Robert M. Haralick, "A Statistically Efficient Method for Ellipse Detection" IEEE International Conference on Image Processing, 1999.
- [84] R. K. Yip, P. K. Tam, D. N. Leung, "Modification of Hough transform for circles and ellipses detection using a 2-dimensional array" Pattern Recognition, 1992.
- [85] P. Yin, L. Chen, "New method for ellipse detection by means for symmetry" Journal of Electronic Imaging volume 3 pages 20-29, 1994.
- [86] C. Ho, L. Chen, "A fast ellipse/circle detector using geometric symmetry" Pattern Recognition, 1995.

- [87] A. S. Aguado, M. E. Montiel, M. S. Nixon, "Using directional information for parameter space decomposition in ellipse detection" *Pattern Recognition*, 1996.
- [88] S. Tsuji, F. Matsumoto, "Detection of ellipses by a modified Hough transform" *IEEE Transactions on Computers* volume 27 pages 777-81, 1978.
- [89] Aylward, S., Bullitt, E, "Initialization, noise, singularities, and scale in height ridge traversal for tubular object centreline extraction" *IEEE Transactions on Medical Imaging*, 2002.
- [90] Deschamps, T., Cohen, L.D, "Fast extraction of minimal paths in 3D images and applications to virtual endoscopy" *Medical Image Analysis*, 2001.
- [91] Wink, O., Niessen, W.J., Viergever, M.A, "Multiscale vessel tracking" *IEEE Transactions on Medical Imaging*, 2004.
- [92] Bitter, I., Kaufman, A.E., Sato, M., "Penalized-distance volumetric skeleton algorithm" *IEEE Transactions on Visualization and Computer Graphics*, 2001.
- [93] Paik, D.S., Beaulieu, C.F., Brooke Jeffrey, R., Rubin, G.D., Napel, S., "Automated path planning for virtual endoscopy" *Medical Physics*, 1998.

- [94] Dijkstra, E.W, "A note on two problems in connexion with graphs" Numerische Mathematik, 1959.
- [95] Vasilevskiy, A., Siddiqi, K., "Flux maximizing geometric flows" IEEE Transactions Pattern Analysis Machine Intelligence volume 24 pages 1565-77, 2002.
- [96] Blum, H., "Biological shape and visual science" Journal of Theoretical Biology volume 38 pages 205-87, 1973.
- [97] Siddiqi, K., Bouix, S., Tannenbaum, A., Zucker, S.W., "Hamilton–Jacobi skeletons" International Journal of Computer Vision volume 48 pages 215-231, 2002.
- [98] Dimitrov, P., Damon, J.N., Siddiqi, K., "Flux invariants for shape" Proceedings of the CVPR, 2003.
- [99] Pudney, C., "Distance-ordered homotopic thinning: a skeletonization algorithm for 3D digital images" Computer Vision and Image Understanding, 1998.
- [100] Borgefors, G., Nystrom, I., Baja, G.S.D., "Skeletonizing volume objects part II: from surface to curve skeleton" Proceedings of the SSPR, 1998.

- [101] Law, M., Chung, A., "Three dimensional curvilinear structure detection using optimally oriented flux" European Conference Computer Vision, 2008.
- [102] Yong Zhou, and Arthur W. Toga, "Efficient Skeletonization of Volumetric Objects" IEEE Transactions on Visualization and Computer Graphics volume 5 pages 196–209, 1999.
- [103] R. N. Bracewell,, "The fast Hartley transform" Proceedings IEEE volume 22 pages 1010-18, 1984.
- [104] P.J. Schneider, D.H. Eberly, "Geometric tools for computer graphics" Morgan Kaufmann, 2003.
- [105] H. Triebel, "Interpolation theory, function spaces, differential operators" North-Holland Publishing Company, 1978.
- [106] Andrew Fitzgibbon, Maurizio Pilu, and Robert B. Fisher, "Direct Least Square Fitting of Ellipses" IEEE Transactions on Pattern Analysis and Machine Intelligence pages 21 pages 476-80, 1999.
- [107] Gander, W, "Least squares with a quadratic constraint." Numerische Mathematik, 1981.

- [108] Haralick, R. M. and Shapiro, L. G, "Computer and Robot Vision" Addison Wesley, 1993.
- [109] Dehmeshki, J "Assessment of radiologist performance with and without computer-aided detection" Gastroenterology, 2006.
- [110] Baker JA, Rosen EL, Lo JY, Gimenez EI, Walsh R, Soo MS, "Computer-aided detection (CAD) in screening mammography: sensitivity of commercial CAD systems for detecting architectural distortion" American Roentgen Ray Society Journal volume 181 pages 1083-8, 2003.